

INFORMATION TO USERS

The most advanced technology has been used to photograph and reproduce this manuscript from the microfilm master. UMI films the original text directly from the copy submitted. Thus, some dissertation copies are in typewriter face, while others may be from a computer printer.

In the unlikely event that the author did not send UMI a complete manuscript and there are missing pages, these will be noted. Also, if unauthorized copyrighted material had to be removed, a note will indicate the deletion.

Oversize materials (e.g., maps, drawings, charts) are reproduced by sectioning the original, beginning at the upper left-hand corner and continuing from left to right in equal sections with small overlaps. Each oversize page is available as one exposure on a standard 35 mm slide or as a 17" x 23" black and white photographic print for an additional charge.

Photographs included in the original manuscript have been reproduced xerographically in this copy. 35 mm slides or 6" x 9" black and white photographic prints are available for any photographs or illustrations appearing in this copy for an additional charge. Contact UMI directly to order.



300 North Zeeb Road, Ann Arbor, MI 48106-1346 USA

Order Number 8824767

Multiresolution representations and wavelets

Mallat, Stephane Georges, Ph.D.

University of Pennsylvania, 1988

Copyright ©1988 by Mallat, Stephane Georges. All rights reserved.

U·M·I
300 N. Zeeb Rd.
Ann Arbor, MI 48106

PLEASE NOTE:

In all cases this material has been filmed in the best possible way from the available copy.
Problems encountered with this document have been identified here with a check mark ✓.

1. Glossy photographs or pages _____
2. Colored illustrations, paper or print _____
3. Photographs with dark background ✓
4. Illustrations are poor copy _____
5. Pages with black marks, not original copy ✓
6. Print shows through as there is text on both sides of page _____
7. Indistinct, broken or small print on several pages ✓
8. Print exceeds margin requirements _____
9. Tightly bound copy with print lost in spine _____
10. Computer printout pages with indistinct print _____
11. Page(s) _____ lacking when material received, and not available from school or author.
12. Page(s) _____ seem to be missing in numbering only as text follows.
13. Two pages numbered _____. Text follows.
14. Curling and wrinkled pages _____
15. Dissertation contains pages with print at a slant, filmed as received _____
16. Other _____

U·M·I



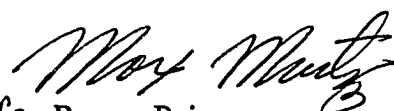
MULTIRESOLUTION REPRESENTATIONS AND WAVELETS

Stephane Mallat

**A DISSERTATION
IN
ELECTRICAL ENGINEERING**

**Presented to the Faculties of the University of Pennsylvania in
Partial Fulfillment of the Requirements for the Degree of
Doctor of Philosophy**

1988


**for Ruzena Bajcsy
Supervisor of Dissertation**


**Sohrab Rabii
Graduate Group Chairperson**

© 1988 Stephane Mallat. All rights reserved.

To my parents.

ACKNOWLEDGEMENTS

I am very grateful to Ruzena Bajcsy who introduced me to computer vision. Her endless enthusiasm and support guided me through the sinuous path of this research. I also wish to thank Yves Meyer, who contributed greatly to the mathematical content of this work, particularly in the second chapter. It was a real pleasure to be part of the interdisciplinary group working on wavelets. The discussions with Ingrid Daubechies were a constant source of ideas for me, and I have enjoyed working with Rafi Coifmann, Alex Grossmann, Stephane Jaffard, Kronland-Martinet, Jean-Phillipe Morel, Jean Morlet, Thierry Paul and Phillippe Tchamitchian.

I received a lot of help from Veronique Arnold, Phillippe Perez, Steve Sherin and Nicolas Treil implementing some of the algorithms described in the thesis. I am also grateful to Max Mintz for reading carefully and correcting the dissertation. During these three years, I enjoyed the support of many other students, faculty and staff among whom were Hellen Anderson, Hugh Durrant-Whyte, Filip Fuma, Alok Gupta, Greg Hager, David Heeger, Knud Henriksen, Keith Henry, Gaylord Holder, Alberto Izaguirre, Robert King, Stane Kovačić, Eric Krotkov, Ray McKendall, David Smitley, John Summers, Frantz Solina, David Talton, Gus Tsikos, Mark Turner, Ira Winston and Kwangyoen Woon.

The friends who helped me escape from this dissertation have been specially important. In particular Anne Abeille, Veronique Arnold, Michel Degraff, Frognette, Eva Illouze, Richard Gerber, Catherine Pelachaud, Yves Schabes, Jean-Luc Vila... Most of all, I am thankful to my parents, who had to cope with me for such a long time.

This research was supported by the following contracts and grants: NSF grant DCR-8410771, Airforce grant AFOSR F49620-85-K-0018, Army/DAAG-29-84-K-0061, NSF-CER/DCR82-19196 Ao2, DARPA/ONR ARPA N0014-85-K-0807, NATO grant 0224/85, NIH 1-R01-HL-29985-01, DEC Corp. and IBM Corp.

ABSTRACT

MULTIRESOLUTION REPRESENTATIONS AND WAVELETS

Stephane Mallat

Supervised by Ruzena Bajcsy

Multiresolution representations are very effective for analyzing the information in images. In this dissertation we develop such a representation for general purpose low-level processing in computer vision. We first study the properties of the operator which approximates a signal at a finite resolution. We show that the difference of information between the approximation of a signal at the resolutions 2^{j+1} and 2^j can be extracted by decomposing this signal on a wavelet orthonormal basis of $L(\mathbb{R}^n)$. In $L^2(\mathbb{R})$, a wavelet orthonormal basis is a family of functions $\left[\sqrt{2^j} \psi(2^j x + n) \right]_{(j,n) \in \mathbb{Z}^2}$, which is built by dilating and translating a unique function $\psi(x)$, called a wavelet. This decomposition defines an orthogonal multiresolution representation called a wavelet representation. It is computed with a pyramidal algorithm of complexity $n \log(n)$. We study the application of this signal representation to data compression in image coding, texture discrimination and fractal analysis. The multiresolution approach to wavelets enables us to characterize the functions $\psi(x) \in L^2(\mathbb{R})$ which generate an orthonormal basis.

The inconvenience of a linear multiresolution decomposition is that it does not provide a signal representation which translates when the signal translates. It is therefore difficult to develop pattern recognition algorithms from such representations. In the second part of the dissertation we introduce a nonlinear multiscale transform which translates when the signal is translated. This representation is based upon the zero-crossings and local energies of a multiscale transform called the dyadic wavelet transform. We experimentally show that this representation is complete and that we can reconstruct the original signal with an iterative algorithm. We study the mathematical properties of this decomposition and show that it is well adapted to computer vision. To illustrate the efficiency of this Energy Zero-Crossings representation, we have developed a coarse to fine matching algorithm on stereo epipolar scan lines. While we stress the applications towards computer vision, wavelets are useful to analyze other types of signal such as speech and seismic-waves.

CONTENT

Introduction	1
Notations	6
Chapter 1 : Orthogonal multiresolution representations	10
1.1. Introduction	10
1.2. Multiresolution transform	11
1.2.1. Multiresolution approximation of $L^2(\mathbb{R})$	11
1.2.2. Implementation of a multiresolution transform	15
1.3. The wavelet representation	20
1.3.1. Detail signal modeling	20
1.3.2. Implementation of an orthogonal wavelet representation	24
1.3.3. Signal reconstruction from an orthogonal wavelet representation	28
1.4. Extension of the orthogonal wavelet representation to images	30
1.4.1. Decomposition and reconstruction algorithms in two dimensions	34
1.5. Applications of the orthogonal wavelet representation	39
1.5.1. Quantization of the orthogonal wavelet representation	39
1.5.2. Texture discrimination and fractal	46
1.6. Distortion with translation	50
Chapter 2 : Multiresolution approximations and wavelet orthonormal bases	51
2.1. Introduction	51
2.2. The scaling function $\phi(x)$	52
2.3. Definition of a multiresolution approximation from $H(0)$	55
2.4. The wavelet orthonormal basis	62
2.5. Approximation error	66
2.6. Separable extension of wavelet orthonormal bases in $L^2(\mathbb{R}^2)$	68
Chapter 3 : Dyadic wavelet Energy Zero-Crossings	70
3.1. Introduction	70
3.2. Dyadic Wavelet transform	71
3.2.1. Smoothing functions and dyadic wavelets	71
3.2.2. Infinite dyadic wavelet transform	75
3.2.3. Finite Dyadic Wavelet Transform	77
3.2.3.1. Finite resolution approximation	77
3.2.3.2. Definition and properties of a finite dyadic wavelet transform	79
3.3. Energy Zero-Crossings Representation	84
3.3.1. Adaptive Sampling : Zero-Crossings	84
3.3.2. Stabilization with local energies	87
3.4. Properties of an Energy Zero-Crossings representation	90

3.4.1. Distance on the Energy Zero-Crossing representation	91
3.4.2. Completeness of the Energy Zero-Crossing representation	93
3.4.3. Continuity of the Energy Zero-Crossing representation	98
3.5. Numerical algorithms	100
3.5.1. Implementation of a finite Energy Zero-Crossing representation	100
3.5.1.1. Dyadic wavelets for discrete algorithms	100
3.5.1.2. Interpolation of a finite resolution approximation	102
3.5.1.3. Implementation of a discrete dyadic wavelet transform	104
3.5.2. Implementation of the Energy Zero-Crossing reconstruction algorithm	106
3.5.2.1. Implementation of a discrete inverse dyadic wavelet transform	106
3.5.2.2. Implementation of the projection operator A^0	109
3.5.2.3. Implementation of a projection operator on Γf	111
3.6. Application of the Energy Zero-Crossing representation to stereo matching	113
3.6.1. Matching algorithm	113
3.6.2. Discussion of the algorithm and results	115
3.7. Dyadic wavelet transform of images	120
3.8. Energy Zero-Crossing representation of images	123
3.8.1. Example of two-dimensional Energy Zero-Crossing representation	128
3.8.2. Application of the Energy Zero-Crossings representation to image segmentation and pattern matching	132
Conclusion and contributions	133
Appendix A	135
Appendix B	137
Appendix C	138
Appendix D	139
Appendix E	140
Appendix F	142
References	144
Index	147

FIGURES

- 1.1. Example of scaling function 15
- 1.2. Multiresolution approximations of a one-dimensional signal 18
- 1.3 Filter H 20
- 1.4 Example of wavelet 22
- 1.5 Wavelet decomposition algorithm for one-dimensional signals 25
- 1.6 Filter G 26
- 1.7 Multiresolution detail signals in one dimension 27
- 1.8 Wavelet reconstruction algorithm for one-dimensional signals 29
- 1.9 Example of reconstructed signal 29
- 1.10 Multiresolution approximation of an image 31
- 1.11 Frequency tunings of a two-dimensional wavelet representation 34
- 1.12 Wavelet representation of the image of a square 35
- 1.13 Wavelet decomposition algorithm for images 36
- 1.14 Wavelet reconstruction algorithm for images 36
- 1.15 Wavelet representation of the image of a train station 37
- 1.16 Wavelet representation of the image of a lady 38
- 1.17 Histogram of a detail image 42
- 1.18 Optimal quantization functions 42
- 1.19 Parameters α and β of the wavelet representation in Fig. 1.16 43
- 1.20 Minimum number of quantization levels 44
- 1.21 Reconstructions for quantized image wavelet representations 45
- 1.22 Wavelet representation of J. Beck textures 47
- 1.23 Wavelet representation of a fractal image 49
- 1.24 Distortion a wavelet representation through translation 50
- 3.1 Example of smoothing function 73
- 3.2 Example of dyadic wavelet 74
- 3.3 Signal measured at the resolution 1 82
- 3.4 Dyadic wavelet decomposition of signal shown in Fig. 3.3 82
- 3.5 Relation between zero-crossings and inflection points 85
- 3.6 Example of straight edges 86
- 3.7 Dyadic decomposition of Fig. 3.6 86
- 3.8 2nd order primitive of the dyadic wavelet shown in Fig. 3.2 86
- 3.9 Construction of an Energy Zero-Crossings representation in one dimension 88
- 3.10 Energy Zero-Crossings representation of the signal shown in Fig. 3.3 90
- 3.11 Reconstruction algorithm from an Energy Zero-Crossings representation 94
- 3.12 Reconstruction of a dyadic wavelet representation from the Energy Zero-Crossings representation shown in Fig. 3.10 97
- 3.13 Reconstruction of the original signal from the reconstruction of Fig. 3.12 97

3.14	Discontinuity of an Energy Zero-Crossings representation	99
3.15	Filters U and G	102
3.16	Interpolation filter	104
3.17	Dyadic wavelet decomposition algorithm	106
3.18	Dyadic wavelet reconstruction algorithm	108
3.19	Orthogonal projection filters	110
3.20	Implementation of the operator $P_{\Gamma\Gamma}$	112
3.21	Horizontal epipolar geometry of stereo images	114
3.22	Pair of stereo epipolar scan lines of an image	117
3.23	Energy Zero-Crossings representation of the epipolar lines of Fig. 3.22	117
3.24	Coarse to fine matching of a pair of epipolar lines	118 119
3.25	Symmetrical repartition of the frequency support of a dyadic wavelet family	121
3.26	Frequency support of a two-dimensional dyadic wavelet	122
3.27	Drawing of a two-dimensional dyadic wavelet representation	124
3.28	Zero-crossings curves	125
3.29	Construction of an Energy Zero-Crossings representation in two dimensions	125
3.30	Example of frequency support repartition of a dyadic wavelet family	129
3.31	Dyadic wavelet and Energy Zero-Crossings surfaces of an image	131

INTRODUCTION

In computer vision, it is difficult to analyze the information content of an image directly from the grey level intensity of the image pixels. Indeed, this value depends upon the lighting conditions. More important are the local variations of the image intensity. From the image contrast, we can extract some important features such as the edges of the structures embedded in the image. At the border of such structures, the image intensity is likely to be suddenly modified. The local variations have therefore a high amplitude. A. Rosenfeld and M. Thurston [42] have shown that the size of the neighborhood where the contrast is computed must be adapted to the size of the objects that we want to analyze. This size defines a resolution of reference for measuring the local variations of the image. Generally, the structures we want to recognize have very different sizes. Hence, it is not possible to define a priori an optimal resolution for analyzing images. Several researchers [17, 34, 43] have developed pattern matching algorithms which process the image at different resolutions. For this purpose, J. Crowley [6] and P. Burt [5] have proposed to reorganized the image information into a set of details appearing at different resolutions. Given a sequence of increasing resolutions $\{r_j\}_{j \in \mathbb{Z}}$, the details of $f(x)$ at the resolution r_j is defined as the difference of information between the approximation of $f(x)$ at the resolution r_j and the approximation at the lower resolution r_{j-1} . The variations of the image at the resolution r_j can be measured from the energy of the image details at the same resolution. At different resolutions, the details of an image generally characterize different physical structures of the scene. For example, a coarse resolution satellite image of a coast gives a description of only the overall shape of the coast. When the resolution of the image is increased, we are able to successively distinguish the local relief of the region, and if the resolution gets even finer we can recognize the different types of local vegetation. Hence, by extracting the difference of information between two successive resolutions, we separate the information corresponding to the coast contour, the relief and the vegetation. This is of course a very simplistic example, but it gives the overall idea of this approach.

A multiresolution decomposition enables us to have a scale-invariant interpretation of the image. The scale of the image is a very important parameter which varies depending upon the distance between the scene and the optical center of the camera. If the camera moves towards

the scene, our interpretation of the scene should not be modified. This scale invariance is a well known property of the human visual system [4, 47]. Our perception of visual information does not depend upon the size of the image projected on the retina. This principle is limited to a finite range of scale defined by the minimum grain which can be perceived by the retina and by the extent of the visual field. A scaling invariance can be obtained in a multiresolution representation if the sequence of resolution parameters $\{r_j\}_{j \in \mathbb{Z}}$ varies exponentially. This means that there exists a resolution step $\alpha \in \mathbb{R}$ such that for all integers j , $r_j = \alpha^j$. Let $f(x)$ be the image of a given scene, and let us suppose that we have computed the details of this image at each resolution α^j . If we get α times closer to the scene, each object of the scene is projected on an area α^2 times smaller in the focal plane of the camera. That is, each object is measured at a resolution α times smaller. The details of this new image at the resolution α^j therefore correspond to the details of the previous image at the resolution α^{j-1} . Changing the scale of the image only translates the image details along the resolution axis. If we similarly analyze the details at all resolutions, the interpretation of the image information is not modified.

A multiresolution representation provides a simple hierarchical framework for interpreting the image information [23]. In some sense, the details of the image at a coarse resolution provide the "context" of the image whereas the finer details correspond to the particular "modalities". For example, it is difficult to recognize that a small rectangle inside an image is the window of a house if we did not previously recognize the house "context". It is therefore natural first to analyze the image details at a coarse resolution and then increase the resolution. This is called a coarse to fine processing strategy. At a coarse resolution, the image details are characterized by very few samples. Hence, the coarse information processing can be performed quickly. The finer details are characterized by more samples and thus take longer to analyze. However, the prior information derived from the context constrains and thus speeds up the computations at finer resolutions. The coarse to fine strategy also enable us to process the minimum amount of details which are necessary to perform a recognition task. Indeed, if we can recognize an object from a coarse description, we do not analyze the finer details. For example, in order to distinguish a car from a house, the coarse details of the image should be enough. Such a strategy is efficient for pattern recognition algorithms. It has already been widely studied for low level image processing such as stereo matching and template matching [15, 17].

P. Burt [5] and J. Crowley [6] have found an elegant pyramidal implementation for computing the signal details at different resolutions. In order to simplify the computations, P. Burt has chosen a resolution step α equal to 2. The details at each resolution 2^j are calculated by filtering the original image with the difference of two low-pass filters and by sub-sampling the resulting image by a factor 2^j . This operation is performed over a finite range of resolutions. In this implementation, the difference of low-pass filters gives an approximation of the Laplacian of a Gaussian. The details at different resolutions are regrouped into a pyramid structure called the Laplacian pyramid. As implemented by P. Burt and J. Crowley, the details of the image at the resolution 2^j do not correspond exactly to the difference of information between the image approximations at the resolution 2^{j+1} and 2^j . At different resolutions, the details of the Laplacian pyramid are correlated. There is no clear model which handles this correlation. It is thus difficult to know whether a similarity between the image details at different resolutions is due to a property of the image itself or to the intrinsic redundancy of the representation. Another inconvenience of this multiresolution representation is that it does not introduce any spatial orientation selectivity into the decomposition process. It is important to locally characterize the spatial orientation of a signal for pattern recognition problems such as texture discrimination [22].

In the first chapter, we study the mathematical properties of the operator which transforms a function into an approximation at a resolution 2^j . We show that the information which exist in a function approximated at the resolution 2^{j+1} but does not appear at the resolution 2^j is extracted by decomposing this function in a wavelet orthonormal basis. This decomposition defines a complete and orthogonal multiresolution representation called the wavelet representation. Wavelets have been introduced by A. Grossmann and J. Morlet [16] as functions $\psi(x)$, whose translates and dilates $\psi(sx+t)$ could be used for expansions of $L^2(\mathbb{R})$ functions. In the wavelet decomposition defined by A. Grossmann and J. Morlet, the scale coefficient s and the translation coefficient t vary over the whole set of real numbers \mathbb{R} . I. Daubechies [8] has shown that for some particular wavelets $\psi(x)$, if the coefficients s and t vary on a discrete sub-set $F \subset \mathbb{R}^2$ called a frame, then the family of functions $\left[\sqrt{s} \psi(sx+t) \right]_{(s,t) \in F}$ is a basis of $L^2(\mathbb{R})$. A very important particular case was found by Y. Meyer [37] who proved that there exist some wavelets $\psi(x)$ such that $\left[\sqrt{2^j} \psi(2^j x - k) \right]_{(j,k) \in \mathbb{Z}^2}$ is an orthonormal basis of

$L^2(\mathbb{R})$. These bases generalize the Haar basis, and Y. Meyer has shown that there exists such functions $\psi(x)$ which are much smoother than the Haar function. The wavelet orthonormal bases provide an important new tool in functional analysis. Indeed, it was believed that there did not exist such simple orthonormal bases of $L^2(\mathbb{R})$ whose elements had a good localization both in the spatial and Fourier domains. These bases have already found many applications in pure and applied mathematics [21, 26], in quantum mechanics [11] and signal analysis [24]. From a mathematical point of view, the multiresolution approach to wavelets enables us to characterize the functions $\psi(x) \in L^2(\mathbb{R})$ which generate an orthonormal basis. The mathematical description of this model is given in chapter 2.

We develop a pyramidal algorithm of complexity $n \log(n)$ which computes the decomposition of a signal in a wavelet orthonormal basis. The signal can also be reconstructed from such a decomposition with a pyramidal algorithm. In the last two paragraphs of chapter 1, we study the applications of the wavelet representation to image processing. We develop an optimal quantization of the wavelet representation, and show that we get very good data compression for coding images. In two dimensions, the orthogonal wavelets locally discriminate the spatial orientation of the signal. We discuss the application to texture segmentation and then prove that we can compute the fractal dimension of a Brownian fractal from its decomposition in a wavelet orthonormal basis.

In order to define a general purpose image representation for computer vision applications, the multiresolution decomposition must satisfy some basic properties that we discuss here. First, we do not want to throw away a priori any information provided by the original image. In general, not all the information available in an image is needed for solving a particular recognition problem. However, the information which can be removed is task dependent. For general applications, the representation must therefore be complete. Another important requirement is to have a representation which is stable with respect to noise. This is necessary in order to build robust algorithms from such a decomposition. Hence, any slight perturbation of the original image should produce only a small perturbation of the image representation and vice-versa. For pattern recognition, we must compare some sub-parts of the image with a given model. This implies the possibility of quantifying the differences between the representation of two local signals with a meaningful distance measure. A priori the pattern that we want to analyze can be located anywhere in the image. The representation of a signal should not depend

upon the spatial positioning of the signal. When a signal translates, its representation should therefore translate without being distorted.

At the end of chapter 1 , we show that when a signai is translated, the orthogonal wavelet representation is not translated but significantly modified. Hence, the characterization of a pattern depends upon the location of this pattern within the image. This property is shared by all the pyramidal multiresolution representations. It is thus difficult to develop any pattern recognition algorithm from such multiresolution representations. In chapter 3 we define a nonlinear multiscale transform which does translate when the signal translates. This new representation is based on the zero-crossings and local energies of a dyadic wavelet representation. In the first part of chapter 3, we formally define a dyadic wavelet representation and study its most important mathematical properties. We describe a discrete pyramidal algorithm of complexity $n \log(n)$ for for implementing this decomposition. The inverse operator which reconstructs the signal from the dyadic wavelet transform is implemented with a similar algorithm. We then build a new discrete representation from the zero-crossings and local energy values of the dyadic wavelet transform of a signal. This Energy Zero-Crossing representation is similar to a multiresolution representation in the sense that it characterizes the details of the signal at different scales. However, it is defined through a nonlinear transform which does translate when the signal translates. If the wavelet is the second derivative of a smooth function, the zero-crossings of the dyadic wavelet transform provide the locations of the signal "edges". In this chapter we show in particular that such a representation is complete for one-dimensional signals. We describe an iterative algorithm which reconstructs the original signal from the zero-crossings and local energies of the dyadic wavelet transform. In order to illustrate the application of the Energy Zero-Crossing representation, we have developed a stereo-matching algorithm for image epipolar scan lines. In the final part of chapter 3, we extend the Energy Zero-Crossing model to two-dimensional signals and discuss its applications to low-level operations in computer vision.

In chapters 1 and 3, we first develop the mathematical foundations of our representations for one-dimensional signals, and then extend the model to two dimensions for computer vision applications. Although we emphasize the computer vision applications, we believe that the signal decompositions studied in this dissertation can find some applications in other domains such as speech and seismic-wave analysis.

NOTATION

Z and **R** respectively denote the set of integers and real numbers.

Notation for one-dimensional signals

Let $\mathbf{L}^2(\mathbf{R})$ denote the vector space of measurable, square-integrable one-dimensional functions $f(x)$. For a pair of functions $f(x) \in \mathbf{L}^2(\mathbf{R})$, $g(x) \in \mathbf{L}^2(\mathbf{R})$, the inner product of $f(x)$ with $g(x)$ is written

$$\langle g(u), f(u) \rangle = \int_{-\infty}^{+\infty} g(u) f(u) du .$$

The norm of $f(x)$ in $\mathbf{L}^2(\mathbf{R})$ is given by

$$\|f\|^2 = \int_{-\infty}^{+\infty} |f(u)|^2 du .$$

We denote the convolution of two functions $f(x) \in \mathbf{L}^2(\mathbf{R})$ and $g(x) \in \mathbf{L}^2(\mathbf{R})$ by

$$f * g(x) = (f(u) * g(u))(x) = \int_{-\infty}^{+\infty} f(u) g(x-u) du .$$

An element of $\mathbf{L}^2(\mathbf{R})$ is a class of functions which are equal outside a set of points of measure zero. If such a class admits a continuous representative, we always chose this representative and are thus able to define the value of a continuous $\mathbf{L}^2(\mathbf{R})$ function at any point. The vector space **C** denotes the space of all the functions of $\mathbf{L}^2(\mathbf{R})$ which are continuous.

Cⁿ denotes the space of all the functions of $\mathbf{L}^2(\mathbf{R})$ which are n times continuously differentiable. When $n = \infty$, this space is written **C[∞]**.

H^s denotes a Sobolev space.

{ 0 } denotes the null space.

L²(Z) the vector space of square-summable sequences :

$$\mathbf{L}^2(\mathbf{Z}) = \left\{ (\alpha_i)_{i \in \mathbf{Z}} : \sum_{i=-\infty}^{+\infty} |\alpha_i|^2 < \infty \right\} .$$

$(L^2(\mathbb{R}))^{\mathbb{Z}}$ is the vector space of all infinite sequences $\left[g_j(x) \right]_{j \in \mathbb{Z}}$ of $L^2(\mathbb{R})$ functions such that

$$\sum_{j \in \mathbb{Z}} \|g_j\|^2 < \infty .$$

The summation $\left(\sum_{j \in \mathbb{Z}} \|g_j\|^2 \right)^{1/2}$ defines a norm on $(L^2(\mathbb{R}))^{\mathbb{Z}}$.

$(L^2(\mathbb{R}))^n$ denotes the vector space of finite sequences $\left[g_j(x) \right]_{1 \leq j \leq n}$ of n $L^2(\mathbb{R})$ functions.

The dilation of a function $f(x) \in L^2(\mathbb{R})$ by a scaling factor 2^j is written

$$f^j(x) = 2^j f(2^j x) .$$

The reflection of $f(x)$ about 0 is written

$$\tilde{f}(x) = f(-x) .$$

The Fourier transform of $f(x) \in L^2(\mathbb{R})$ is written $\hat{f}(\omega)$ and is defined by

$$\hat{f}(\omega) = \int_{-\infty}^{+\infty} f(x) e^{-i\omega x} dx .$$

For any vector space $V \subset L^2(\mathbb{R})$, we denote by FV the image V under the Fourier transform.

If X is an operator from $L^2(\mathbb{R})$ into $L^2(\mathbb{R})$, then for any $f(x) \in L^2(\mathbb{R})$, the image of $f(x)$ by X is written

$$Xf(x) = X(f(u))(x) .$$

Notation for two-dimensional signals

We denote by $L^2(\mathbb{R}^2)$ the vector space of measurable, square-integrable two dimensional functions $f(x,y)$. For a pair of functions $f(x,y) \in L^2(\mathbb{R}^2)$, $g(x,y) \in L^2(\mathbb{R}^2)$, the inner product of $f(x,y)$ with $g(x,y)$ is written

$$\langle f(x,y), g(x,y) \rangle = \int_{-\infty}^{+\infty} \int_{-\infty}^{+\infty} f(x,y) g(x,y) dx dy .$$

The norm of $f(x,y)$ in $L^2(\mathbb{R}^2)$ is given by

$$\|f\|^2 = \int_{-\infty}^{+\infty} \int_{-\infty}^{+\infty} |f(x,y)|^2 dx dy .$$

$L^2(\mathbb{Z}^2)$ is the vector space of square-summable discrete sequences which depend upon two parameters

$$L^2(\mathbb{Z}^2) = \left\{ (\alpha_{n,m})_{(n,m) \in \mathbb{Z}^2} : \sum_{n=-\infty}^{+\infty} \sum_{m=-\infty}^{+\infty} |\alpha_{n,m}|^2 < +\infty \right\} .$$

$(L^2(\mathbb{R}^2))^{\mathbb{Z}}$ is the vector space of all infinite sequences $\left[g_j(x,y) \right]_{j \in \mathbb{Z}}$ of $L^2(\mathbb{R})$ functions such that

$$\sum_{j \in \mathbb{Z}} \|g_j\|^2 < +\infty .$$

$(L^2(\mathbb{R}^2))^n$ denotes the vector space of finite sequences $\left[g_j(x,y) \right]_{1 \leq j \leq n}$ of $L^2(\mathbb{R})$ functions.

The dilation of a function $f(x,y) \in L^2(\mathbb{R}^2)$ by a scaling factor 2^j is written

$$f^j(x,y) = 2^{2j} f(2^j x, 2^j y) .$$

The Fourier transform of $f(x,y) \in L^2(\mathbb{R}^2)$ is written $\hat{f}(\omega_x, \omega_y)$ and is defined by

$$\hat{f}(\omega_x, \omega_y) = \int_{-\infty}^{+\infty} \int_{-\infty}^{+\infty} f(x,y) e^{-i(\omega_x x + \omega_y y)} dx dy .$$

Operators defined in the dissertation

A^j : computes the approximation of a function at the resolution 2^j .

S^j : smooth a function at the scale 2^j .

W^j : dyadic wavelet transform at the scale 2^j .

W_F : finite dyadic wavelet transform.

W_I : infinite dyadic wavelet transform.

P_X : projection on a particular vector space X .

Functions defined in the dissertation

$\phi(x)$: scaling function.

$\psi(x)$: wavelet.

$\theta(x)$: smoothing function.

Vector spaces defined in the dissertation

V_j : subspace of $L^2(\mathbb{R})$ (or $L^2(\mathbb{R}^2)$) , consisting of all functions approximated at the resolution 2^j .

O_j : orthogonal complement of V_j in V_{j+1} .

F : Vector space of all finite wavelet transforms .

I : Vector space of all infinite wavelet transforms .

CHAPTER 1

ORTHOGONAL MULTIRESOLUTION REPRESENTATIONS

1.1. Introduction

In this chapter we define an orthogonal multiresolution representation called the wavelet representation [30]. We interpret mathematically the intuitive properties that one would expect from an operator which transforms a function $f(x) \in L^2(\mathbb{R})$ into its approximation at the resolution 2^j . Then, we show that the information which exist in a function approximated at the resolution 2^{j+1} but does not appear at the resolution 2^j is extracted by decomposing this function in a wavelet orthonormal basis. This decomposition defines a wavelet representation. It can be efficiently computed with a pyramidal algorithm similar to P. Burt's [5] algorithm. We first study the wavelet decomposition of one-dimensional signals and then extend the model to images. In two dimensions, the wavelet representation has a spatial orientation selectivity. We describe the applications of this multiresolution representation to data compression in image coding, to texture discrimination and to fractal analysis. In this chapter, we give no theorem proof and avoid the mathematical technical details. We rather try to illustrate the practical implications of the model. The mathematical foundations are more thoroughly described in chapter 2.

1.2. Multiresolution transform

In this paragraph, we study the concept of multiresolution decomposition for one-dimensional signals. The model is extended to two dimensions in paragraph 1.4.

1.2.1. Multiresolution approximation of $L^2(\mathbb{R})$

Let A^j be the operator which approximates a signal at a resolution 2^j . We suppose that our original signal $f(x)$ is measurable and has a finite energy : $f(x) \in L^2(\mathbb{R})$. In this paragraph, we characterize A^j by the properties one would expect from such an approximation.

- A^j is a linear operator. If $A^j f(x)$ is the approximation of some function $f(x)$ at the resolution 2^j , $A^j f(x)$ is not modified if we approximate it again with the operator A^j . This principle shows that $A^j \circ A^j = A^j$. The operator A^j is thus a projection operator on a particular vector space $\mathbf{V}_j \subset L^2(\mathbb{R})$. \mathbf{V}_j is the set of all the signal approximated at resolution 2^j .
- Among all the approximated functions at the resolution 2^j , $A^j f(x)$ is the function which is the most similar to $f(x)$.

$$\forall g(x) \in \mathbf{V}_j \quad , \quad \|g(x) - f(x)\| \geq \|A^j f(x) - f(x)\| . \quad (1.1)$$

The operator A^j is thus an orthonormal projection on the vector space \mathbf{V}_j .

- The approximation of a signal at resolution 2^{j+1} contains all the necessary information to build the same signal at a smaller resolution 2^j . This is a causality property.
Since A^j is a projection operator on \mathbf{V}_j this principle is equivalent to :

$$\forall j \in \mathbb{Z} , \quad \mathbf{V}_j \subset \mathbf{V}_{j+1} . \quad (1.2)$$

- An approximation operation is similar at all resolutions.

The spaces of approximated functions should thus be derived from one another by scaling each approximated function by the ratio of the resolution values.

$$\forall j \in \mathbb{Z}, \quad g(x) \in \mathbf{V}_j \iff g(2x) \in \mathbf{V}_{j+1}. \quad (1.3)$$

- The approximation $A^j f(x)$ of a signal $f(x)$ can be characterized by 2^j samples per length unit. When $f(x)$ is translated by a length proportional to 2^{-j} , $A^j f(x)$ is translated and it is characterized by the same samples which have been translated.

Because of the condition (1.3), it is sufficient to express the above principle for $j = 0$. This statement can be modeled as follows.

Discrete characterization :

$$\text{There exists an isomorphism } I_0 \text{ from } \mathbf{V}_0 \text{ onto } L^2(\mathbb{Z}), \quad (1.4)$$

$$\text{where } L^2(\mathbb{Z}) = \{ (\alpha_i)_{i \in \mathbb{Z}} : \sum_{i=-\infty}^{+\infty} |\alpha_i|^2 < \infty \}.$$

Translation of the approximation :

$$\forall k \in \mathbb{Z}, \text{ let } f_k(x) = f(x-k), \quad A^j f_k(x) = A^j f(x-k). \quad (1.5)$$

Translation of the samples :

$$I_0(A^j f(x)) = (\alpha_i)_{i \in \mathbb{Z}} \iff I_0(A^j f_k(x)) = (\alpha_{i-k})_{i \in \mathbb{Z}}. \quad (1.6)$$

- When computing an approximation of $f(x)$ at a resolution 2^j , some information about $f(x)$ is lost. This lost information corresponds to the orthonormal projection of $L^2(\mathbb{R})$ on the orthogonal complement of \mathbf{V}_j in $L^2(\mathbb{R})$. However, when the resolution increases to $+\infty$ the approximated signal should converge to the original signal. Conversely when the resolution decreases to zero, the approximated signal contains less and less information and converges to zero.

Since the approximated signal at a resolution 2^j is equal to the orthogonal projection on a space \mathbf{V}_j , this principle can be written :

$$\bigcup_{j=-\infty}^{+\infty} \mathbf{V}_j \text{ is dense in } L^2(\mathbb{R}), \quad \text{and} \quad \bigcap_{j=-\infty}^{+\infty} \mathbf{V}_j = \{ 0 \}. \quad (1.7)$$

We call any set of vector spaces $\left[\mathbf{V}_j \right]_{j \in \mathbb{Z}}$ which satisfies the properties (1.2) to (1.7) a **multiresolution approximation** of $L^2(\mathbb{R})$. We have shown that the concept of approximation at a resolution 2^j is defined with respect to a multiresolution approximation of $L^2(\mathbb{R})$. Let us

give a simple example of multiresolution approximation of $L^2(\mathbb{R})$.

Example

Let \mathbf{V}_0 be the vector space of all the functions of $L^2(\mathbb{R})$ which are constant on each interval $[k, k+1]$, for any $k \in \mathbb{Z}$. Equation (1.3) implies that \mathbf{V}_j is the vector space of all the functions of $L^2(\mathbb{R})$ which are constant on each interval $[k2^{-j}, (k+1)2^{-j}]$, for any $k \in \mathbb{Z}$. The condition (1.2) is clearly verified. We can define an isomorphism I_0 which satisfies properties (1.4), (1.5) and (1.6) by associating to any function $f(x) \in \mathbf{V}_0$ the sequence $(\alpha_k)_{k \in \mathbb{Z}}$ such that α_k equals the value of $f(x)$ on the interval $[k, k+1]$. We know that the vector space of piecewise constant functions is dense in $L^2(\mathbb{R})$. Hence, we can derive that $\bigcup_{j=-\infty}^{+\infty} \mathbf{V}_j$ is dense in $L^2(\mathbb{R})$. It is clear as well that $\bigcap_{j=-\infty}^{+\infty} \mathbf{V}_j = \{0\}$, so the sequence of vector spaces $[\mathbf{V}_j]_{j \in \mathbb{Z}}$ is a multiresolution approximation of $L^2(\mathbb{R})$. The inconvenience of this multiresolution approximation is that the functions of the vector spaces \mathbf{V}_j are not regular. They are not even continuous. For many applications we want a smooth approximate of a function. In appendix A, we describe a class of multiresolution approximations where the functions of each space \mathbf{V}_j are n times continuously differentiable.

We saw that the approximation operator A^j is equal to the orthogonal projection on the vector space \mathbf{V}_j . In order to numerically characterize this operator, we must find an orthonormal basis of \mathbf{V}_j . The following theorem shows that such an orthonormal basis can be defined by scaling and translating a unique function $\phi(x)$.

Theorem 1.1

Let $[\mathbf{V}_j]_{j \in \mathbb{Z}}$ be a multiresolution approximation of $L^2(\mathbb{R})$. There exists a unique function $\phi(x) \in L^2(\mathbb{R})$ called a scaling function such that for any $j \in \mathbb{Z}$, if we denote by $\phi^j(x) = 2^j \phi(2^j x)$ the scaling of $\phi(x)$ by 2^j , then

$$\left[\sqrt{2^{-j}} \phi^j(x - 2^{-j}n) \right]_{n \in \mathbb{Z}} \text{ is an orthonormal basis of } \mathbf{V}_j. \quad (1.8)$$

The proof of this theorem can be found in chapter 2. We can therefore build an orthonormal basis of any \mathbf{V}_j by scaling the function $\phi(x)$ with a coefficient 2^j and translating the resulting function on a grid whose interval is proportional to 2^{-j} . The coefficient $\sqrt{2^{-j}}$ is adjusted for normalization purposes. For a given multiresolution approximation $\left[\mathbf{V}_j\right]_{j \in \mathbb{Z}}$, there exists a unique scaling function $\phi(x)$ which satisfies (1.8). However, for different multiresolution approximations, the scaling functions are different. Fig. 1.1 shows an example of an exponentially decreasing scaling function. Its Fourier transform has the shape of a low-pass filter. It corresponds to a multiresolution approximation of $L^2(\mathbb{R})$ which is built from cubic splines. This scaling function is further described in appendix A.

The orthogonal projection on \mathbf{V}_j can now be computed by decomposing the signal $f(x)$ on the orthonormal basis given by theorem 1.1.

$$\forall f(x) \in L^2(\mathbb{R}) \quad A^j f(x) = 2^{-j} \sum_{n=-\infty}^{+\infty} \langle f(u), \phi^j(u - 2^{-j}n) \rangle \phi^j(x - 2^{-j}n) \quad (1.9)$$

The approximation of the signal $f(x)$ at the resolution 2^j is thus characterized by the set of inner products

$$A^j f_d = \left[\langle f(u), \phi^j(u - 2^{-j}n) \rangle \right]_{n \in \mathbb{Z}}. \quad (1.10)$$

$A^j f_d$ is called a discrete approximation of $f(x)$ at the resolution 2^j . Since computers can only process discrete signals, we must work with these discrete approximations, which characterize the continuous approximations $A^j f(x)$. The discrete approximation of $f(x)$ at the resolution 2^j can also be viewed as a uniform sampling of $f(x)$ filtered by the low-pass filter $\tilde{\phi}^j(x) = \phi^j(-x)$. Indeed, each inner product can be interpreted as a convolution product evaluated at a point $2^{-j}n$:

$$\langle f(u), \phi^j(u - 2^{-j}n) \rangle = \int_{-\infty}^{+\infty} f(u) \phi^j(u - 2^{-j}n) du = (f(u) * \phi^j(-u))(2^{-j}n). \quad (1.11)$$

We can rewrite $A^j f_d$:

$$A^j f_d = \left[(f(x) * \phi^j(-x))(2^{-j}n) \right]_{n \in \mathbb{Z}}. \quad (1.12)$$

It is not surprising that the computation of a discrete approximation corresponds to a low-pass

filtering. Indeed, by removing the details of $f(x)$ smaller than 2^{-j} , we suppress the highest frequencies of this function. However, the scaling function $\phi(x)$ is a very particular low-pass filter since the family of functions $\left[\sqrt{2^{-j}} \phi^j(x - 2^{-j}n) \right]_{n \in \mathbb{Z}}$ is an orthonormal family.

In the next paragraph we show that the discrete approximation of $f(x)$ at the resolution 2^j can be computed with a pyramidal algorithm.

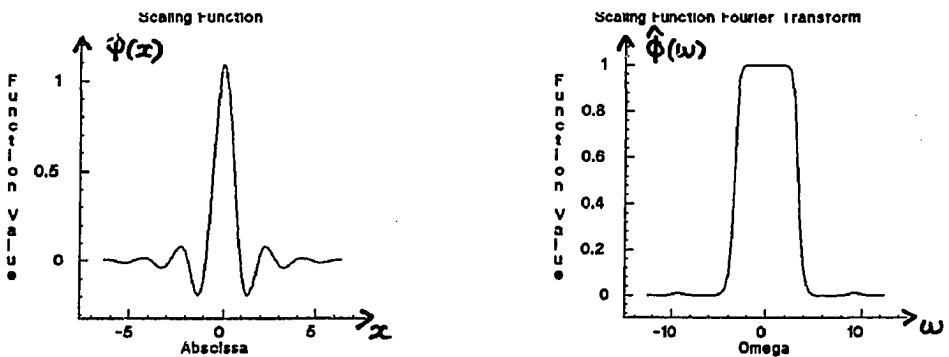


Fig. 1.1. Example of scaling function with its Fourier transform. It decreases exponentially in the spatial domain and as $\frac{1}{\omega^4}$ in the frequency domain.

1.2.2. Implementation of a multiresolution transform

In practice, a signal measuring device low-passes the continuous input signal, and a digitizer outputs a uniform sampling. Hence, this measurement corresponds to an approximation of the original signal at a finite resolution. For normalization purposes, we suppose that this resolution is equal to 1. Let $A^0 f_d$ be the discrete approximation at the resolution 1 of the signal we want to decompose. The causality principle says that from $A^0 f_d$ we can compute all the $A^j f_d$ for $j < 0$. In this paragraph, we describe a simple iterative algorithm for calculating these discrete approximations.

Let $\left[V_j \right]_{j \in \mathbb{Z}}$ be a multiresolution approximation and $\phi(x)$ be the corresponding scaling function. The family of functions $\left[\sqrt{2^{-j-1}} \phi^{j+1}(x - 2^{-j-1}k) \right]_{k \in \mathbb{Z}}$ is an orthonormal basis

of \mathbf{V}_{j+1} . We know that for any $n \in \mathbf{Z}$, the function $\phi^j(x - 2^{-j}n)$ is a member of \mathbf{V}_j which is included in \mathbf{V}_{j+1} . $\phi^j(x - 2^{-j}n)$ can thus be expanded in this orthonormal basis of \mathbf{V}_{j+1} :

$$\phi^j(x - 2^{-j}n) = 2^{-j-1} \sum_{k=-\infty}^{+\infty} \langle \phi^j(u - 2^{-j}n), \phi^{j+1}(u - 2^{-j-1}k) \rangle \phi^{j+1}(x - 2^{-j}k). \quad (1.13)$$

Each of the inner products $\langle \phi^j(u - 2^{-j}n), \phi^{j+1}(u - 2^{-j-1}k) \rangle$ verifies

$$2^{-j-1} \langle \phi^j(u - 2^{-j}n), \phi^{j+1}(u - 2^{-j-1}k) \rangle = \frac{1}{2} \langle \phi^{-1}(u), \phi(u - (k - 2n)) \rangle. \quad (1.14)$$

This can easily be shown by changing variables in the left inner product integral. By computing the inner products of $f(x)$ with both sides of equation (1.13) we get

$$\langle f(u), \phi^j(u - 2^{-j}n) \rangle = \sum_{k=-\infty}^{+\infty} \langle f(u), \phi^{j+1}(u - 2^{-j-1}k) \rangle \frac{1}{2} \langle \phi^{-1}(u), \phi(u - (k - 2n)) \rangle.$$

Let H be a discrete filter with impulse response

$$h(n) = \frac{1}{2} \langle \phi^{-1}(u), \phi(u - n) \rangle, \quad n \in \mathbf{Z}, \quad (1.16)$$

and let \tilde{H} be the mirror filter with impulse response $\tilde{h}(n) = h(-n)$,

$$\langle f(u), \phi^j(u - 2^{-j}n) \rangle = \sum_{k=-\infty}^{+\infty} \langle f(u), \phi^{j+1}(u - 2^{-j-1}k) \rangle \tilde{h}(2n - k). \quad (1.17)$$

Equation (1.17) shows that $A^j f_d$ can be computed by convolving $A^{j+1} f_d$ with \tilde{H} and keeping every other sample of the output. All the discrete approximations $A^j f_d$ for $j < 0$ can thus be computed from $A^0 f_d$ by repeating this process. This operation is called a pyramid transform. The algorithm is illustrated by a block diagram in Fig. 1.5.

In practice, the measuring device gives only a finite number N of samples : $A^0 f_d = [\alpha_n]_{1 \leq n \leq N}$. Each discrete signal $A^j f_d$ ($j < 0$) has $2^j N$ samples. In order to avoid any border problem when computing the discrete approximations $A^j f_d$, we suppose that the original signal $A^0 f_d$ is symmetrical with respect to $n = 0$ and $n = N$:

$$\alpha_n = \begin{cases} \alpha_{-n} & \text{if } -N < n < 0 \\ \alpha_{2N-n} & \text{if } 0 < n < N \end{cases}.$$

If the impulse response of the filter \tilde{H} is even ($\tilde{H} = H$), each discrete approximation $A^j f_d$

will also be symmetrical with respect to $n = 0$ and $n = 2^{-jN}$. Fig. 1.2 shows the discrete approximated signal $A^j f_d$ of a continuous signal $f(x)$, for $j = 0, -1, -2, -3$. These discrete approximated signals have been computed with the algorithm previously described. We have approximated the impulse response of the filter H shown in Fig. 1.3 by taking $h(n) = 0$ for $|n| > 8$. The continuous approximated signals $A^j f(x)$ have been calculated with equation (1.9). As the resolution decreases the smaller details of $f(x)$ gradually disappear.

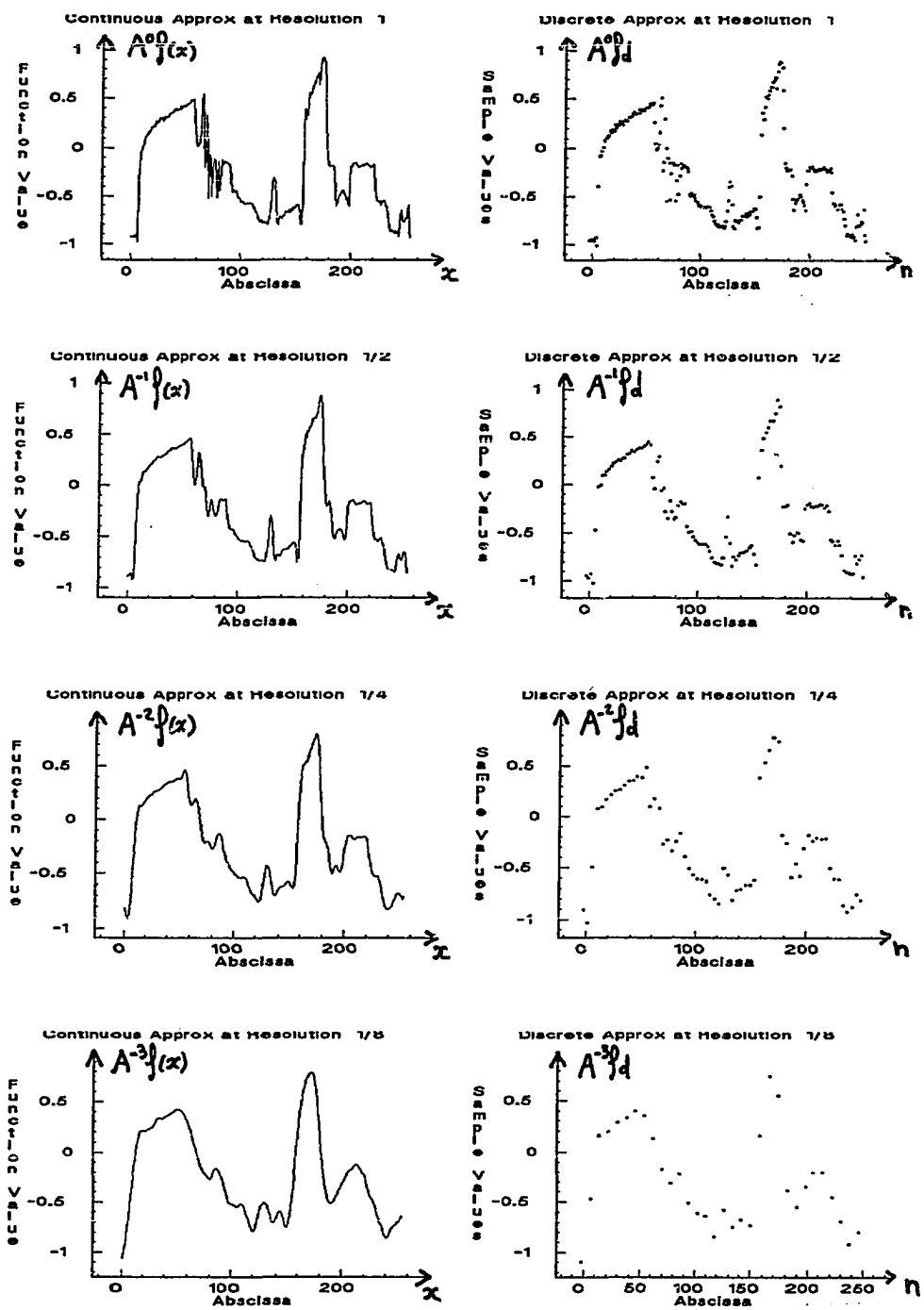


Fig. 1.2. The left and right images are respectively the graphs of $A^j f_d$ and $A^j f(x)$ for $j = 0, -1, -2, -3$ (resolution 1, 1/2, 1/4, 1/8). As the resolution decreases smaller details gradually disappear.

We have shown in theorem 1.1 that a multiresolution approximation $\left[\mathbf{V}_j \right]_{j \in \mathbb{Z}}$ is completely characterized by the a scaling function $\phi(x)$. In general, a scaling function is a function $\phi(x) \in L^2(\mathbb{R})$ such that , for all $j \in \mathbb{Z}$, $\left[\sqrt{2^{-j}} \phi^j(x - 2^{-j}n) \right]_{n \in \mathbb{Z}}$ is an orthonormal family, and if \mathbf{V}_j is the vector space generated by this family of functions, then $\left[\mathbf{V}_j \right]_{j \in \mathbb{Z}}$ is a multiresolution approximation of $L^2(\mathbb{R})$. The following theorem gives a practical characterization of the Fourier transform of a scaling function.

Theorem 1.2

Let $\phi(x)$ be a scaling function, and let H be a discrete filter with impulse response $h(n) = \frac{1}{2} \langle \phi^{-1}(u), \phi(u-n) \rangle$. Let $H(\omega)$ be the Fourier series defined by

$$H(\omega) = \sum_{n=-\infty}^{+\infty} h(n) e^{-in\omega} . \quad (1.18)$$

$H(\omega)$ satisfies the following two properties :

- (a) $H(\omega)$ is 2π periodic and $|H(0)| = 1$.
- (b) $|H(\omega)|^2 + |H(\omega+\pi)|^2 = 1$.

Conversely let $H(\omega)$ be a function satisfying (a) and (b) , such that

- (c) $|H(\omega)| \neq 0$ for $\omega \in [0, \pi/2]$.

The function defined by

$$\hat{\phi}(\omega) = \prod_{p=1}^{+\infty} H(2^{-p}\omega) \quad (1.19)$$

is the Fourier transform of a scaling function.

The proof of this theorem is given in chapter 2. The filters which satisfy property (b) are called **conjugate filters**. We can find an extensive description of such filters and numerical methods to synthesize them in the signal processing literature [10, 38, 41]. Given a conjugate filter H which satisfies (a) , (b) and (c) we can then compute the Fourier transform of the corresponding scaling function with equation (1.18) . It is possible to choose $H(\omega)$ in order to have a scaling function $\phi(x)$ which is well localized in both the frequency and spatial domains. Appendix A describes a class of symmetrical scaling functions which are exponentially

decreasing and whose Fourier transforms decrease as $\frac{1}{\omega^n}$, for $n \in \mathbb{N}$. The scaling function shown in Fig. 1.1 is one of these. Fig. 1.3 shows the filter H associated with the scaling function given in Fig. 1.1.

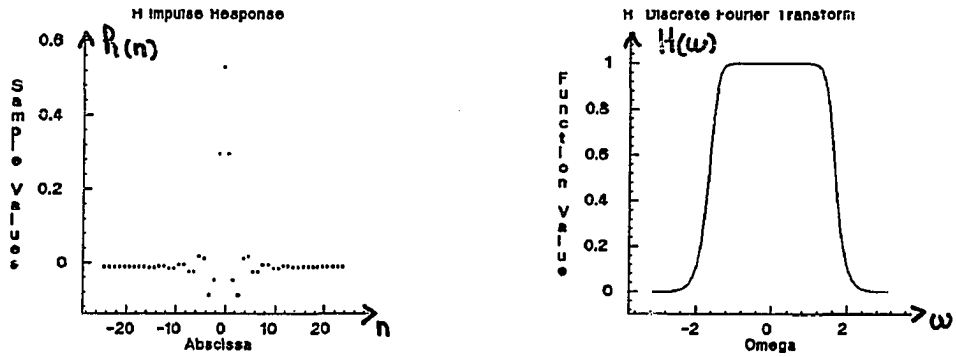


Fig. 1.3. Impulse response and Discrete Fourier Transform of the filter H . This is a low pass filter and the impulse response decreases exponentially.

1.3. The wavelet representation

1.3.1. Detail signal modeling

In this paragraph we show how to extract the difference of information between the approximation of a function $f(x)$ at the resolutions 2^{j+1} and 2^j . This difference of information is called the **detail signal** at the resolution 2^j . The approximations of signal at the resolution 2^{j+1} and 2^j are given respectively by the orthogonal projection of the signal on V_{j+1} and V_j . By applying the projection theorem we can easily show that the detail signal at the resolution 2^j is given by the orthogonal projection of the original signal on the orthogonal complement of V_j in V_{j+1} . Let O_j be this orthogonal complement :

$$O_j \text{ is orthogonal to } V_j \quad (1.20)$$

$$O_j \oplus V_j = V_{j+1} . \quad (1.21)$$

To compute the orthogonal projection of a function $f(x)$ on \mathbf{O}_j , we need to find an orthonormal basis of \mathbf{O}_j . Similarly to theorem 1.1, theorem 1.3 shows that such a basis can be built by scaling and translating a function $\psi(x)$. orthogonal wavelet.

Theorem 1.3

Let $\left[\mathbf{V}_j \right]_{j \in \mathbb{Z}}$ be a multiresolution vector space sequence, $\phi(x)$ the scaling function and H the corresponding conjugate filter. Let $\psi(x)$ be a function whose Fourier transform is given by

$$\hat{\psi}(\omega) = G\left(\frac{\omega}{2}\right) \hat{\phi}\left(\frac{\omega}{2}\right) \quad \text{with} \quad G(\omega) = e^{-i\omega} \overline{H(\omega+\pi)}. \quad (1.22)$$

Let $\psi^j(x) = 2^j \psi(2^j x)$ denote the scaling of $\psi(x)$ by 2^j .

$\left[\sqrt{2^{-j}} \psi^j(x - 2^{-j}n) \right]_{n \in \mathbb{Z}}$ is an orthonormal basis of \mathbf{O}_j and
 $\left[\sqrt{2^{-j}} \psi^j(x - 2^{-j}n) \right]_{(n, j) \in \mathbb{Z}^2}$ is an orthonormal basis of $L^2(\mathbb{R})$.

$\psi(x)$ is called an orthogonal wavelet.

The proof of this theorem can be found in chapter 2. An orthonormal basis of \mathbf{O}_j can thus be computed by scaling the wavelet $\psi(x)$ with a coefficient 2^j and translating it on a grid whose interval is proportional to 2^{-j} . Depending upon the scaling function $\phi(x)$, the wavelet $\psi(x)$ can have a good localization both in the spatial and Fourier domains. The first wavelets found by Y. Meyer [37] have an asymptotic decay which is faster than any polynomial and are in C^∞ . Given a function $H(\omega)$ which satisfies the conditions (a), (b) and (c) of theorem 1.1, we can compute the Fourier transform of an orthonormal wavelet with equations (1.19) and (1.22). I. Daubechies has shown that for any $n > 0$, we can find a function $H(\omega)$ such that the corresponding wavelet $\psi(x)$ has a compact support and is n times continuously differentiable. The family of wavelets described in appendix A are exponentially decreasing and are in C^n for different values of n . These particular wavelets have been found by P. Lemarie [25] and G. Battle [2].

The decomposition of a signal in an orthonormal wavelet basis gives an intermediate representation between Fourier and spatial representations. The properties of the wavelet orthonormal bases are discussed by P. Lemarie and Y. Meyer [26]. Due to this double localization in the Fourier and the spatial domains, it is possible to locally characterize the regularity of a function $f(x)$, with the expansion coefficients in a wavelet orthonormal basis. For example, from the asymptotically decreasing rate of the wavelet coefficients, we can determine whether a function $f(x)$ is n times differentiable at a point x_0 . Fig. 1.4 shows the wavelet associated with the scaling function of Fig. 1.1. This wavelet is symmetrical with respect to $\frac{1}{2}$.

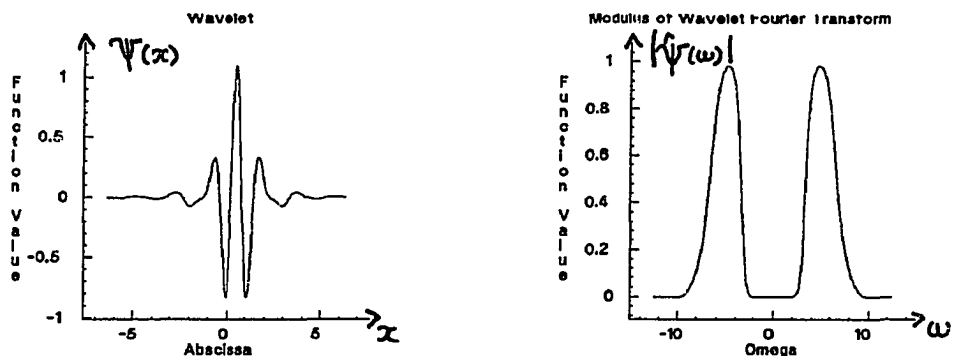


Fig. 1.4. Example of a wavelet with the modulus of its Fourier transform. The wavelet decreases exponentially in the spatial domain and as $\frac{1}{\omega^4}$ in the frequency domain.

Let P_{O_j} be the orthogonal projection on the vector space O_j . As a consequence of theorem 1.3, this operator can now be written

$$P_{O_j}(f)(x) = 2^{-j} \sum_{n=-\infty}^{+\infty} \langle f(u), \psi^j(u-2^{-j}n) \rangle \psi^j(x-2^{-j}n). \quad (1.23)$$

$P_{O_j}(f)$ is equal to the detail signal of $f(x)$ at the resolution 2^{j+1} . It is characterized by the set of inner products:

$$D_j = \left[\langle f(u), \psi^j(u-2^{-j}n) \rangle \right]_{n \in \mathbb{Z}}. \quad (1.24)$$

D_j is called the discrete detail signal at the resolution 2^j . It contains the difference of information between $A^{j+1}f_d$ and A^jf_d . Similarly to (1.12), we can prove that each of these inner products is equal to the convolution of $f(x)$ with $\psi^j(-x) = \tilde{\psi}^j(x)$ in $2^{-j}n$:

$$\langle f(u), \psi^j(u - 2^{-j}n) \rangle = (f(u) * \tilde{\psi}^j(u))(2^{-j}n). \quad (1.25)$$

Let W^j denote the operator which convolves any function $f(x) \in L^2(\mathbb{R})$ with $\tilde{\psi}^j(u)$:

$$\forall f(x) \in L^2(\mathbb{R}), \quad W^j f(x) = f * \tilde{\psi}^j(x). \quad (1.26)$$

Equations (1.24) and (1.25) show that the discrete detail signal at the resolution 2^j is equal to a uniform sampling of $W^j f(x)$ at the rate 2^j :

$$D_j = \left[W^j(2^{-j}n) \right]_{n \in \mathbb{Z}}.$$

The wavelet $\psi(x)$ can also be viewed as a band pass filter. Equations (1.26) and (1.27) show that the detail signal at each resolution corresponds to a particular frequency band of the signal. The operator W^j is further studied in chapter 3.

We can now prove by induction that for any $J < 0$, the original discrete signal $A^0 f_d$ can be represented by the set of discrete signals

$$\left[A^J f_d, (D_j)_{J \leq j \leq -1} \right]. \quad (1.28)$$

This set of discrete signals is called an **orthogonal wavelet representation**. It gives a reference signal at a coarse resolution $A^J f_d$ and the detail signals at the resolutions 2^j for $J \leq j \leq -1$. It can be interpreted as a decomposition of the original signal in an orthonormal wavelet basis or as a decomposition of the signal in a set of *independent* frequency channels like in Marr's human vision model [33]. The independence is due to the orthogonality of the wavelet functions. It is very difficult to have a real understanding of the model in terms of frequency decomposition because the frequency channels overlap and there is some aliasing. We can control this aliasing thanks to the orthogonality of our decomposition functions. That is why the tools of functional analysis give a better understanding of this decomposition. If we neglect this aliasing problem the interpretation in the frequency domain provides an intuitive approach to the model.

1.3.2. Implementation of an orthogonal wavelet representation

In this paragraph we describe a pyramidal algorithm to compute the wavelet representation. With the same derivation steps as in paragraph 1.2.2, we show that D_j can be calculated by convolving $A^{j+1}f_d$ with a discrete filter G that we characterize.

For any $n \in \mathbb{Z}$, the function $\psi^j(x - 2^{-j}n)$ is a member of $\mathbf{O}_j \subset \mathbf{V}_{j+1}$. Similarly to (1.13), we can expand this function in an orthonormal basis of \mathbf{V}_{j+1} :

$$\psi^j(x - 2^{-j}n) = 2^{-j-1} \sum_{k=-\infty}^{+\infty} \langle \psi^j(u - 2^{-j}n), \phi^{j+1}(u - 2^{-j-1}k) \rangle \phi^{j+1}(x - 2^{-j-1}k). \quad (1.29)$$

As in equation (1.14), by changing variables in the inner product integral we can prove that :

$$2^{-j-1} \langle \psi^j(u - 2^{-j}n), \phi^{j+1}(u - 2^{-j-1}k) \rangle = \frac{1}{2} \langle \psi^{-1}(u), \phi(u - (k - 2n)) \rangle. \quad (1.30)$$

Hence, by computing the inner product of $f(x)$ with the functions of both sides of equation (1.29) we get :

$$\langle f(u), \psi^j(u - 2^{-j}n) \rangle = \frac{1}{2} \sum_{k=-\infty}^{+\infty} \langle \psi^{-1}(u), \phi(u - (k - 2n)) \rangle \langle f(u), \phi^{j+1}(u - 2^{-j-1}k) \rangle.$$

Let G be the discrete filter with impulse response

$$g(n) = \frac{1}{2} \langle \psi^{-1}(u), \phi(u - n) \rangle. \quad (1.31)$$

and \tilde{G} be the mirror filter with impulse response $\tilde{g}(n) = g(-n)$. Then

$$\langle f(u), \psi^j(u - 2^{-j}n) \rangle = \sum_{k=-\infty}^{+\infty} \tilde{g}(2n - k) \langle f(u), \phi^{j+1}(u - 2^{-j-1}k) \rangle. \quad (1.32)$$

Equation (1.32) shows that we can compute the detail signal D_j by convolving $A^{j+1}f_d$ with the filter \tilde{G} and keeping every other sample of the output. Equations (1.24) and (1.32) show that we can compute an orthogonal wavelet representation of a discrete signal A^0f_d by successively decomposing $A^{j+1}f_d$ into $A^j f_d$ and D_j for $-1 \geq j \geq j$. This algorithm is illustrated by the block diagram shown in Fig. 1.5. In practice, the signal A^0f_d has only a finite number of samples. The border problems are solved as in paragraph 1.5.2 by using a symmetry with respect to first and the last sample.

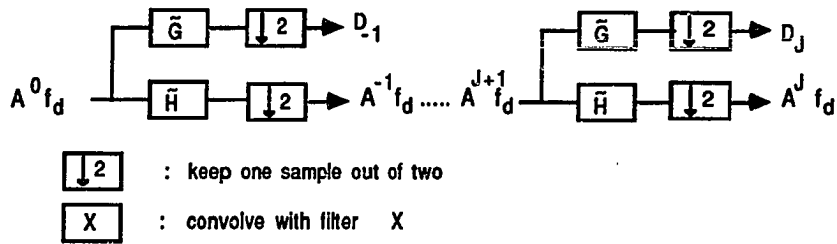


Fig. 1.5. Pyramidal algorithm for computing the wavelet representation of a one-dimensional signal.

If we insert equations (1.30) and (1.31) in (1.29), for $j = -1$ and $n = 0$ we have

$$\frac{1}{2} \Psi\left(\frac{x}{2}\right) = \sum_{k=-\infty}^{+\infty} g(k) \phi(x-k) . \quad (1.33)$$

The Fourier transform of this equation shows that the function $G(\omega)$ defined in equation (1.22) of theorem 1.3 is the Fourier series of the discrete filter $G = [g(n)]_{n \in \mathbb{Z}}$. Since $G(\omega) = e^{-i\omega} \overline{H(\omega+\pi)}$, the impulse response of G is related to the impulse respond of H by

$$g(n) = (-1)^{1-n} h(1-n) . \quad (1.34)$$

G is the mirror filter of H . It is a high-pass filter. Fig. 1.6 shows the mirror filter G of the filter H given in Fig. 1.3. In signal processing G and H are called **conjugate mirror filters**. Equation (1.32) can be interpreted as a high-pass filtering of the discrete signal $A^j f_d$. If the original signal has N samples, the discrete signals D_j and $A^j f_d$ have $2^j \cdot N$ samples each. The wavelet representation

$$\left[A^J f_d , (D_j)_{j \leq j \leq -1} \right]$$

has the same total number of samples as the original approximated signal $A^0 f_d$. The number of samples representing the signal is the same because the representation is orthogonal.

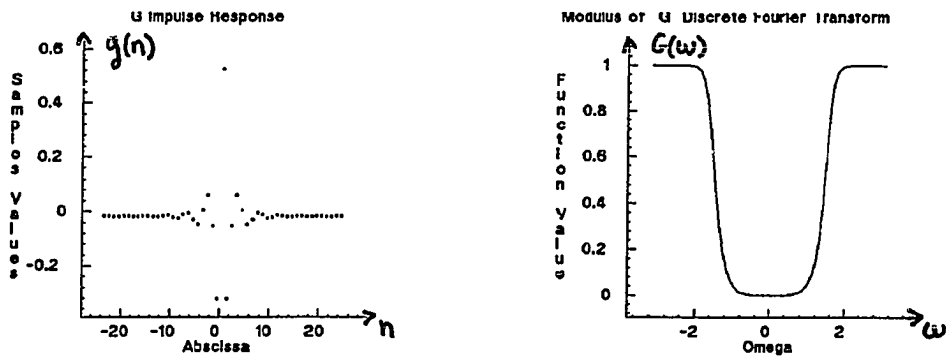


Fig. 1.6. Impulse response and Discrete Fourier Transform of the filter G . This is a high pass filter and the impulse response decreases exponentially.

Fig. 1.7 shows the detail signals at the resolutions $\frac{1}{2}, \frac{1}{4}, \frac{1}{8}$ corresponding to the original signal $A^0 f_d$ shown at the top of Fig. 1.2. The middle and the left graphs of Fig. 1.7 are respectively the discrete and continuous detail signals D_j and $P_{O_j}(f)$. The continuous detail signals $P_{O_j}(f)$ can easily be calculated from D_j with equation (1.16). The energy of the samples of D_j gives a measure of the irregularity of the signal at resolution 2^j . On the left column of Fig. 1.7 is a linear interpolation of the absolute value of the detail signal samples. Whenever $A^j f(x)$ and $A^{j+1} f(x)$ are significantly different, the signal detail has a high amplitude. In particular, this is verified near the "edges" of the signal. Depending on how straight the edge is, the highest peak is found at the resolution $\frac{1}{2}, \frac{1}{4}$ or $\frac{1}{8}$. The highest peaks at the resolution $\frac{1}{2}$ are due to the "texture" between the abscissa 60 and 80.

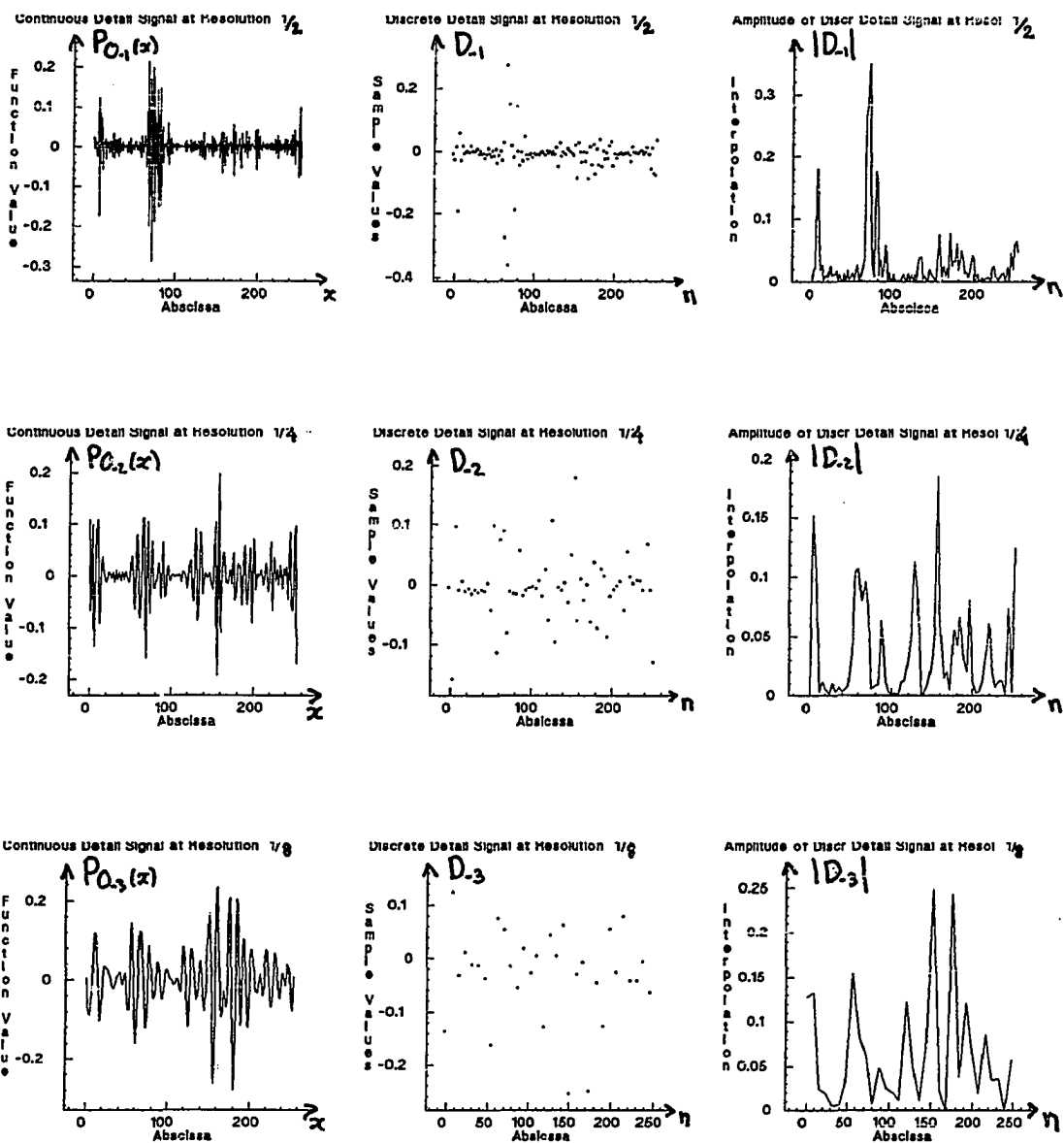


Fig. 1.7. These graphs show the detail signals at the resolutions $\frac{1}{2}, \frac{1}{4}, \frac{1}{8}$ ($j = -1, -2, -3$).

The left and middle columns are, respectively, the graphs of the continuous and discrete detail signals : $P_{O,j}(f)$ and D_j . The graphs on the right are a linear interpolation of the absolute value of the samples of D_j .

1.3.3. Signal reconstruction from an orthogonal wavelet representation

We know that the wavelet representation is complete. In this paragraph, we show that the original discrete signal can be reconstructed also with a pyramid transform. Assertions (1.12) and (1.14) show that $\left[\sqrt{2^{-j}} \phi^j(x - 2^{-j}n), \sqrt{2^{-j}} \psi^j(x - 2^{-j}n) \right]_{n \in \mathbb{Z}}$ is an orthonormal basis of \mathbf{V}_{j+1} . For any $n > 0$, the function $\phi^{j+1}(x - 2^{-j-1}n)$ can thus be decomposed in this basis :

$$\begin{aligned} \phi^{j+1}(x - 2^{-j-1}n) = & 2^{-j} \sum_{k=-\infty}^{+\infty} \langle \phi^j(u - 2^{-j}k), \phi^{j+1}(u - 2^{-j-1}n) \rangle \phi^j(x - 2^{-j}k) + \\ & 2^{-j} \sum_{k=-\infty}^{+\infty} \langle \psi^j(u - 2^{-j}k), \phi^{j+1}(u - 2^{-j-1}n) \rangle \psi^j(x - 2^{-j}k) . \end{aligned} \quad (1.35)$$

By computing the inner product of each side of equation (1.33) with the function $f(x)$, we have

$$\begin{aligned} \langle f(u), \phi^{j+1}(u - 2^{-j-1}n) \rangle = & 2^j \sum_{k=-\infty}^{+\infty} \langle \phi^j(u - 2^{-j}k), \phi^{j+1}(u - 2^{-j-1}n) \rangle \langle f(u), \phi^j(u - 2^{-j}k) \rangle + \\ & 2^{-j} \sum_{k=-\infty}^{+\infty} \langle \psi^j(u - 2^{-j}k), \phi^{j+1}(u - 2^{-j-1}n) \rangle \langle f(u), \psi^j(u - 2^{-j}k) \rangle . \end{aligned} \quad (1.36)$$

This expression can be rewritten by using the filters H and G respectively defined by equations (1.16) and (1.31)

$$\begin{aligned} \langle f, \phi^{j+1}(u - 2^{-j-1}n) \rangle = & 2 \sum_{k=-\infty}^{+\infty} h(n-2k) \langle f(u), \phi^j(u - 2^{-j}k) \rangle + \\ & 2 \sum_{k=-\infty}^{+\infty} g(n-2k) \langle f(u), \psi^j(u - 2^{-j}k) \rangle . \end{aligned}$$

This equation shows that $A^{j+1}f_d$ can be reconstructed by putting zeros between each sample of $A^j f_d$ and D_j and convolving the resulting signals with the filters H and G respectively. The original discrete signal $A^0 f_d$ can thus be reconstructed by repeating this procedure for $J \leq j < 0$, as illustrated by the block diagram in Fig. 1.8. Fig. 1.9 is a reconstruction of the discrete signal $A^0 f_d$ shown at the top of Fig. 1.2, from its wavelet representation ($J = -3$). By comparing the two graphs, we can appreciate the quality of the reconstruction. The low and high frequencies of the signal are reconstructed well, which illustrates the numerical stability of the decomposition and reconstruction processes.

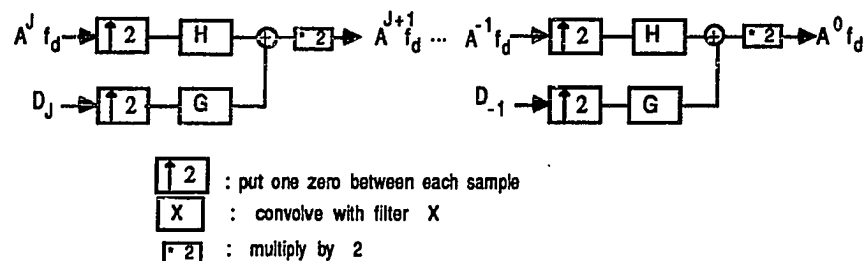


Fig. 1.8. Pyramid architecture for reconstructing a one-dimensional signal signal from its wavelet decomposition.

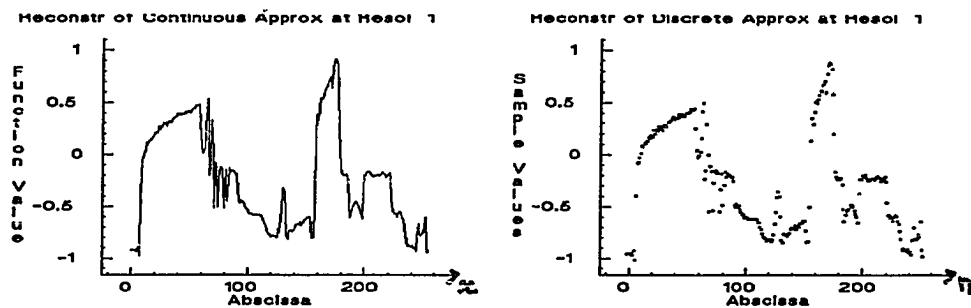


Fig. 1.9. The left graph is the discrete reconstruction of the approximated signal at the resolution 1. The right graph gives the corresponding continuous signal. The quality of the reconstruction can be appreciated by comparing these graphs with the top graphs of Fig. 1.2.

1.4. Extension of the orthogonal wavelet representation to images

The wavelet model can be easily generalized to any dimension $n \in \mathbb{N}^*$ [36]. In this paragraph we study the two-dimensional case for image processing applications. We consider that our signal is a finite energy function $f(x,y) \in L^2(\mathbb{R}^2)$. A multiresolution approximation of $L^2(\mathbb{R}^2)$ is a sequence of subspaces of $L^2(\mathbb{R}^2)$ which satisfies a straightforward two-dimensional extension of the properties (1.2) to (1.7). Let $\left[V_j \right]_{j \in \mathbb{Z}}$ be such a multiresolution approximation of $L^2(\mathbb{R}^2)$. The approximation of a signal $f(x,y)$ at a resolution 2^j is equal to its orthogonal projection on the vector space V_j . In two dimensions, theorem 1.1 is still valid and one can show that there exists a unique scaling function $\Phi(x,y)$ whose dilate and translate give an orthonormal basis of each space V_j . Let $\Phi^j(x,y) = 2^{2j} \Phi(2^j x, 2^j y)$. The family of functions

$$\left[\Phi^j(x - 2^{-j}n, y - 2^{-j}m) \right]_{(n,m) \in \mathbb{Z}^2} \text{ is an orthonormal basis of } V_j.$$

The function $\Phi(x,y)$ is unique with respect to a particular multiresolution approximation of $L^2(\mathbb{R}^2)$. In this chapter we study the particular case of separable multiresolution approximations of $L^2(\mathbb{R}^2)$. For such multiresolution approximations, each vector space V_j can be decomposed as a tensor product of two identical subspaces of $L^2(\mathbb{R})$

$$V_j = V_j^1 \otimes V_j^1.$$

It is necessary and sufficient that $\left[V_j^1 \right]_{j \in \mathbb{Z}}$ is a multiresolution approximation of $L^2(\mathbb{R})$.

One can then easily derive that the scaling function $\Phi(x,y)$ can be written

$$\Phi(x,y) = \phi(x) \phi(y), \quad (1.37)$$

where $\phi(x)$ is the one-dimensional scaling function of the multiresolution approximation $\left[V_j^1 \right]_{j \in \mathbb{Z}}$. With a separable multiresolution approximation, we give a particular importance to the horizontal and vertical directions in the image. For many types of images such as in man made environment, these directions are particularly important. In this particular case, the orthogonal basis of V_j can be written

$$\left[\Phi^j(x - 2^{-j}n, y - 2^{-j}m) \right]_{(n,m) \in \mathbb{Z}^2} = \left[\phi^j(x - 2^{-j}n) \phi^j(y - 2^{-j}m) \right]_{(n,m) \in \mathbb{Z}^2}. \quad (1.38)$$

The approximation of a signal $f(x,y)$ at a resolution 2^j is therefore characterized by the set of inner products

$$A^j f_d = \left[\langle f(x,y), \phi^j(x-2^{-j}n) \phi^j(y-2^{-j}m) \rangle \right]_{(n,m) \in \mathbb{Z}^2}. \quad (1.39)$$

Fig. 1.10 gives the discrete approximations of an image for $j = 0, -1, -2, -3$.

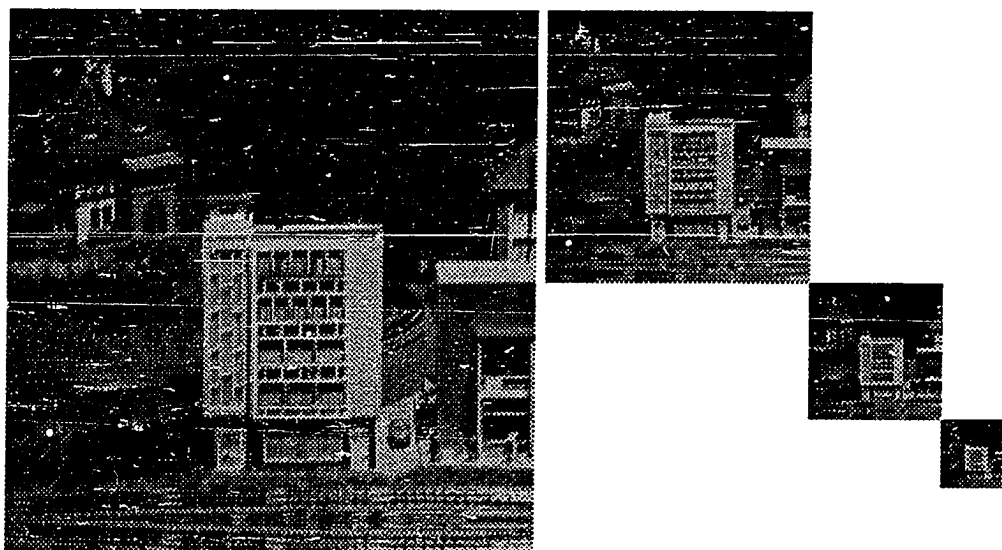


Fig. 1.10 Approximations of an image at the resolutions $1, \frac{1}{2}, \frac{1}{4}, \frac{1}{8}$ ($j = 0, -1, -2, -3$).

As in the one-dimensional case, the detail signal at the resolution 2^j is equal to the orthogonal projection of the signal on the orthogonal complement of \mathbf{V}_j in \mathbf{V}_{j+1} . Let \mathbf{O}_j be this orthogonal complement. The following theorem gives a simple extension of theorem 1.3. It shows that we can build an orthonormal basis of \mathbf{O}_j by scaling and translating three wavelets : $\Psi_1(x,y)$, $\Psi_2(x,y)$ and $\Psi_3(x,y)$.

Theorem 1.4

Let $\left[V_j \right]_{j \in \mathbb{Z}}$ be a separable multiresolution approximation of $L^2(\mathbb{R}^2)$. Let $\Phi(x,y) = \phi(x)\phi(y)$ be the associated two-dimensional scaling function. Let $\psi(x)$ be the one-dimensional wavelet associated with the scaling function $\phi(x)$. There exists three wavelets $\Psi_1(x,y) = \phi(x)\psi(y)$, $\Psi_2(x,y) = \psi(x)\phi(y)$, $\Psi_3(x,y) = \psi(x)\psi(y)$ such that

$$\left\{ \begin{array}{l} 2^{-j} \Psi_1(x-2^{-j}n, y-2^{-j}m) \\ 2^{-j} \Psi_2(x-2^{-j}n, y-2^{-j}m) \\ 2^{-j} \Psi_3(x-2^{-j}n, y-2^{-j}m) \end{array} \right\}_{(n,m) \in \mathbb{Z}^2} \quad (1.40)$$

is an orthonormal basis of \mathbf{O}_j and

$$\left\{ \begin{array}{l} 2^{-j} \Psi_1(x-2^{-j}n, y-2^{-j}m) \\ 2^{-j} \Psi_2(x-2^{-j}n, y-2^{-j}m) \\ 2^{-j} \Psi_3(x-2^{-j}n, y-2^{-j}m) \end{array} \right\}_{(n,m,j) \in \mathbb{Z}^3} \quad (1.41)$$

is an orthonormal basis of $L^2(\mathbb{R}^2)$.

Chapter 2 gives a proof of this theorem. In two dimensions, the difference of information between $A^{j+1}f_d$ and $A^j f_d$ is now given by three detail signal images:

$$\begin{aligned} D_j^1 &= \left[\langle f(x,y), \Psi_1(x-2^{-j}n, y-2^{-j}m) \rangle \right]_{(n,m) \in \mathbb{Z}^2}, \\ D_j^2 &= \left[\langle f(x,y), \Psi_2(x-2^{-j}n, y-2^{-j}m) \rangle \right]_{(n,m) \in \mathbb{Z}^2}, \\ D_j^3 &= \left[\langle f(x,y), \Psi_3(x-2^{-j}n, y-2^{-j}m) \rangle \right]_{(n,m) \in \mathbb{Z}^2}. \end{aligned}$$

As in the one-dimensional case, we suppose that the output of the image digitizer corresponds to $A^0 f_d$. For any $J < 0$, the discrete image can be thus be completely represented by the $-3J + 1$ discrete images :

$$\left[A^J f_d, (D_j^1)_{J \leq j \leq -1}, (D_j^2)_{J \leq j \leq -1}, (D_j^3)_{J \leq j \leq -1} \right].$$

This set of images is called an **orthogonal wavelet representation** in two dimensions. $A^J f_d$ is the coarse image and the D_j^k images give the detail signals for the different orientations and resolutions. If the original image has N^2 pixels, each image $A^J f_d, D_j^1, D_j^2, D_j^3$ has $2^J \cdot N^2$

pixels ($j < 0$). The total number of pixels in this new representation is equal to the number of pixels of the original image, so we do not increase the volume of data. This is due to the orthogonality of the representation.

Just as for one-dimensional signals, in two dimensions, the inner products which define $A^j f_d$, D_j^1 , D_j^2 and D_j^3 are equal to a uniform sampling two-dimensional convolution products. Since the three wavelets $\Psi_1(x,y)$, $\Psi_2(x,y)$, $\Psi_3(x,y)$ are given by separable product of the functions ϕ and ψ , these convolutions can be written

$$A^j f_d = \left[(f(x,y) * \phi^j(-x)\phi^j(-y))(2^{-j}n, 2^{-j}m) \right]_{(n,m) \in \mathbb{Z}^2} \quad (1.42)$$

$$D_j^1 = \left[(f(x,y) * \phi^j(-x)\psi^j(-y))(2^{-j}n, 2^{-j}m) \right]_{(n,m) \in \mathbb{Z}^2} \quad (1.43)$$

$$D_j^2 = \left[(f(x,y) * \psi^j(-x)\phi^j(-y))(2^{-j}n, 2^{-j}m) \right]_{(n,m) \in \mathbb{Z}^2} \quad (1.44)$$

$$D_j^3 = \left[(f(x,y) * \psi^j(-x)\psi^j(-y))(2^{-j}n, 2^{-j}m) \right]_{(n,m) \in \mathbb{Z}^2}. \quad (1.45)$$

The expressions (1.42), (1.43), (1.44) and (1.45) show that in two dimensions, $A^j f_d$ and the D_j^k are computed with separable filtering of the signal along the abscissa and ordinate. The wavelet decomposition can thus be interpreted as a signal decomposition in a set of independent, *spatially oriented* frequency channels. Let us suppose that $\phi(x)$ and $\psi(x)$ are, respectively, a perfect low-pass and a perfect band-pass filter. Fig. 1.11(a) shows in the frequency domain how the discrete signal $A^{j+1} f_d$ is decomposed into $A^j f_d$, D_j^1 , D_j^2 and D_j^3 . $A^j f_d$ corresponds to the lowest frequencies, D_j^1 gives the vertical high frequencies (horizontal edges) at the resolution 2^{j+1} , D_j^2 the horizontal high frequencies (vertical edges) and D_j^3 the high frequencies in both directions (corners). This is well illustrated by the decomposition of a white square on a black background shown in Fig. 1.12(b). All of the two-dimensional wavelet decompositions shown in this chapter have been computed with the one-dimensional filters shown in Fig. 1.3 and Fig. 1.6. The arrangement of the D_j^k images is shown in Fig. 1.11(b). The black, grey and white pixels respectively correspond to negative, zero and positive coefficients. Fig. 1.12(c) gives the absolute value of the detail signal samples. The black pixels correspond to zero whereas the white ones have the highest amplitude. As expected, the detail signal samples have a high amplitude respectively on the horizontal edges, the vertical edges and the corners of the square.

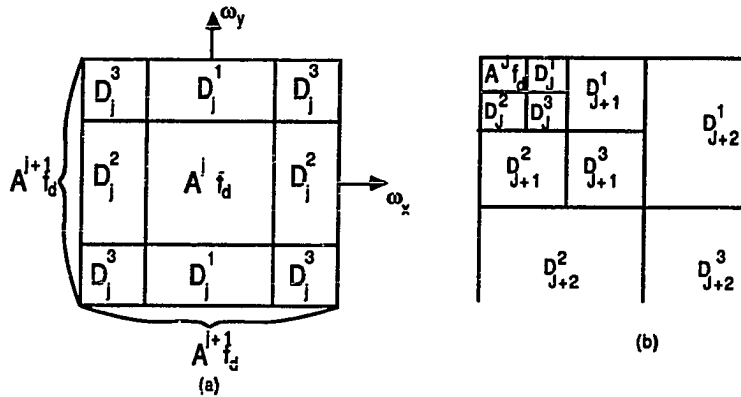


Fig. 1.11. (a) Frequency support of the images $A^{j+1}f_d$, $A^j f_d$ and the detail images D_j^k . (b) Disposition of the D_j^k and $A^j f_d$ images in the wavelet representations shown in Fig. 1.12(b) , Fig. 1.15(b) and Fig. 1.16(b).

1.4.1. Decomposition and reconstruction algorithms in two dimensions

In two dimensions, the wavelet representation can be computed with a pyramidal algorithm similar to the one-dimensional algorithm described in 3.2. Indeed, the two-dimensional wavelet transform that we have described can be seen as a one-dimensional wavelet transform along the x and y axes. By repeating the analysis described in paragraph 1.3.2, we can show that a two-dimensional wavelet transform can be computed in cascade by filtering the rows and columns of the images $A^j f_d$ with the discrete filters H and G defined by equations (1.16) and (1.31). This algorithm is illustrated by the block diagram shown in Fig. 1.13 and corresponds to a separable conjugate mirror filter decomposition [50].

Fig. 1.15(b) shows the wavelet representation of a natural scene image for $J = -3$, and Fig. 1.15(c) gives the absolute value of the detail signal samples. The arrangement of the detail images is also explained in Fig. 1.11(b). Fig. 1.16 is another example of wavelet representation for $J = -5$. The detail image samples which have a high amplitude are around the edges and in the texture areas within a given spatial orientation.

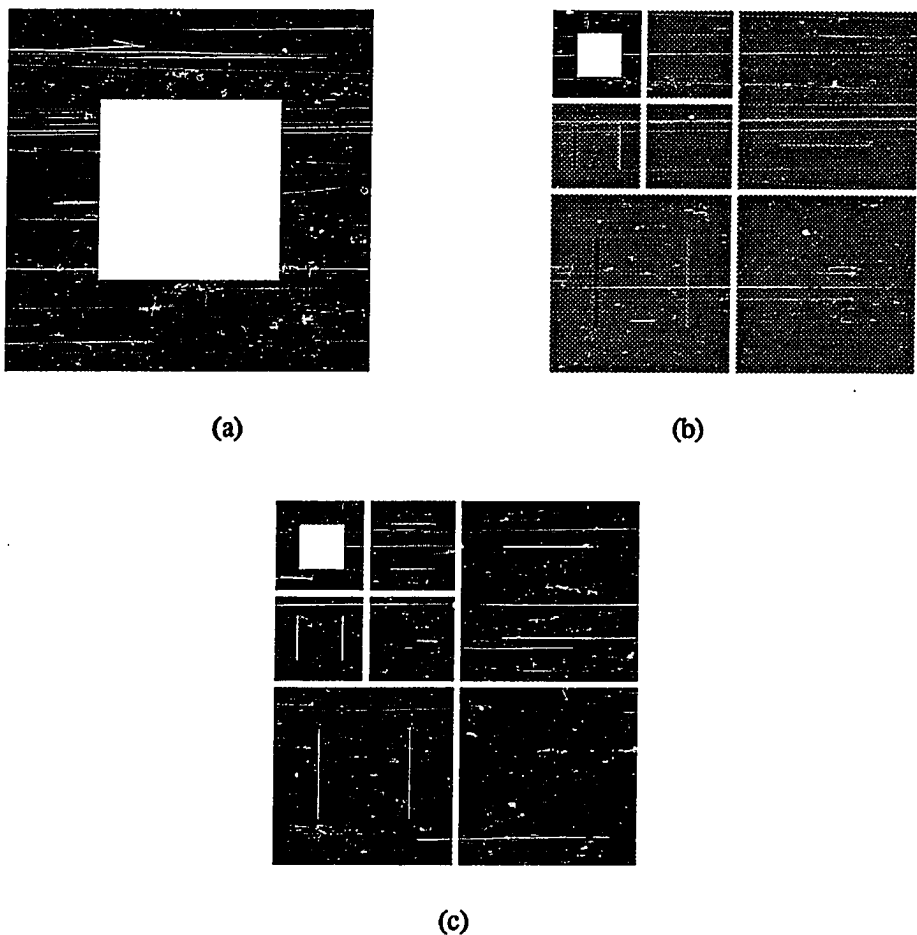


Fig. 1.12. (a) *Original image.* (b) *Wavelet representation for $J = -2$.* (c) *Absolute value of the detail signal pixels.*

The one-dimensional reconstruction algorithm described in paragraph 1.3.3 can also be easily extended to two dimensions. The original image $A^0 f_d$ can be reconstructed from a two-dimensional wavelet representation with the pyramidal algorithm illustrated in Fig. 1.14. This algorithm is a separable extension of the one-dimensional algorithm shown in Fig. 1.8. We convolve the rows and columns of the images $A^j f_d$ and D^k with the filters H and G. Fig. 1.15(d) and Fig. 1.16(d) show respectively the image reconstruction of the original image from its wavelet representation. If we keep floating-point precision on the discrete signals of the wavelet representation, the reconstruction is of very good quality, as can be seen from these images.

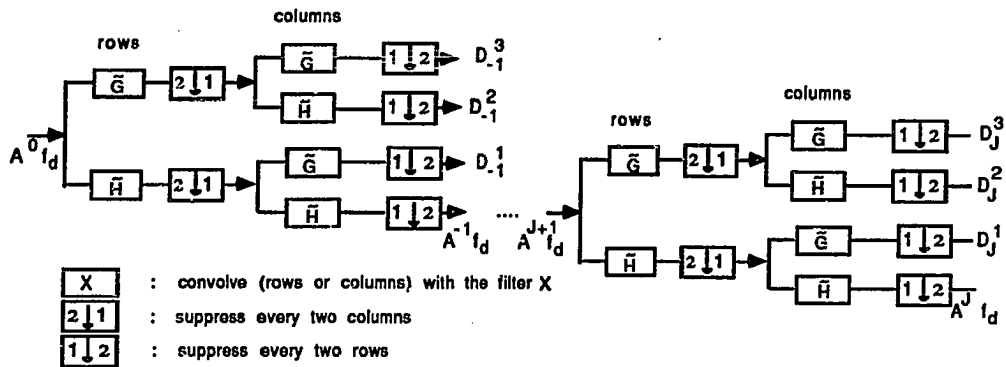


Fig. 1.13. Pyramid architecture for computing the wavelet representation of a two-dimensional signal.

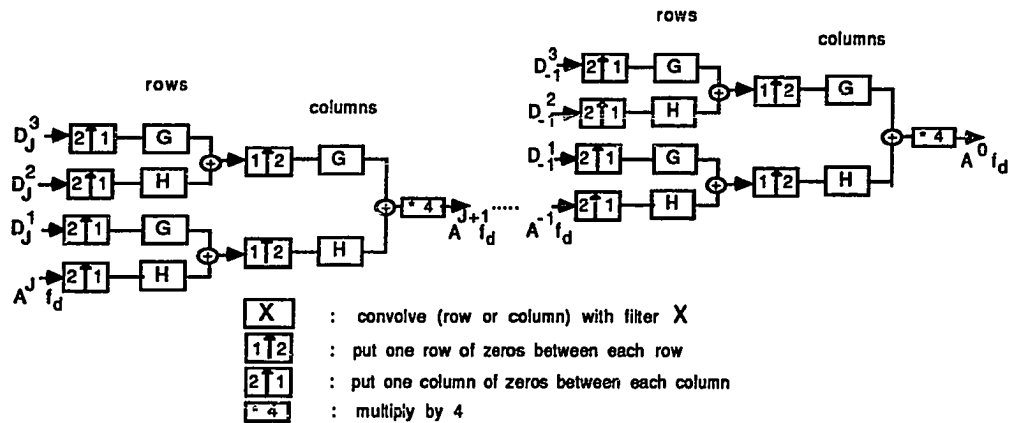


Fig. 1.14. Pyramid architecture for reconstructing an image from its wavelet decomposition.

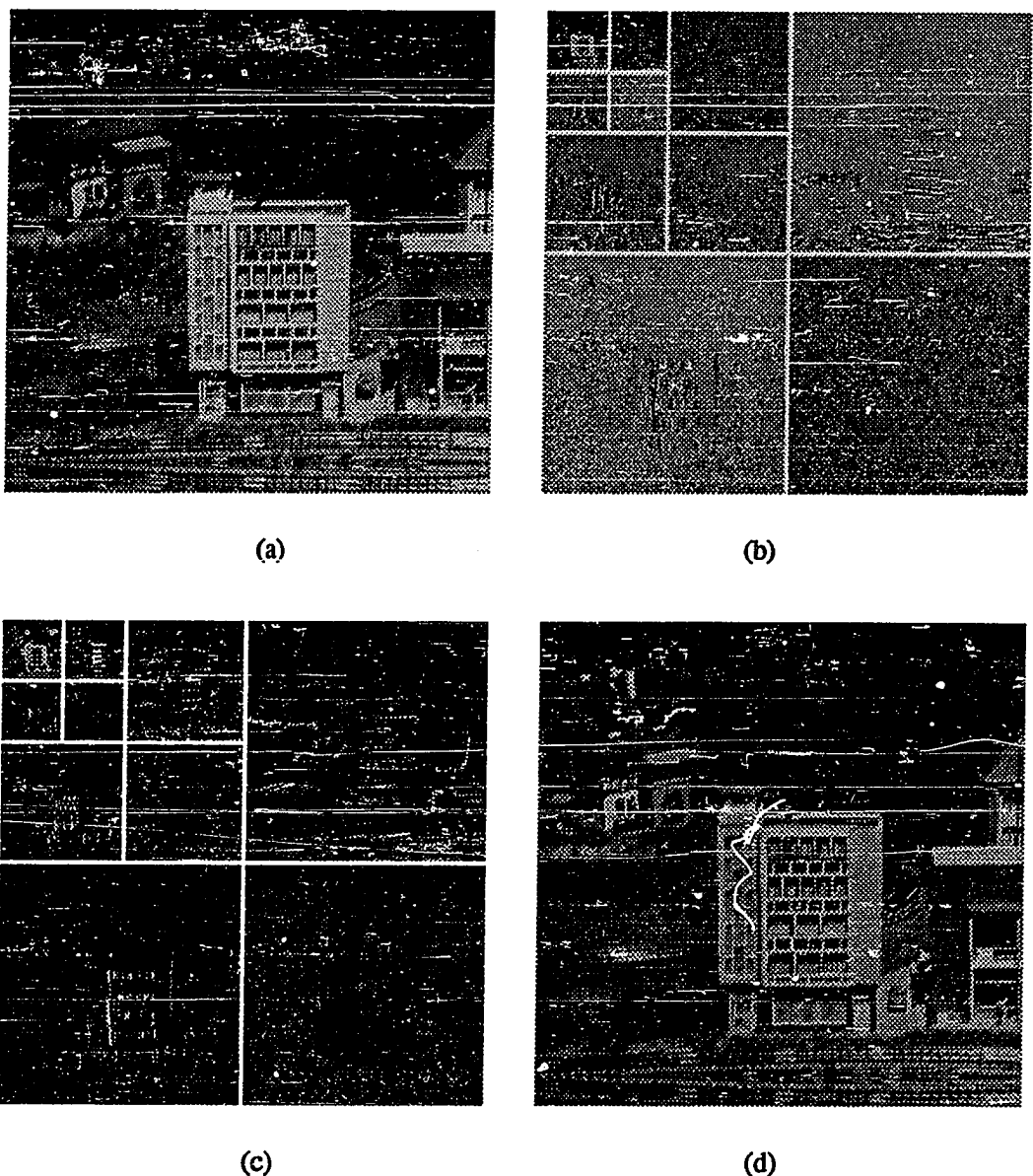
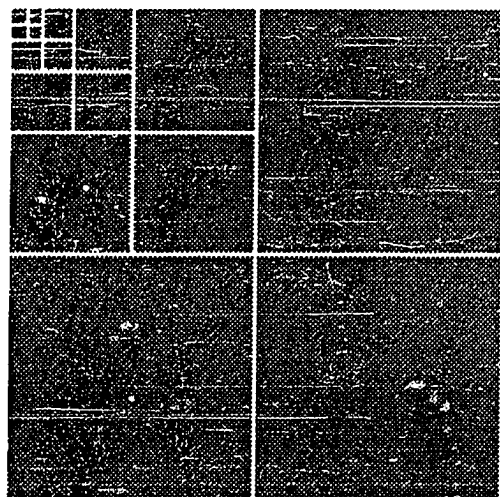


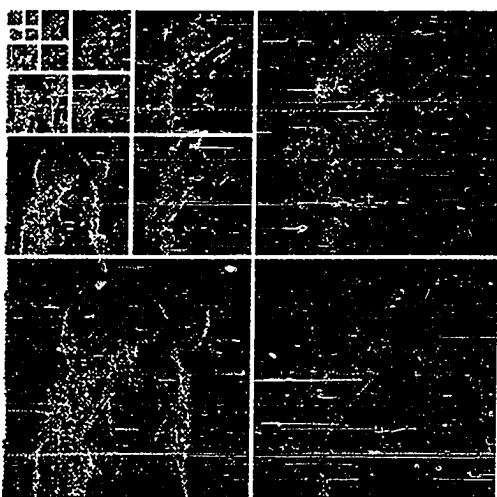
Fig. 1.15. (a) Original image. (b) Wavelet representation for $J = -3$. (c) Absolute value of the detail signal pixels. (d) Reconstructed image from a representation with floating-point precision.



(a)



(b)



(c)



(d)

Fig. 1.16. (a): Original lady image. (b): Wavelet representation for $J = -5$. (c): Absolute value of the detail images pixels. (d): Reconstructed image from a representation with floating-point precision.

1.5. Applications of the orthogonal wavelet representation

1.5.1. Quantization of the orthogonal wavelet representation

In theory, to compute an exact reconstruction of the original image, we must keep the pixel values of each detail image with an infinite precision. However, for practical applications, we can admit some errors as long as the relevant information is not destroyed. Such imprecisions exist in the human visual system. The human visual system is not able to differentiate a difference of contrast which is smaller than a certain threshold ΔC . ΔC depends on the intensity, the orientation and the frequency of the stimuli. A. Watson [48] has shown that this threshold ΔC could be modeled from the quantization of a representation similar to the wavelet representation which might be implemented in the human visual cortex. The conjugate mirror filters which implement the wavelet decomposition have been studied by J. Woods [50] and E. Adelson et al. [1] for image coding. In order to be able to use the wavelet representation in computer vision, we must not modify the structure of the representation with some coding algorithm. Hence, in this paragraph, we study only an optimal quantization of this representation without any further coding. Our goal is to find a quantization procedure which minimizes the quantization noise on the reconstructed image. P. Burt and E. Adelson [5] have shown that one can reduce considerably the amount of data representing the image with a uniform quantization of the Laplacian pyramid. Since the wavelet multiresolution representation is orthogonal, a priori we should be able to get even better data compression.

Let us first study how the quantization noise of the wavelet representation relates to the error on the reconstructed signal. Let $[A^J f_d, (D_j)_{J \leq j \leq -1}]$ be a one-dimensional wavelet representation. We denote the quantized representation $[A^J f_d^q, (D_j^q)_{J \leq j \leq -1}]$ by adding a superscript q . This quantized representation is defined by the number of quantization levels $[N'_J, (N_j)_{J \leq j \leq -1}]$ for each signal, plus the respective positions of the quantization levels and quantization bins. Let $[\epsilon'_J, (\epsilon_j)_{J \leq j \leq -1}]$ be respectively the energies of the quantization noise. Since the wavelet representation is orthogonal with respect to an $L^2(\mathbb{R})$ norm, one can easily show that the quantization energy of the signal $A^0 f_d^q$ reconstructed from the quantized representation is :

$$\epsilon'_0 = \epsilon'_J + \sum_{j=1}^{J-1} \epsilon_j . \quad (1.46)$$

In two dimensions this result can be easily extended. Let $\epsilon_j^1, \epsilon_j^2, \epsilon_j^3$ be respectively the quantization energy of the detail images $D_j^{1,q}, D_j^{2,q}, D_j^{3,q}$. The error on the reconstructed image is then given by

$$\epsilon'_0 = \epsilon'_J + \sum_{k=1}^3 \sum_{j=1}^{J-1} \epsilon_j^k \quad (1.47)$$

In order to quantize this representation, we must define an a priori distribution of the quantization noise between each detail signal of the representation. Since we do not want to emphasize any particular resolution level nor orientation, we introduce the same amount of quantization noise in each detail image : $\epsilon_j^k = \epsilon'_j = \epsilon$ for $J \leq j \leq -1$ and $1 \leq k \leq 3$.

For a signal whose histogram is equal to $h(u)$, the quantization noise ϵ is given by

$$\epsilon = \sum_{i=1}^N \int_{x_i}^{x_{i+1}} h(u) (u - y_i)^2 du . \quad (1.48)$$

$N, (y_i)_{1 \leq i \leq N}$ and $(x_i)_{1 \leq i \leq N}$ are respectively the number of quantization levels, the positions of the quantization levels and the positions of the quantization bins. To have a maximum data compression for a given quantization noise, we must find the values of the x_i and y_i which minimize N for a given ϵ . This optimization depends upon the signal histogram $h(u)$. In the following we study a model of the image detail histograms.

In general we do not have any a priori knowledge on the grey level distribution of an image intensity. This is also true for $A^J f_d$, which gives the image approximation at the resolution 2^J . We thus uniformly quantize $A^J f_d$ in order to have a quantization noise independent of the shape of the histogram. It is well-known that when a signal is quantized uniformly, the size of the quantization bins Δx is related to the quantization noise ϵ'_J by

$$\Delta x = \sqrt{12 \epsilon'_J} .$$

This relation enables us to compute the size Δx of the quantization bins for $A^J f_d$.

If images were any kind of two-dimensional signals in $L^2(\mathbb{R}^2)$, the histogram of the detail images could have any shape. Indeed, these detail images correspond to a decomposition of the image in an orthonormal family of functions. In reality these histograms are symmetric

peaks centered at zero. This shows that images are some very particular kind of $L^2(\mathbb{R}^2)$ signals. This is a well known observation in image processing [28]. There is however no clear model which defines the sub-set of $L^2(\mathbb{R}^2)$ corresponding to images. The wavelet orthonormal bases might be helpful for defining this sub-set. Indeed, it is much easier to work with an orthonormal family of functions when analyzing the statistical properties of a signal from its decomposition. In the case of a wavelet representation, we have found experimentally that the detail image histograms could be modeled with the following family of histograms:

$$h(u) = K e^{-\left(\frac{|u|}{\alpha}\right)^{\beta}}. \quad (1.49)$$

β enables us to modify the decreasing rate of the peak and α its variance. K is a constant which is adjusted in order to have $\int_{-\infty}^{\infty} h(u) du = M$, where M is the total number of pixels of the given detail image. A simple computation gives

$$K = \frac{M \beta}{2 \alpha \Gamma(\frac{1}{\beta})} \quad \text{where} \quad \Gamma(t) = \int_0^{\infty} e^{-u} u^{t-1} du. \quad (1.50)$$

This model was built by studying the histograms of 3 images decomposed 5 resolution levels. The goal of this study was to define a qualitative model of these histograms for the optimal quantization procedure. The coefficients α and β of the histogram model can be computed by measuring the first two moments of the real histogram that we want to model. Indeed, with a simple computation, one can show that

$$m_1 = \int_{-\infty}^{\infty} |u| h(u) du = 2K \frac{\alpha^2}{\beta} \Gamma(\frac{2}{\beta}) \quad \text{and} \quad m_2 = \int_{-\infty}^{\infty} u^2 h(u) du = 2K \frac{\alpha^3}{\beta} \Gamma(\frac{3}{\beta}),$$

$$\text{so } \beta = F^{-1}\left(\frac{m_1^2}{m_2 M}\right) \quad \text{where} \quad F(x) = \frac{\Gamma(\frac{2}{x})^2}{\Gamma(\frac{3}{x}) \Gamma(\frac{1}{x})} \quad (1.51)$$

$$\text{and} \quad \alpha = \frac{m_2 \Gamma(\frac{1}{\beta})}{M \Gamma(\frac{3}{\beta})}. \quad (1.52)$$

The curve $F^{-1}(x)$ is shown in Fig. 1.18. As an example, Fig. 1.17 shows the histogram of D_3^3 of the lady image and the corresponding model.

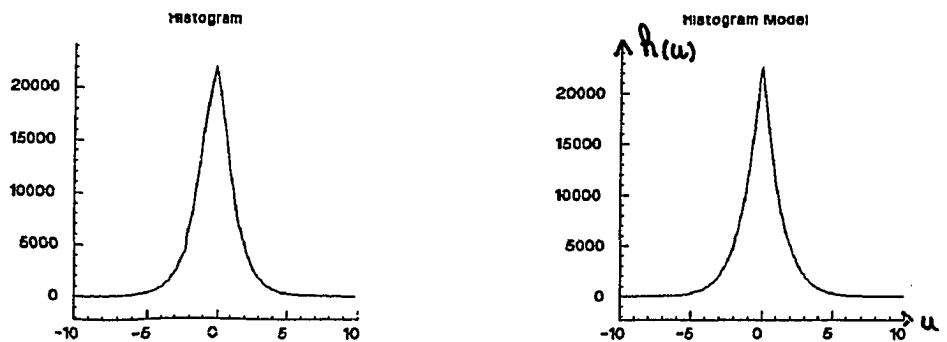


Fig. 1.17. Left: Graph of the histogram $h(u)$. Right: Modeling of $h(u)$ with $\alpha = 1.39$ and $\beta = 1.14$.

For a given histogram and a number of quantization levels N , we can use the algorithm of Max [35] to compute the optimal quantization which minimizes the quantization noise ϵ in (1.48). The parameter α of $h(u)$ only modifies the scale along the u axis. If β is fixed, the minimum quantization noise is proportional to α^2 , and the values $(y_i)_{1 \leq i \leq N}$ and $(x_i)_{1 \leq i \leq N}$ are proportional to α . For the wavelet representations of the images that we studied, we found that $\beta \in [0.4, 1.5]$. Fig. 1.18 gives the quantization noise depending on the number of quantization levels N for $\beta \in \{1.5, 1, 0.7, 0.5, 0.4\}$ and for a normalized histogram ($M = 1, m_2 = 1$).

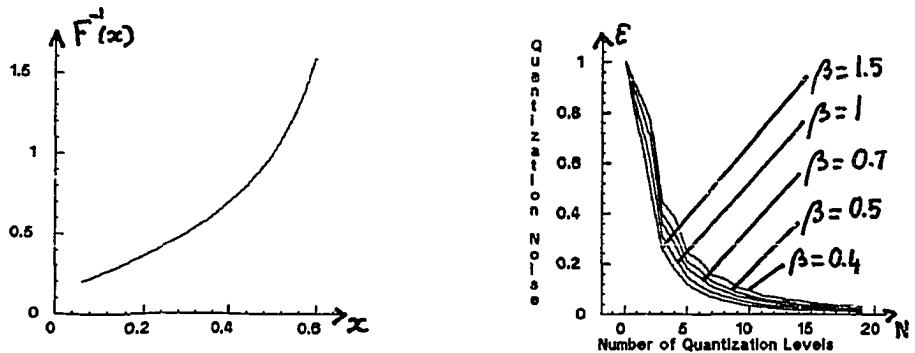


Fig. 1.18. Left: Graph of $F^{-1}(x)$. Right: Quantization noise as a function of the number of quantization levels for different values of β .

As explained in the previous paragraph, we want to adapt the quantization in order to produce a constant quantization noise in all the signal details. The right curves of Fig. 1.18 enable us to compute the corresponding minimum number of quantization level depending on the value of β in each detail signal. We can then extract from a file the optimal position of the quantization bins and of the quantization levels. These positions must have been previously computed with the Max algorithm.

Fig. 1.19 gives the values of the parameters α and β for the histograms of each discrete image of the wavelet representation shown in Fig 1.16. The array of Fig. 1.20 gives the minimum number of quantization levels required for each image of the wavelet representation in order to have a quantization noise smaller than ϵ . We can observe that for the lower frequencies (coarse resolution) we need more quantization levels than for the highest frequencies. Hence, the sensitivity of the quantized representation is higher at low frequencies. This is true for all images because the energy is generally concentrated in the lower frequencies. It is interesting to remark that the human visual system is also much more sensitive to contrast at low frequencies. The evolution of the contrast sensitivity with respect to the frequency of the stimuli is qualitatively the same for a human observer and for our quantized wavelet representation [48].

Fig. 1.21 shows the reconstructed images from these quantized wavelet representations. M is the mean number of quantization-levels per pixel. Normally the image intensity is quantized on 256 levels so $M = 256$. Fig. 1.21 gives the reconstructed images from the quantized representation for $\epsilon = 0.8, 1.4, 3.2, 5.8$. The quality of the reconstructed images can be appreciated by comparing with the original image shown in Fig. 1.16(a). For $\epsilon = 0.8$ there is almost no perceptual degradation of the original image on a TV monitor.

	D_{-5}^1	D_{-5}^2	D_{-5}^3	D_{-4}^1	D_{-4}^2	D_{-4}^3	D_{-3}^1	D_{-3}^2	D_{-3}^3	D_{-2}^1	D_{-2}^2	D_{-2}^3	D_{-1}^1	D_{-1}^2	D_{-1}^3
α	2.71	17.7	3.17	1.22	5.20	1.06	0.43	1.63	0.43	0.34	0.43	0.32	1.35	0.83	1.39
β	0.74	1.24	0.72	0.61	0.78	0.58	0.50	0.59	0.50	0.52	0.47	0.53	0.94	0.64	1.14

Fig. 1.19. This array gives the value of the parameters α and β for the histograms of each the detail image of the wavelet representation shown in Fig. 1.16.

$\epsilon \backslash$	S_{-5}	D_{-5}^1	D_{-5}^2	D_5^3	D_{-4}^1	D_{-4}^2	D_{-4}^3	D_{-3}^1	D_{-3}^2	D_{-3}^3	D_{-2}^1	D_{-2}^2	D_{-2}^3	D_{-1}^1	D_{-1}^2	D_{-1}^3	M
5.8	25	7	16	8	5	12	6	4	8	4	3	6	2	1	3	1	2.33
3.2	34	8	21	12	7	16	8	6	13	6	4	8	3	1	4	2	3.27
1.4	51	14	32	19	11	24	14	8	20	8	7	13	5	3	6	2	5.18
0.8	68	19	42	24	15	32	18	13	27	13	8	18	8	4	8	3	7.10

Fig. 1.20. For different values of the quantization noise ϵ , this array gives the minimum number of quantization levels for each image of the wavelet representation shown in Fig. 1.16.



(a)



(b)



(c)



(d)

Fig. 1.21. These images show the reconstructed images from the quantized wavelet representation for different values of the quantization noise ϵ . (a): $\epsilon = 0.8$. (b): $\epsilon = 1.4$. (c): $\epsilon = 3.2$. (d): $\epsilon = 5.8$.

1.5.2. Texture discrimination and fractal

In this paragraph, we describe the application of the wavelet orthogonal representation to texture discrimination and fractal analysis. In psychophysics B. Julesz [22] has shown that humans analyze textures by decomposing them with a set of basic functions called *textons*. These textons are spatially *local*; they have a particular *spatial orientation* and a narrow *frequency tuning*. The wavelet representation can also be interpreted as a texton decomposition where each texton is equal to one function of the wavelet orthonormal basis. Indeed, these functions have all the discriminative abilities required by the Julesz theory. In the decomposition studied in this chapter we only have three orientation tunings, but we could build a wavelet representation having as many orientation tunings as desired by using non-separable wavelet orthonormal bases [36]. Fig. 1.22(a) shows three textures synthesized by J. Beck. Human cannot preattentively discriminate the middle from the right texture but can separate the left texture from the others. In this example, the human discrimination is based mainly on the orientation of these textures as their frequency content is very similar. With a firstorder statistical analysis of the wavelet representation shown in Fig. 1.22(b), we can also discriminate the left texture but not the two others. This example illustrates the ability of our representation to differentiate textures on orientation criteria. This is of course only one aspect of the problem, and a more sophisticated statistical analysis is needed for modeling textures [13]. Although several psycho-physical studies have shown the importance of a signal decomposition in several frequency channels [14, 3], there still is no statistical model to combine the information provided by the different channels. From this point of view, the wavelet mathematical model might be helpful to transpose some tools currently used in functional analysis to characterize the local regularity of functions.

B. Mandelbrot [32] has shown that some natural texture images can be modeled by Brownian fractal noise. A Brownian fractal noise $F(x)$ is a random process whose increment has a probability distribution given by:

$$Pr\left[\frac{|F(x) - F(x+\Delta x)|}{\|\Delta x\|^H} = u \right] = g(u) .$$

$g(u)$ is a Gaussian probability distribution. Such a random process is selfsimilar :

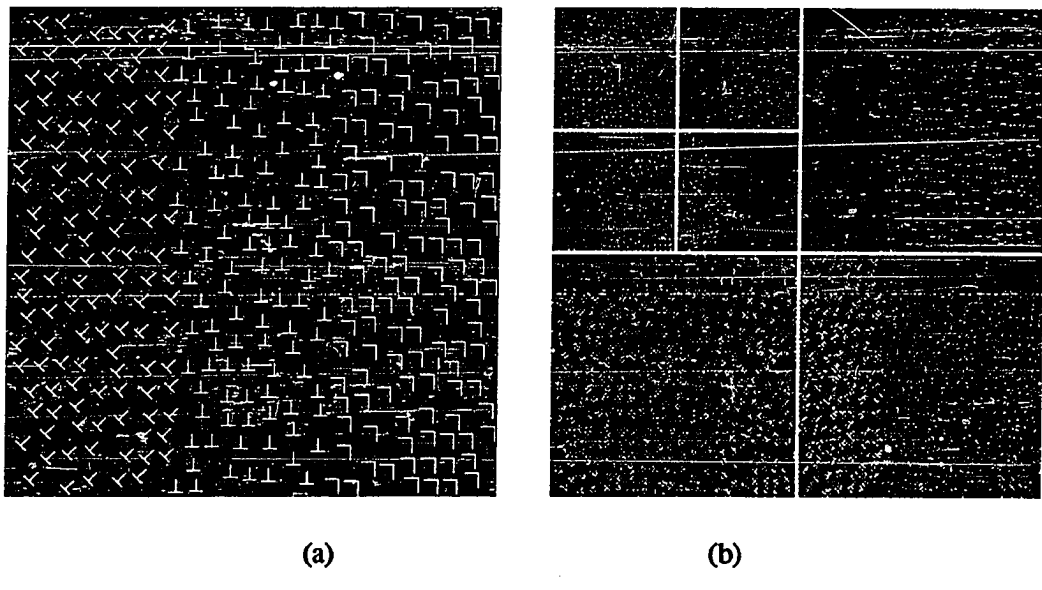


Fig. 1.22. (a) J.Beck textures : only the left texture is preattentively discriminable. (b) Absolute value of the wavelet representation for $J = -3$: the left texture can be discriminated with a first order statistical analysis of the detail signals.

$$\forall r, \quad F(x) \quad \text{and} \quad r^H F(rx) \quad \text{are statistically identical.}$$

Hence, a realization of $F(x)$ looks similar at any scale and for any resolution. Fractal do not provide a general model which can be extended for any kind of texture, however S. Pentland [40] has shown that for a fractal texture, the psychophysical perception of roughness can be quantified with the fractal dimension. Fig. 1.23(a) shows a realization of a fractal noise which looks like a cloud. Its fractal dimension is 2.5. Fig. 1.23(b) gives the wavelet representation of this fractal. The detail signals are similar at all resolutions. The $A^{-3}f_d$ image gives the local DC component of the image, which would correspond to the local differences of illuminations for a cloud. Let us show that the fractal dimension can easily be computed from the wavelet representation. We give the proof for a one-dimensional fractal noise but it can be easily extended to two dimensions. The power spectrum of a fractal noise is given by [32]

$$P(\omega) = k \omega^{-2H-1}. \quad (1.53)$$

The fractal dimension is related to the exponent H by

$$D = T + 1 - H , \quad (1.54)$$

where T is the topological dimension of the space in which x varies (for images $T = 2$). Since a Brownian fractal noise is not a stationary process, this power spectrum can not be understood in the classical sense. P. Flandrin [12] has shown how to define precisely this power spectrum formula with a time-frequency analysis. We have seen in (1.25) that the detail signals D_j are obtained by filtering the signal with $\psi(-x)$ and sampling the output. The power spectrum of the filtered signal is

$$P_j(\omega) = P(\omega) |\hat{\psi}(2^{-j}\omega)|^2 . \quad (1.55)$$

After sampling at a rate 2^j , the power spectrum is given by [39]

$$P'_j = 2^j \sum_{k=-\infty}^{+\infty} P_j(\omega + 2^j 2k\pi) . \quad (1.56)$$

Let σ_j^2 be the variance of the detail signal D_j ,

$$\sigma_j^2 = \frac{2^{-j}}{2\pi} \int_{-2\pi}^{+2\pi} P'_j(\omega) d\omega . \quad (1.57)$$

By inserting equations (1.55) and (1.56) into (1.57) and using the change of variable $\omega' = 2\omega$ in this integral we can prove that

$$\sigma_j^2 = 2^{2H} \sigma_{j+1}^2 . \quad (1.58)$$

For a fractal, the ratio $\frac{\sigma_j^2}{\sigma_{j+1}^2}$ should thus be constant. Equation (1.58) enables us to compute H , and then the fractal dimension D can be computed with equation (1.54). A similar algorithm was proposed by D. Heeger and S. Pentland for analyzing fractal with Gabor functions [18]. In two dimensions we can derive an equation similar to (1.58) for each orientation tuning of the detail signal. For the fractal shown in Fig. 1.23(a) we have calculated these ratios in each orientation for the first three levels. The maximum error on the fractal dimension derived from each of these ratios was 3%.

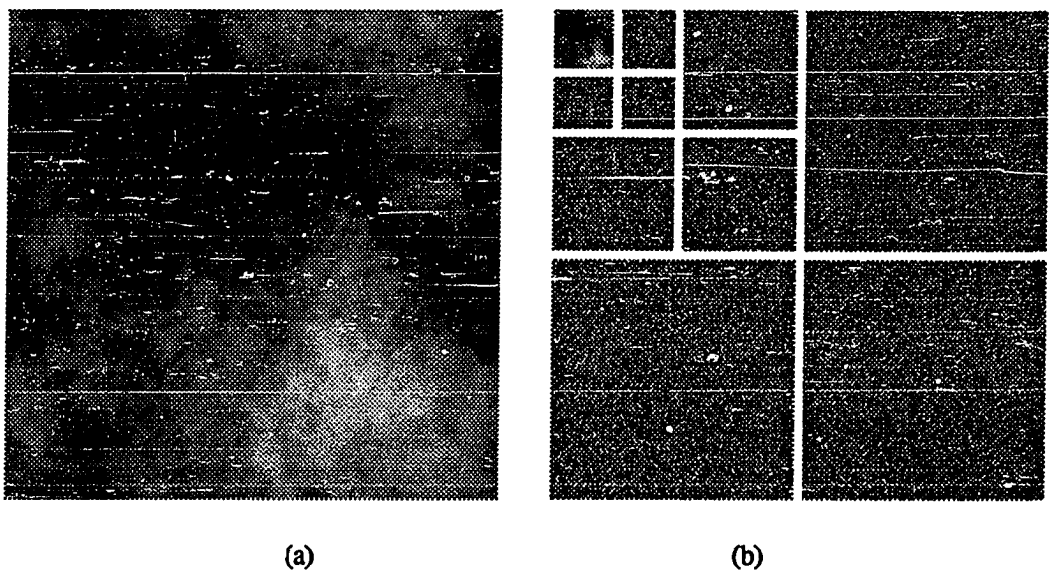


Fig. 1.23. (a) Fractal noise. (b) Wavelet representation for $J = -3$. The detail signals are similar for each resolution.

1.6. Distortion with translation

The fundamental drawback of an orthogonal wavelet decomposition for pattern recognition applications is that such a representation does not translate. We saw in equation (1.27) that the discrete detail signals could be interpreted as a uniform sampling at the rate 2^j of the continuous function $W^j f(x) = f * \bar{\psi}^j(x)$. Let $f(x) \in L^2(\mathbb{R})$, and let $g(x) = f(x-\tau)$ be a translation of $f(x)$ by τ . It is clear that $W^j g(x) = W^j f(x-\tau)$. However, the sampling of $W^j g(x)$ does not correspond to a translation of the sampling of $W^j f(x)$ unless $\tau = k2^j$, $k \in \mathbb{Z}$ (see Fig. 1.24). This distortion through translation implies that the wavelet coefficients of a pattern at the resolution 2^j depend upon the position of the pattern modulo 2^{-j} . This property is inherent to the notion of resolution. Indeed, at the resolution 2^j we cannot measure anything smaller than 2^{-j} so we cannot represent a displacement smaller than 2^{-j} . One can find the same problem in all the pyramidal multiresolution representations. It is thus difficult to achieve any pattern recognition operation from such representations.

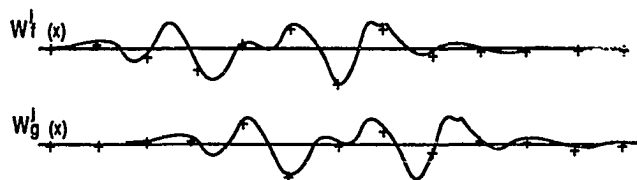


Fig. 1.24 This drawing shows that the sampling of a wavelet transform (given by the crosses) is very different after translating the signal. The sampling does not translate if the translation is not proportional to the sampling rate.

CHAPTER 2

MULTIRESOLUTION APPROXIMATIONS AND WAVELET ORTHONORMAL BASES

2.1. Introduction

In this chapter, we study the mathematical properties of the multiresolution approximations of $L^2(\mathbb{R})$ and how they relate to the wavelet orthonormal bases [29]. We prove theorems 1.1, 1.2, 1.3, 1.4 given in chapter 1.

Definition

A multiresolution approximation of $L^2(\mathbb{R})$ is a sequence $\left[V_j \right]_{j \in \mathbb{Z}}$ of closed subspaces of $L^2(\mathbb{R})$ such that the following hold :

$$\forall j \in \mathbb{Z}, \quad V_j \subset V_{j+1} \quad (2.1)$$

$$\bigcup_{j=-\infty}^{+\infty} V_j \text{ is dense in } L^2(\mathbb{R}) \quad \text{and} \quad \bigcap_{j=-\infty}^{+\infty} V_j = \{0\} \quad (2.2)$$

$$\forall j \in \mathbb{Z}, \quad f(x) \in V_j \iff f(2x) \in V_{j+1} \quad (2.3)$$

$$\forall k \in \mathbb{Z}, \quad f(x) \in V_j \implies f(x - 2^{-j}k) \in V_j \quad (2.4)$$

There exists an isomorphism I_0 from V_0 onto $L^2(\mathbb{Z})$ which commutes with the action of \mathbb{Z} . (2.5)

In (2.5) the action of \mathbb{Z} over V_0 is defined by (2.4), whereas the action of \mathbb{Z} over $L^2(\mathbb{Z})$ is the usual translation. We saw in chapter 1 that the approximation of a function $f(x) \in L^2(\mathbb{R})$ at a resolution 2^j is defined as the orthogonal projection of $f(x)$ on V_j . We first prove theorem 1.1 and show that there exists a unique function $\phi(x) \in L^2(\mathbb{R})$ such that, for any $j \in \mathbb{Z}$, $\left[\sqrt{2^j} \phi(2^j x - k) \right]_{k \in \mathbb{Z}}$ is an orthonormal basis of V_j . We then show that the

Fourier transform of $\phi(x)$ is characterized by a 2π periodic function $H(\omega)$ as described in theorem 1.2.

The additional information contained in the approximation at resolution 2^{j+1} , as compared with the approximation at the resolution 2^j is given by the orthogonal projection on the orthogonal complement \mathbf{O}_j of \mathbf{V}_j in \mathbf{V}_{j+1} . We show that there exists an orthogonal wavelet $\psi(x)$ such that $\left[\sqrt{2^j} \psi(2^j x - k) \right]_{k \in \mathbb{Z}}$ is an orthonormal basis of \mathbf{O}_j . Since the direct sum of $\left[\mathbf{O}_j \right]_{j \in \mathbb{Z}}$ is equal to $\mathbf{L}^2(\mathbb{R})$, $\left[\sqrt{2^j} \psi(2^j x - k) \right]_{(k,j) \in \mathbb{Z}^2}$ is an orthonormal basis of $\mathbf{L}^2(\mathbb{R})$. If $\psi(x)$ is regular enough, a remarkable property of these bases is to provide an unconditional basis of most of the classical functional spaces : the Sobolev spaces, Hardy spaces, \mathbf{L}^p spaces [26] and others.

An important problem in approximation theory [9] is to estimate the asymptotic decreasing of the approximation error, given an a priori knowledge on the smoothness of the approximated function. By using the properties of wavelet orthonormal bases, we can compute the asymptotic behavior of the approximation error for functions in a Sobolev space \mathbf{H}^s . We show that this result is a characterization of \mathbf{H}^s . Finally, we briefly describe the two-dimensional separable extension of wavelet orthonormal bases studied by Y. Meyer [37] and prove theorem 1.4.

2.2. The scaling function $\phi(x)$

Notations: Let us recall that we denote by $F\mathbf{V}$ the image under the Fourier transform of a subspace \mathbf{V} of $\mathbf{L}^2(\mathbb{R})$. $\langle \dots, \dots \rangle$ denotes the inner product in a Hilbert space and Id denotes the identity operator.

This paragraph gives a proof of theorem 1.1. Because of property (2.3) of a multiresolution approximation, it is clearly sufficient to prove this theorem for $j = 0$. Let us first detail the property (2.5) of a multiresolution approximation. There exists a function $g(x)$ satisfying

$$g(x) \in \mathbf{V}_0 \quad \text{and} \quad I_0(g) = \varepsilon_0, \quad \text{where} \quad \varepsilon_0(k) = \begin{cases} 1 & \text{if } k = 0 \\ 0 & \text{if } k \neq 0 \end{cases}.$$

Let $k \in \mathbb{Z}$ and $g_k(x) = g(x - k)$. Since the isomorphism I_0 commutes with the translation of an integer,

$$I_0(g_k) = \varepsilon_k, \text{ where } \varepsilon_k(n) = \begin{cases} 1 & \text{if } n = k \\ 0 & \text{if } n \neq k \end{cases}.$$

The sequence $\{\varepsilon_k\}_{k \in \mathbb{Z}}$ is a basis of $L^2(\mathbb{Z})$, so the function $g(x)$ characterizes the isomorphism I_0 . Any function $f(x) \in V_0$ can be decomposed in a unique way :

$$f(x) = \sum_{k=-\infty}^{+\infty} \alpha_k g(x-k). \quad (2.6)$$

Since I_0 is an isomorphism, $\|f\|^2$ and $\left(\sum_{k=-\infty}^{+\infty} |\alpha_k|^2 \right)^{1/2}$ are two equivalent norms on V_0 .

We are looking for a function $\phi(x)$ such that $\{\phi(x-k)\}_{k \in \mathbb{Z}}$ is an orthonormal basis of V_0 . To compute $\phi(x)$ we must orthogonalize the family of functions $\{g(x-k)\}_{k \in \mathbb{Z}}$. We can use two methods for this purpose, both useful. The simplest one uses the Fourier transform and is based on a characterization of FV_0 .

$$\hat{f}(\omega) \in FV_0 \iff \hat{f}(\omega) = m(\omega) \hat{g}(\omega) \text{ where } m(\omega) = \sum_{k=-\infty}^{+\infty} \alpha_k e^{ik\omega}.$$

Since $\|\hat{f}\|_2$ and $\left(\sum_{k=-\infty}^{+\infty} |\alpha_k|^2 \right)^{1/2}$ are two equivalent norms on FV_0 , it follows that

$$\exists C_1 > 0, \exists C_2 > 0 \text{ such that } \forall \omega \in \mathbb{R} \quad C_1 \leq \left[\sum_{k=-\infty}^{+\infty} |\hat{g}(\omega+2k\pi)|^2 \right]^{1/2} \leq C_2. \quad (2.7)$$

Since $\hat{\phi}(\omega) \in FV_0$, we can find $m_\phi(\omega)$ such that

$$\hat{\phi}(\omega) = m_\phi(\omega) \hat{g}(\omega). \quad (2.8)$$

The family of functions $\{\phi(x-k)\}_{k \in \mathbb{Z}}$ is orthonormal if and only if (the Poisson formula)

$$\sum_{k=-\infty}^{+\infty} |\hat{\phi}(\omega+2k\pi)|^2 = 1 \text{ almost everywhere},$$

$$\text{hence } m_\phi(\omega) = \left[\sum_{k=-\infty}^{+\infty} |\hat{g}(\omega+2k\pi)|^2 \right]^{-1/2}. \quad (2.9)$$

A function $f(x) \in L^2(\mathbb{R})$ is said to be regular if and only if

$$f(x) \in C^1 \text{ and } \exists C > 0, \forall x \in \mathbb{R}, |f(x)| \leq C(1+x^2)^{-1} \text{ and } |f'(x)| \leq C(1+x^2)^{-1}.$$

Let us prove that the function $\phi(x)$ defined by (2.8) and (2.9) is regular if $g(x)$ is regular. Hence, we must show that

$$m_\phi(\omega) = \sum_{k=-\infty}^{+\infty} \alpha_k e^{ik\omega} \text{ with } |\alpha_k| \leq C (1+k^2)^{-1}. \quad (2.10)$$

The Banach space of 2π periodic continuous functions characterized by (2.10) is a commutative Banach algebra with the involution which associates to $m(\omega)$ its complex conjugate $\bar{m}(\omega)$. This algebra is invariant under the action of analytic functions, i.e., if $m(\omega)$ satisfies (2.10) and $G(z)$ is an analytic function with domain containing the range of $m(\omega)$, then $G \circ m$ satisfies (2.10). On the other hand, $\sum_{k=-\infty}^{+\infty} |g(\omega+2k\pi)|^2$ is a member of our algebra because $g(x)$ is regular. We can thus use $z^{-1/2}$ in the complex plane without $]-\infty, 0]$ to derive (2.10). From (2.10) we can then conclude that $\phi(x)$ is regular. A multiresolution approximation is said to be regular if $\phi(x)$ is regular.

The second approach for building the function ϕ is based on the general algorithm for orthogonalizing an unconditional basis $\left[e_\lambda \right]_{\lambda \in \Lambda}$ of a Hilbert space \mathbf{H} . This approach was suggested by Y. Meyer. Let us recall that a sequence $\left[e_\lambda \right]_{\lambda \in \Lambda}$ is a normalized unconditional basis if there exist two positive constants C_1 and C_2 such that for any sequence of numbers $\left[\alpha_\lambda \right]_{\lambda \in \Lambda}$,

$$C_1 \left(\sum_{\lambda \in \Lambda} |\alpha_\lambda|^2 \right)^{1/2} \leq \left\| \sum_{\lambda \in \Lambda} \alpha_\lambda e_\lambda \right\| \leq C_2 \left(\sum_{\lambda \in \Lambda} |\alpha_\lambda|^2 \right)^{1/2}. \quad (2.11)$$

We first compute the Gram matrix \mathbf{G} , indexed by $\Lambda \times \Lambda$, whose coefficients are $\langle e_{\lambda_1}, e_{\lambda_2} \rangle$. Equation (2.11) is equivalent to

$$C_1^2 \text{Id} \leq \mathbf{G} \leq C_2^2 \text{Id}. \quad (2.12)$$

This equation shows that we can calculate $\mathbf{G}^{-1/2}$, whose coefficients are written $\gamma(\lambda_1, \lambda_2)$. Let us define the vectors $f_\lambda = \sum_{\lambda' \in \Lambda} \gamma(\lambda, \lambda') e_{\lambda'}$. It is well known that the family $\left[f_\lambda \right]_{\lambda \in \Lambda}$ is an orthonormal basis of \mathbf{H} . This algorithm has the advantage with respect to the usual Gram-Schmidt procedure, to preserve any supplementary structure (invariance under the action of a

group , symmetries) which might exist in the sequence $\left[e_\lambda \right]_{\lambda \in \Lambda}$. In our particular case we verify immediately that both methods lead to the same result. The second one is more general and can be used when the multiresolution approximation is defined on a Hilbert space where the Fourier transform does not exist [36].

2.3. Definition of a multiresolution approximation from $H(\omega)$

In this paragraph we give a proof of theorem 1.2. We prove separately the necessary and sufficient conditions of this theorem. We have shown that there exists a unique function $\phi(x)$ such that $\left[\phi(x-k) \right]_{k \in \mathbb{Z}}$ is an orthonormal basis of V_0 . Property (2.2) of a multiresolution approximation implies that

$$\frac{1}{2} \phi\left(\frac{x}{2}\right) \in V_{-1} \subset V_0 .$$

The function $\frac{1}{2} \phi\left(\frac{x}{2}\right)$ can thus be decomposed in the orthonormal basis $\left[\phi(x-k) \right]_{k \in \mathbb{Z}}$:

$$\frac{1}{2} \phi\left(\frac{x}{2}\right) = \sum_{k=-\infty}^{\infty} \beta_k \phi(x+k) \quad \text{where} \quad \beta_k = \frac{1}{2} \int_{-\infty}^{\infty} \phi\left(\frac{x}{2}\right) \bar{\phi}(x+k) dx . \quad (2.13)$$

For a regular multiresolution approximation, $|\beta_k| = O(1+k^2)^{-1}$. By taking the Fourier transform of both sides of equation (2.13) we obtain

$$\hat{\phi}(2\omega) = H(\omega) \hat{\phi}(\omega) \quad \text{where} \quad H(\omega) = \sum_{k=-\infty}^{\infty} \beta_k e^{ik\omega} . \quad (2.14)$$

The following theorem gives the necessary condition of theorem 1.2.

Theorem 2.1

The function $\tilde{H}(\omega)$ as defined above satisfies :

$$|H(\omega)|^2 + |H(\omega + \pi)|^2 = 1 \quad (2.15)$$

$$H(0) = 1 \quad (2.16)$$

Proof: The proof of (2.15) is straightforward.

$$\sum_{k=-\infty}^{+\infty} |\hat{\phi}(\omega+2k\pi)|^2 = 1 \quad \text{so} \quad \sum_{k=-\infty}^{+\infty} |\hat{\phi}(2\omega+2k\pi)|^2 = 1 .$$

Since $\hat{\phi}(2\omega) = H(\omega) \hat{\phi}(\omega)$, this second summation yields

$$\sum_{k=-\infty}^{+\infty} |H(\omega+k\pi)|^2 |\hat{\phi}(\omega+k\pi)|^2 = 1 .$$

$H(\omega)$ is 2π periodic, so by regrouping the terms for $k \in 2\mathbb{Z}$ and $k \in 2\mathbb{Z}+1$ we obtain

$$|H(\omega)|^2 + |H(\omega+\pi)|^2 = 1 .$$

In order to prove that $H(0) = 1$, we use the regularity of the multiresolution approximation. We show that $\hat{\phi}(0) \neq 0$ and more precisely that $|\hat{\phi}(0)| = 1$. Let A^j be the orthogonal projection on V_j . The kernel of A^j is

$$2^j K(2^j x, 2^j y) , \text{ where } K(x, y) = \sum_{k=-\infty}^{\infty} \phi(x-k) \bar{\phi}(y-k) . \quad (2.17)$$

Lemma 2.1

Let $\phi(x)$ be a regular function and $K(x, y) = \sum_{k=-\infty}^{\infty} \phi(x-k) \bar{\phi}(y-k)$. The following two properties are equivalent:

$$\int_{-\infty}^{\infty} K(x, y) dy = 1 \quad \text{for almost all } x . \quad (2.18)$$

The sequence of operators $\left[I_j \right]_{j \in \mathbb{Z}}$ whose kernels are $2^j K(2^j x, 2^j y)$ tends to Id in the sense of strong convergence for operators. (2.19)

Proof: Let us first prove that (2.18) implies (2.19). It is clear that the sequence of operators $\left[I_j \right]_{j \in \mathbb{Z}}$ is bounded over $L^2(\mathbb{R})$. To prove that

$$\forall j \in \mathbb{Z}, \forall f \in L^2(\mathbb{R}) \quad \lim_{j \rightarrow \infty} \|f - I_j(f)\|_2 = 0 , \quad (2.20)$$

it is thus sufficient to restrict ourselves to indicator functions of intervals. Let $f(x)$ be the indicator function of an interval $[a, b]$ ($f(x) = 1$ if $a \leq x \leq b$, $f(x) = 0$ otherwise). Since $\phi(x)$ is regular, $\exists C > 0$ such that $|K(x,y)| \leq C (1 + |x-y|)^{-2}$. Hence

$$|I_j(f)(x)| \leq C 2^j \int_a^b (1 + 2^j |x-y|)^{-2} dy \leq \frac{C'}{1+x^2}. \quad (2.21)$$

If x is not member of $[a, b]$, this inequality implies that $I_j(f)(x)$ tends to 0. If x is inside $[a, b]$, (2.18) implies that $I_j(f)(x)$ tends to 1. The second inequality of (2.21) enables us to apply the dominated convergence theorem and thus to conclude (2.20).

Conversely let us show that (2.19) implies (2.18). For this purpose we consider the particular case where $f(x)$ is the indicator function of $[-1, 1]$. If $|x| \leq r < 1$,

$$I_j(f)(x) = \int_{-1}^1 2^j K(2^j x, 2^j y) dy = \alpha(2^j x) + O(2^{-j}) \text{ where } \alpha(x) = \int_{-\infty}^{\infty} K(x, y) dy \in L^\infty(\mathbb{R}).$$

The function $\alpha(x)$ is periodic with period 1. Since $\alpha(2^j x)$ converges strongly to 1 in $L^2([-r, r])$, $\alpha(x)$ must therefore be equal to 1.

(end of lemma 2.1 proof)

Coming back to the operators $A^j(f)$, the properties (2.1) and (2.2) imply that the sequence of operators $\left[A^j \right]_{j \in \mathbb{Z}}$ tends to \mathbf{I} in the sense of strong convergence for operators. Applying lemma 2.1, (2.18) implies that

$$\int_{-\infty}^{+\infty} \sum_{k=-\infty}^{\infty} \phi(x-k) \bar{\phi}(y-k) dy = 1 \quad \text{and thus} \quad \sum_{k=-\infty}^{\infty} \bar{\gamma} \phi(x-k) = 1 \quad \text{where} \quad \gamma = \int_{-\infty}^{\infty} \phi(y) dy \quad (2.22)$$

By integrating in x on $[0, 1]$, this equation yields $|\gamma|^2 = 1$. With the Poisson formula, it follows from (2.22) that

$$\hat{\phi}(0) = (\bar{\gamma})^{-1} \quad \text{and} \quad \forall k \in \mathbb{Z}^* \quad \hat{\phi}(2k\pi) = 0. \quad (2.23)$$

From equation (2.14), we can now conclude that $H(0) = 1$.

(end of theorem 2.1 proof)

In the following, we normalize ϕ with $\bar{\gamma}$ so that $\hat{\phi}(0) = 1$. The following theorem gives the sufficiency condition stated in theorem 1.2.

Theorem 2.2

Let $H(\omega)$ be a differentiable 2π periodic function such that

$$H(0) = 1 \quad \text{and} \quad |H(\omega)|^2 + |H(\omega + \pi)|^2 = 1 \quad (2.24)$$

$$H(\omega) \neq 0 \quad \text{on} \quad [-\frac{\pi}{2}, \frac{\pi}{2}] \quad (2.25)$$

$$\text{Let } \hat{\phi}(\omega) = \prod_{k=1}^{\infty} H(2^{-k}\omega). \quad (2.26)$$

Then $\hat{\phi}(\omega)$ is the Fourier transform of a function $\phi(x)$ such that $\left[\phi(x-k) \right]_{k \in \mathbb{Z}}$ is an orthonormal basis of a closed subspace V_0 of $L^2(\mathbb{R})$. If $\phi(x)$ is regular, then the sequence of vector space V_j defined by (2.2) is a regular multiresolution approximation of $L^2(\mathbb{R})$.

Proof : To simplify notations we write $h(\omega) = |H(\omega)|^2$ and denote by $h_k(\omega)$ ($k \geq 1$) the continuous function such that

$$h_k(\omega) = \begin{cases} 0 & \text{if } |\omega| > 2^k\pi \\ h(\frac{\omega}{2})h(\frac{\omega}{4}) \cdots h(\frac{\omega}{2^k}) & \text{if } |\omega| \leq 2^k\pi \end{cases}$$

Lemma 2.2

For all $k \in \mathbb{N}, k \neq 0$,

$$I_k^n = \int_{-\infty}^{\infty} h_k(\omega) e^{i2n\pi\omega} d\omega = \begin{cases} 2\pi & \text{if } n=0 \\ 0 & \text{if } n \neq 0 \end{cases} \quad (2.27)$$

Proof : Let us divide the integral I_k^n into two parts :

$$I_k^n = \int_{-2^k\pi}^0 h_k(\omega) e^{i2n\pi\omega} d\omega + \int_0^{2^k\pi} h_k(\omega) e^{i2n\pi\omega} d\omega.$$

By substituting the variable $\omega' = \omega + 2^k\pi$ in the first integral and using $h(2^{-j}\omega + 2^{k-j}\pi) = h(2^{-j}\omega)$ for $0 \leq j < k$ and $h(2^{-k}\omega) + h(2^{-k}\omega + \pi) = 1$, we can regroup these two integrals into

$$\int_0^{2^k\pi} h\left(\frac{\omega}{2}\right) \cdots h\left(\frac{\omega}{2^{k-1}}\right) e^{i2n\pi\omega} d\omega = \int_{-2^{k-1}\pi}^{2^{k-1}\pi} h\left(\frac{\omega}{2}\right) \cdots h\left(\frac{\omega}{2^{k-1}}\right) e^{i2n\pi\omega} d\omega = I_k^k .$$

Therefore, $I_k^k = I_{k-1}^k = \cdots = I_1^k = \begin{cases} 2\pi & \text{if } n=0 \\ 0 & \text{if } n \neq 0 \end{cases}$.

(end of lemma 2.2 proof)

Let us now consider the infinite product

$$h_\infty(\omega) = \lim_{k \rightarrow \infty} h_k(\omega) = \prod_{j=1}^{\infty} h(2^{-j}\omega) .$$

Since $0 \leq h(\omega) \leq 1$, this product converges. From Fatou's lemma we derive that

$$\int_{-\infty}^{\infty} h_\infty(\omega) d\omega \leq \lim_{k \rightarrow \infty} \int_{-\infty}^{\infty} h_k(\omega) d\omega = 2\pi . \quad (2.28)$$

Since $h(\omega)$ is differentiable in 0 and $h(0) = 1$, $\text{Log}(h(\omega)) = O(\omega)$ in the neighborhood of 0.

$$h_\infty(\omega) = e^{-\sum_{j=1}^{\infty} \text{Log}(h(2^{-j}\omega))} \quad \text{hence} \quad \lim_{\omega \rightarrow 0} h_\infty(\omega) = h_\infty(0) = 1 . \quad (2.29)$$

From (2.25) and (2.29), it follows that

$$\exists C > 0 \text{ such that } \forall \omega \in [-\pi, \pi] \quad h_\infty(\omega) \geq C . \quad (2.30)$$

For $|\omega| \leq 2^k\pi$, $h_\infty(\omega) = h_k(\omega) h_\infty\left(\frac{\omega}{2^k}\right)$, it thus follows from (2.30) that

$$0 \leq h_k(\omega) \leq \frac{1}{C} h_\infty(\omega) . \quad (2.31)$$

Since $h_k(\omega) = 0$ for $|\omega| > 2^k\pi$, the inequality (2.31) is verified for all $\omega \in \mathbb{R}$. By applying the dominated convergence theorem on the sequence $\left[h_k(\omega) e^{i2n\pi\omega} \right]_{k \in \mathbb{Z}}$ we derive from lemma 2.2 that

$$\int_{-\infty}^{\infty} h_\infty(\omega) e^{i2n\pi\omega} d\omega = \begin{cases} 2\pi & \text{if } n=0 \\ 0 & \text{if } n \neq 0 \end{cases} . \quad (2.32)$$

Equation (2.26) thus defines the Fourier transform of a function $\phi(x)$ in $L^2(\mathbb{R})$ such that $\{\phi(x-k)\}_{k \in \mathbb{Z}}$ is an orthonormal family. We call \mathbf{V}_0 the vector space generated by this orthonormal family.

Let us suppose now that ϕ is regular. Let $\{\mathbf{V}_j\}_{j \in \mathbb{Z}}$ be the sequence of vector spaces derived from \mathbf{V}_0 with property (2.3). To prove that this sequence satisfies the property (2.1), it is sufficient to show that $\mathbf{V}_{-1} \subset \mathbf{V}_0$. The vector spaces $F\mathbf{V}_0$ and $F\mathbf{V}_{-1}$ are respectively the set of all functions $m(\omega)\hat{\phi}(\omega)$ and $m(2\omega)\hat{\phi}(2\omega)$ where $m(\omega)$ is any 2π periodic function such that $m(\omega) \in L^2([0, 2\pi])$. We have seen in (2.14) that $\hat{\phi}(2\omega) = H(\omega)\hat{\phi}(\omega)$ where $|H(\omega)| \leq 1$. Since the function $m(2\omega)H(\omega)$ is in $L^2([0, 2\pi])$ and is 2π periodic, we can conclude that $F\mathbf{V}_{-1} \subset F\mathbf{V}_0$ and $\mathbf{V}_{-1} \subset \mathbf{V}_0$.

To prove (2.2), we must verify that

$$\lim_{j \rightarrow +\infty} A^j = \text{Id} \quad \text{and} \quad \lim_{j \rightarrow -\infty} A^j = 0 , \quad (2.33)$$

where A^j is the orthogonal projection operator on \mathbf{V}_j . By definition, the kernel of A^j is

$$2^j \sum_{k=-\infty}^{\infty} \phi(2^j x - k) \bar{\phi}(2^j y - k) = 2^j K(2^j x, 2^j y) .$$

From (2.29) we can derive that $\hat{\phi}(0) = 1$ and (2.24) and (2.25) imply that $\hat{\phi}(2k\pi) = 0$ for $k \neq 0$. With the Poisson formula, it thus follows that

$$\int_{-\infty}^{+\infty} K(x, y) dy = \sum_{k=-\infty}^{\infty} \phi(x - k) = 1 \quad \text{for almost all } x .$$

From the above we conclude the first part of (2.33) by using lemma 2.1. The second part of (2.33) can be easily derived from the inequality (2.21) on $2^j |A(2^j x, 2^j y)|$.

(end of theorem 2.2 proof)

Remarks

1. The necessary conditions on $H(\omega)$ stated in theorem 2.1 are not sufficient to define a function ϕ such that $\{\phi(x-k)\}_{k \in \mathbb{Z}}$ is an orthonormal family. The function $H(\omega) = \cos(\frac{3\omega}{2})$ is a counter-example : $\phi(x)$ is then equal to $\frac{1}{3}$ in $[-\frac{3}{2}, \frac{3}{2}]$ and 0 elsewhere.

However, we do not know whether the sufficient conditions introduced in theorem 2.2 are also necessary.

2. It is possible to control the smoothness of $\hat{\phi}(\omega)$ from $H(\omega)$. One can show that if $H(\omega) \in \mathbf{C}^q$ then $\hat{\phi}(\omega) \in \mathbf{C}^q$ and

$$\frac{d^n H(0)}{d\omega^n} = 0 \quad \text{for } 1 \leq n \leq q \iff \frac{d^n \hat{\phi}(0)}{d\omega^n} = 0 \quad \text{for } 1 \leq n \leq q. \quad (2.34)$$

A result of I. Daubechies [7] and P. Tchamitchian [45] also gives a lower bound for the decreasing rate of $\hat{\phi}(\omega)$ at infinity. If $\frac{d^n H(0)}{d\omega^n} = 0$ for $1 \leq n \leq q$ then (2.24) yields $\frac{d^n H((2k+1)\pi)}{d\omega^n} = 0$, for $0 \leq n \leq q-1$ and $k \in \mathbb{Z}$. We can thus find a 2π -periodic function $\tilde{m}_0(\omega)$ such that

$$H(\omega) = \left[\cos\left(\frac{\omega}{2}\right) \right]^q \tilde{m}_0(\omega) \quad \text{and} \quad \exists M > 0, \sup_{\omega \in [0, 2\pi]} |\tilde{m}_0(\omega)| \leq M.$$

One can show that

$$\prod_{j=-1}^{+\infty} |\tilde{m}_0(2^{-j}\omega)| = O(|\omega|^{\frac{\log(M)}{\log(2)}})$$

at infinity. Since

$$\prod_{j=-1}^{+\infty} \cos(2^{-j}\frac{\omega}{2}) = \frac{\sin(\frac{\omega}{2})}{\frac{\omega}{2}}$$

it follows that

$$|\hat{\phi}(\omega)| = O(|\omega|^{-q + \frac{\log(M)}{\log(2)}}) \quad \text{at infinity}. \quad (2.35)$$

I. Daubechies [7] has also proved that we could find functions $H(\omega)$ such that $q - \frac{\log(M)}{\log(2)}$ is

arbitrarily large. We can thus compute some functions $\phi(x)$ which are as smooth as desired.

2.4. The wavelet orthonormal basis

The approximation of a function $f(x) \in L^2(\mathbb{R})$ was defined as the orthogonal projection of $f(x)$ on V_j . The increment of precision of the approximation when the resolution increases from 2^j to 2^{j+1} is thus given by the orthogonal projection on the orthogonal complement of V_j in V_{j+1} . Let us call this vector space O_j . In this paragraph, we describe an algorithm, which is now classic [36], in order to find a wavelet $\psi(x)$ such that $\left[\sqrt{2^j} \psi(2^j x - k) \right]_{k \in \mathbb{Z}}$ is an orthonormal basis of O_j .

We are looking for a function $\psi(x)$ such that $\psi\left(\frac{x}{2}\right) \in V_0$. Its Fourier transform can thus be written

$$\hat{\psi}(2\omega) = G(\omega) \hat{\phi}(\omega), \quad (2.36)$$

where $G(\omega)$ is a 2π periodic function in $L^2([0, 2\pi])$. Since $V_0 = V_{-1} \oplus O_{-1}$, the Fourier transform of any function $f(x) \in V_0$ can be decomposed as

$$\hat{f}(\omega) = a(\omega) \hat{\phi}(\omega) = b(\omega) \hat{\phi}(2\omega) + c(\omega) \hat{\psi}(2\omega),$$

where $a(\omega)$ is 2π periodic and member of $L^2([0, 2\pi])$ and $b(\omega), c(\omega)$ are both π periodic and members of $L^2([0, \pi])$. By inserting (2.14) and (2.36) in the previous equation, it follows that

$$a(\omega) = b(\omega) H(\omega) + c(\omega) G(\omega). \quad (2.37)$$

The orthogonality of the decomposition can be expressed as

$$\int_0^{2\pi} |a(\omega)|^2 d\omega = \int_0^\pi |b(\omega)|^2 d\omega + \int_0^\pi |c(\omega)|^2 d\omega.$$

This equation is verified for any $a(\omega)$ if and only if

$$\begin{cases} |H(\omega)|^2 + |G(\omega)|^2 = 1 \\ H(\omega) \overline{G(\omega)} + H(\omega+\pi) \overline{G(\omega+\pi)} = 0 \end{cases}. \quad (2.38)$$

Condition (2.38) together with (2.15) can also be expressed by writing that the matrix

$$S(\omega) = \begin{bmatrix} H(\omega) & G(\omega) \\ H(\omega+\pi) & G(\omega+\pi) \end{bmatrix} \quad (2.39)$$

is unitary.

The functions $b(\omega)$ and $c(\omega)$ are respectively given by

$$\begin{cases} b(\omega) = a(\omega) \overline{H(\omega)} + a(\omega+\pi) \overline{H(\omega+\pi)} \\ c(\omega) = a(\omega) \overline{G(\omega)} + a(\omega+\pi) \overline{G(\omega+\pi)} \end{cases} \quad (2.40)$$

A possible choice for $G(\omega)$ is

$$G(\omega) = e^{-i(\omega+\alpha)} \overline{H(\omega+\pi)} , \quad (2.41)$$

where α is a constant phase.

The vector spaces \mathbf{V}_J can be written $\mathbf{V}_J = \bigoplus_{j=-\infty}^{J-1} \mathbf{O}_j$. Since $\bigcup_{j=-\infty}^{+\infty} \mathbf{V}_j$ is dense in $L^2(\mathbb{R})$, we have $L^2(\mathbb{R}) = \bigoplus_{j=-\infty}^{+\infty} \mathbf{O}_j$. The family of functions $\{\sqrt{2^j} \psi(2^j x - k)\}_{(k,j) \in \mathbb{Z}^2}$ is therefore an orthonormal basis of $L^2(\mathbb{R})$. The Haar basis is a particular case where

$$\psi(x) = \begin{cases} 1 & \text{if } 0 \leq x < \frac{1}{2} \\ -1 & \text{if } \frac{1}{2} \leq x < 1 \\ 0 & \text{otherwise.} \end{cases}$$

It corresponds to $H(\omega) = \cos(\frac{\omega}{2})$ and $\alpha = \frac{\pi}{2}$ in (2.41). The function $\phi(x)$ is the indicator function of $[-\frac{1}{2}, \frac{1}{2}]$, so the associated multiresolution approximation is not regular. With some other choice of $H(\omega)$, we can compute some wavelets which are much more regular than the Haar wavelet.

The smoothness and the asymptotic decreasing rate of a wavelet $\psi(x)$ defined by (2.36) and (2.41) can partially be controlled from the behavior of $H(\omega)$. The asymptotic decreasing rate of $\psi(x)$ can be estimated by observing that if $H(\omega) \in \mathbb{C}^q$, then $\hat{\psi}(\omega) \in \mathbb{C}^q$ and

$$\frac{d^n H(0)}{d\omega^n} = 0 \quad \text{for } 1 \leq n \leq q \iff \begin{cases} \frac{d^n G(0)}{d\omega^n} = 0 & \text{for } 0 \leq n \leq q-1 \\ \frac{d^n \hat{\psi}(0)}{d\omega^n} = 0 & \text{for } 0 \leq n \leq q-1 \end{cases} \quad (2.42)$$

Concerning the smoothness of $\psi(x)$, we can derive from (2.35) a lower bound for the asymptotic decreasing rate of $\hat{\psi}(\omega)$: $|\hat{\psi}(\omega)| = O(|\omega|^{-q+\frac{\log(M)}{\log(2)}})$ at infinity.

Outside the Haar basis, the first class of wavelet orthonormal bases was found by Y.Meyer [37]. They correspond to all the functions $H(\omega)$ which are continuously differentiable at any order and equal to 1 on $[-\frac{\pi}{3}, \frac{\pi}{3}]$. The Fourier transform $\hat{\psi}(\omega)$ is in C^∞ , so $\psi(x)$ has a decay faster than any power. We can also easily derive that $\hat{\psi}(\omega)$ has a support included in $[-\frac{8\pi}{3}, \frac{8\pi}{3}]$ so $\psi(x)$ is in C^∞ .

By using a multiresolution approach, I. Daubechies [7] has recently proved that for any $n \geq 1$, we could find a wavelet $\psi(x) \in C^n$ having a compact support. She has shown that we could find a trigonometrical polynomial

$$H(\omega) = \sum_{k=0}^A \alpha_k e^{ik\omega}$$

satisfying $q - \frac{\log(M)}{\log(2)} > n+2$ in equation (2.35). Hence $|\hat{\phi}(\omega)| = O(|\omega|^{-n-2})$ at infinity and the associated wavelet defined by (2.36) and (2.41) has a support included in $[-\frac{(A-1)}{2}, \frac{(A-1)}{2}]$. Since we also have $|\hat{\psi}(\omega)| = O(|\omega|^{-n-2})$ at infinity, $\psi(x) \in C^n$.

If $\psi(x)$ is smooth enough, an important property of a wavelet orthonormal basis is to provide unconditional bases for most of the usual functional spaces [26]. We can thus find whether or not a function $f(x)$ is inside such spaces as $L^p(\mathbb{R})$ ($1 < p < \infty$) or the Hardy spaces from the behavior of the decomposition coefficients in the wavelet basis. In the next paragraph we use in particular the following result on Sobolev spaces.

If a wavelet $\psi(x)$ verifies

$$\exists C \geq 0, |\psi(x)| < C (1 + |x|)^{-1-q} \quad (2.43)$$

$$\int_{-\infty}^{+\infty} x^n \psi(x) dx = 0 \quad \text{for } 1 \leq n \leq q \quad (2.44)$$

$$\exists C \geq 0, \left| \frac{d^n \psi(x)}{dx^n} \right| < C (1 + |x|)^{-1-q} \quad \text{for } n \leq q \quad (2.45)$$

then $\forall s \leq q$ the family of functions $\left[\sqrt{2^j} \psi(2^j x - k) \right]_{(j,k) \in \mathbb{Z}^2}$ is an unconditional basis of the Sobolev space \mathbf{H}^s . As a consequence, for any $f(x) \in \mathbf{L}^2(\mathbf{R})$, if $\alpha(k,j) = \langle f(x), \sqrt{2^j} \psi(2^j x - k) \rangle$ then

$$f \in \mathbf{H}^s \iff \left[\sum_{j=-\infty}^{+\infty} \left\{ \left(\sum_{k=-\infty}^{+\infty} |\alpha(k,j)|^2 \right)^{\frac{1}{2}} 2^{js} \right\}^2 \right]^{\frac{1}{2}} < +\infty. \quad (2.46)$$

Remarks

1. We have seen that from any multiresolution approximation we can derive a wavelet orthonormal basis. It is however not true that we can build a multiresolution approximation from any wavelet basis. The function $\psi(x)$ whose Fourier transform is given by

$$\hat{\psi}(\omega) = \begin{cases} 1 & \text{if } \frac{4\pi}{7} \leq |\omega| \leq \pi \text{ or } 4\pi \leq |\omega| \leq 4\pi + \frac{4\pi}{7} \\ 0 & \text{otherwise} \end{cases}. \quad (2.47)$$

is a counter-example.

The translates and dilates $\left[\sqrt{2^j} \psi(2^j x - k) \right]_{(j,k) \in \mathbb{Z}^2}$ of this function constitute an orthonormal basis of $\mathbf{L}^2(\mathbf{R})$. Let \mathbf{V}_J be the vector space generated by the family of functions

$$\left[\sqrt{2^j} \psi(2^j x - k) \right]_{k \in \mathbb{Z}, -\infty < j < J}.$$

One can verify that the sequence of vector spaces $\left[\mathbf{V}_J \right]_{J \in \mathbb{Z}}$ does not satisfy the property (2.10) of a multiresolution approximation. Hence, the wavelet defined by (2.47) is not related to a multiresolution approximation. It might however be sufficient to impose a regularity condition on $\psi(x)$ in order to always generate a multiresolution approximation

2. Multiresolution approximations have been extended to $\mathbf{L}^2(\mathbf{R}^n)$ by Y.Meyer [36]. This enables us to build wavelet orthonormal bases of $\mathbf{L}^2(\mathbf{R}^n)$ with a similar algorithm.

2.5. Approximation error

The approximation error at the resolution 2^j is given by $\varepsilon_j = \|f - A^j(f)\|^2$. We known from (2.2) that $\lim_{j \rightarrow \infty} \varepsilon_j = 0$. A classical problem in approximation theory is to estimate the convergence rate of ε_j given an a priori knowledge on the smoothness of $f(x)$ and conversely derive the smoothness of $f(x)$ from the convergence rate of ε_j [9].

Theorem 2.3

Let $\left[\mathbf{V}_j \right]_{j \in \mathbb{Z}}$ be a multiresolution approximation such that the associated function ϕ satisfies

$$\exists C \geq 0, |\phi(x)| < C (1 + |x|)^{-3-q} \quad (2.48)$$

$$\int_{-\infty}^{+\infty} x^n \phi(x) dx = 0 \quad \text{for } 1 \leq n \leq q+1 \quad (2.49)$$

$$\exists C \geq 0, \left| \frac{d^n \phi(x)}{dx^n} \right| < C (1 + |x|)^{-1-q} \quad \text{for } n \leq q. \quad (2.50)$$

Then, for all $f \in L^2(\mathbb{R})$, if $0 < s \leq q$,

$$f(x) \in H^s \iff \|f - A^j(f)\|_2 = \varepsilon'_j 2^{-sj} \quad \text{where } \sum_{j=-\infty}^{+\infty} \varepsilon'^2_j < +\infty \quad (2.51)$$

Proof: Let $P_{\mathbf{O}_j}$ denote the orthogonal projection on the vector space \mathbf{O}_j and $\psi(x)$ be the wavelet defined by (2.36) and (2.41). Let $f(x)$ be in $L^2(\mathbb{R})$ and $\alpha(k,j) = \langle f(x), \sqrt{2^j} \psi(2^j x - k) \rangle$. Then

$$\|f - A^j(f)\|_2 = \left[\sum_{j=j}^{\infty} \|P_{\mathbf{O}_j}(f)\|^2 \right]^{\frac{1}{2}} = \left[\sum_{j=j}^{+\infty} \sum_{k=-\infty}^{+\infty} |\alpha(k,j)|^2 \right]^{\frac{1}{2}}. \quad (2.52)$$

In order to prove the theorem we show that if the function $\phi(x)$ satisfies conditions (2.48), (2.49) and (2.50) then $\psi(x)$ satisfies conditions (2.43), (2.44) and (2.45). We then apply property (2.46) to finish the proof.

It follows from (2.48) that the function $H(\omega)$ defined by (2.13) and (2.14) verifies :

$$H(\omega) = \sum_{k=-\infty}^{\infty} \beta_k e^{ik\omega} \quad \text{and} \quad \exists C_0 > 0 \quad \text{such that} \quad \beta_k \leq C_0 (1+k)^{-3-q} . \quad (2.53)$$

The function $G(\omega)$ defined in (2.41) can be written

$$G(\omega) = e^{-i\alpha} \sum_{k=-\infty}^{\infty} \gamma_k e^{ik\omega} , \quad \text{where} \quad \gamma_k = \beta_{-k-1} (-1)^{-k-1} .$$

The wavelet $\psi(x)$ is thus given by

$$\frac{1}{2} \psi\left(\frac{x}{2}\right) = e^{-i\alpha} \sum_{k=-\infty}^{+\infty} \beta_{-k-1} (-1)^{-k-1} \phi(x-k) .$$

With the above expression and equations (2.48), (2.50) and (2.53) we can then derive (2.43) and (2.45).

Equations (2.48) and (2.49) imply that $\hat{\phi}(\omega) \in \mathbf{C}^{q+1}$ and

$$\frac{d^n \hat{\phi}(0)}{d\omega^n} = 0 \quad \text{for} \quad 1 \leq n \leq q+1 .$$

From (2.34) and (2.42) it thus follows that $\frac{d^n \hat{\psi}(0)}{d\omega^n} = 0$ for $0 \leq n \leq q$, which implies (2.44).

We can now finish the proof of this theorem by applying property (2.46). Let $\alpha_j = \sum_{k=-\infty}^{+\infty} |\alpha(k,j)|^2$. Equation (2.52) yields

$$\sum_{j=J}^{+\infty} \alpha_j = 2^{-2sJ} \varepsilon'_J^2 .$$

So, $\alpha_J = 2^{-2sJ} (\varepsilon'_J^2 - \varepsilon'_{J+1}^2 2^{-2s})$ and therefore

$$\sum_{j=-\infty}^{+\infty} \alpha_j 2^{2js} = (1 - 2^{-2s}) \sum_{j=-\infty}^{+\infty} \varepsilon'_j^2 .$$

The right-hand side statement of property (2.46) is thus equivalent to the right-hand side statement of (2.51). This concludes the proof of the theorem.

2.6. Separable extension of wavelet orthonormal bases in $L^2(\mathbb{R}^2)$

This extension is a particular case of the n-dimensional extension of Y. Meyer [36]. In two dimensions, a multiresolution approximation of $L^2(\mathbb{R}^2)$ is a sequence of subspaces of $L^2(\mathbb{R}^2)$ $\left[\mathbf{V}_j \right]_{j \in \mathbb{Z}}$ which satisfy a straightforward two-dimensional extension of properties (2.1) to (2.5). Such a two-dimensional multiresolution approximation can be defined from the tensor product of a one-dimensional multiresolution vector space sequence. Let $\left[\mathbf{V}_j^1 \right]_{j \in \mathbb{Z}}$ be a multiresolution approximation of $L^2(\mathbb{R})$. Let \mathbf{V}_j^2 be the subspace of $L^2(\mathbb{R}^2)$ defined by

$$\mathbf{V}_j^2 = \mathbf{V}_j^1 \otimes \mathbf{V}_j^1.$$

One can easily show that $\left[\mathbf{V}_j^2 \right]_{j \in \mathbb{Z}}$ is a multiresolution approximation of $L^2(\mathbb{R}^2)$. Since $\left[\mathbf{V}_j^1 \right]_{j \in \mathbb{Z}}$ is a multiresolution approximation of $L^2(\mathbb{R})$, we saw in paragraph 1.2.2 that there exists a unique scaling function $\phi(x)$ such that $\left[\sqrt{2^j} \phi(2^j x - n) \right]_{n \in \mathbb{Z}}$ is an orthonormal basis of \mathbf{V}_j^1 . Let $\Phi(x, y) = \phi(x)\phi(y)$. It is clear that $\left[2^j \Phi(2^j x - n, 2^j y - m) \right]_{(n,m) \in \mathbb{Z}^2}$ is an orthonormal basis of \mathbf{V}_j^2 . Let \mathbf{O}_j^1 be the orthogonal complement of \mathbf{V}_j^1 in \mathbf{V}_{j+1}^1 . We saw that there exist a wavelet $\psi(x)$ such that $\left[\sqrt{2^j} \psi(2^j x - n) \right]_{n \in \mathbb{Z}}$ is an orthonormal basis of \mathbf{O}_j^1 . Let us now define the orthogonal complement \mathbf{O}_j^2 of \mathbf{V}_j^2 in \mathbf{V}_{j+1}^2 from the vector spaces \mathbf{V}_j^1 and \mathbf{O}_j^1 .

$$\mathbf{V}_{j+1}^2 = \mathbf{V}_{j+1}^1 \otimes \mathbf{V}_{j+1}^1 = (\mathbf{O}_j^1 \oplus \mathbf{V}_j^1) \otimes (\mathbf{O}_j^1 \oplus \mathbf{V}_j^1) \text{ hence } \quad (2.54)$$

$$\mathbf{V}_{j+1}^2 = (\mathbf{V}_j^1 \otimes \mathbf{V}_j^1) \oplus (\mathbf{V}_j^1 \otimes \mathbf{O}_j^1) \oplus (\mathbf{O}_j^1 \otimes \mathbf{V}_j^1) \oplus (\mathbf{O}_j^1 \otimes \mathbf{O}_j^1).$$

The vector space \mathbf{O}_j^2 can thus be decomposed into

$$\mathbf{O}_j^2 = (\mathbf{V}_j^1 \otimes \mathbf{O}_j^1) \oplus (\mathbf{O}_j^1 \otimes \mathbf{V}_j^1) \oplus (\mathbf{O}_j^1 \otimes \mathbf{O}_j^1), \quad (2.55)$$

where $\mathbf{V}_j^1 \otimes \mathbf{O}_j^1$, $\mathbf{O}_j^1 \otimes \mathbf{V}_j^1$ and $\mathbf{O}_j^1 \otimes \mathbf{O}_j^1$ are three orthogonal vector spaces.

$$\text{Let } \Psi_1(x, y) = \phi(x)\psi(y), \quad \Psi_2(x, y) = \psi(x)\phi(y), \quad \Psi_3(x, y) = \psi(x)\psi(y).$$

Since $\left[\sqrt{2^j} \phi(2^j x - n) \right]_{n \in \mathbb{Z}}$ and $\left[\sqrt{2^j} \psi(2^j x - n) \right]_{n \in \mathbb{Z}}$ are orthonormal bases, respectively, of \mathbf{V}_j^1 and \mathbf{O}_j^1 , we can derive from equation (2.55) that

$$\left\{ \begin{array}{l} 2^j \Psi_1(2^j x - n, 2^j y - m) \\ 2^j \Psi_2(2^j x - n, 2^j y - m) \\ 2^j \Psi_3(2^j x - n, 2^j y - m) \end{array} \right\}_{(n,m) \in \mathbb{Z}^2}$$

is an orthonormal basis of \mathbf{O}_j^2 . Since

$$\bigcup_{j=-\infty}^{+\infty} \mathbf{V}_j^2 \text{ is dense in } \mathbf{L}^2(\mathbf{R}^2) \quad \text{and} \quad \bigcap_{j=-\infty}^{+\infty} \mathbf{V}_j^2 = \{0\},$$

$$\text{we have } \bigoplus_{j=-\infty}^{+\infty} \mathbf{O}_j^2 = \mathbf{L}^2(\mathbf{R}^2).$$

This implies that

$$\left\{ \begin{array}{l} 2^j \Psi_1(2^j x - n, 2^j y - m) \\ 2^j \Psi_2(2^j x - n, 2^j y - m) \\ 2^j \Psi_3(2^j x - n, 2^j y - m) \end{array} \right\}_{(n,m,j) \in \mathbb{Z}^3}$$

is an orthonormal basis of $\mathbf{L}^2(\mathbf{R}^2)$. This concludes the proof of the theorem 1.4 stated in chapter 1.

CHAPTER 3

DYADIC WAVELET ENERGY ZERO-CROSSINGS

3.1. Introduction

In chapter 1, we saw that the orthogonal wavelet representation is difficult to use for pattern recognition applications because it does not translate when the signal translates. We have shown in equation (1.27) that the decomposition of a function $f(x)$ in a wavelet orthonormal basis could also be interpreted as a uniform sampling of $W^j f(x) = f * \tilde{\psi}^j(x)$ at a rate 2^j for all resolutions 2^j . When $f(x)$ is translated, $W^j f(x)$ is also translated but the uniform sampling of $W^j f(x)$ does not translate. In this chapter we extend the operator W^j to a larger class of wavelets $\psi(x)$ called dyadic wavelets. The operator W^j is called a dyadic wavelet transform and can be viewed as a discretization along the scale axis of the continuous wavelet transform defined by J. Morlet and A. Grossmann [16]. We study the properties of the operator W^j and introduce a new discrete representation based on the zero-crossings and local energy values of this operator [31]. This new representation does translate when the signal translates. For any wavelet which is the second derivative of a smoothing function, the zero-crossings of a dyadic wavelet decomposition provide the location of the signal edges. We study the properties of this Energy Zero-Crossing representation and show that it is well adapted to pattern recognition applications. We show in particular that one can reconstruct a signal from the zero-crossings and local energy values of the dyadic wavelet transform. In order to compute an Energy Zero-Crossing representation of a function, we must first compute its dyadic wavelet transform. We describe a pyramidal algorithm of complexity $n \log(n)$ to compute a dyadic wavelet transform, and then show how to derive the Energy Zero-Crossing representation. We also detail the implementation of a recursive algorithm which reconstructs the original signal from the zero-crossings and local energy values of the dyadic wavelet transform. To illustrate

the application of this representation in pattern matching, we have developed a stereo matching algorithm for one-dimensional signals. We extend this representation to two dimensions and show that it introduces a spatial orientation selectivity. In the last paragraph, we discuss the applications of a two-dimensional Energy Zero-Crossing representation to image segmentation and pattern matching in general.

3.2. Dyadic Wavelet transform

3.2.1. Smoothing functions and dyadic wavelets

In this paragraph, we introduce the dyadic wavelet transform as a transform which decomposes a continuous signal into a sum of details appearing at the scales $(2^j)_{j \in \mathbb{Z}}$. The dyadic wavelet transform is a discretization along the scale axis of the continuous wavelet transform studied by J. Morlet and A. Grossmann [16].

Let S^j be the operator which smooths at the scale 2^j any function $f(x) \in L^2(\mathbb{R})$. This operator convolves $f(x)$ with a function $\theta^j(x) = 2^j \theta(2^j x)$:

$$S^j f(x) = f * \theta^j(x) . \quad (3.1)$$

The function $\theta(x)$ is called a smoothing function. Let us first study the properties of the operator S^j and of the corresponding smoothing function $\theta(x)$. We show afterwards how to define the details of a function $f(x)$ at the scale 2^j from this operator. For normalization purposes we impose the requirement that

$$\|\theta\| = 1 . \quad (3.2)$$

A smoothing operation must gradually attenuate the details of a function as the scale decreases. From $S^{j+1}f$ we should be able to compute $S^j f$ with an additional smoothing. Let $\hat{S}^j f(\omega)$ and $\hat{S}^{j+1} f(\omega)$ be respectively the Fourier transform of $S^j f(x)$ and $S^{j+1} f(x)$. This property is satisfied if and only if

$$\forall \omega \in \mathbb{R} , \quad |\hat{S}^j f(\omega)| \leq |\hat{S}^{j+1} f(\omega)| . \quad (3.3)$$

Since $\hat{S}^j f(\omega) = \hat{f}(\omega) \hat{\theta}(2^{-j} \omega)$ and $\hat{S}^{j+1} f(\omega) = \hat{f}(\omega) \hat{\theta}(2^{-j-1} \omega)$, equation (3.3) implies that there exists a function $U(\omega)$ such that

$$\hat{\theta}(2\omega) = U(\omega)\hat{\theta}(\omega) \quad \text{and} \quad \forall \omega \in \mathbb{R} \quad |U(\omega)| \leq 1 . \quad (3.4)$$

The Fourier transform of $S^j f(x)$ and $S^{j+1} f(x)$ are thus related by

$$\hat{S}^j f(\omega) = U(2^{-j-1}\omega) \hat{S}^{j+1} f(\omega) . \quad (3.5)$$

$U(2^{-j-1}\omega)$ is the additional smoothing which is needed in order to go from the scale 2^{j+1} to the scale 2^j . Equation (3.5) shows that the Fourier transform of a smoothing function can be expressed in terms of $U(\omega)$:

$$\hat{\theta}(\omega) = \prod_{p=1}^{+\infty} U(2^{-p}\omega) . \quad (3.6)$$

As the scale increases to plus infinity we expect that the operator S^j attenuates less the function details and that $S^j f(x)$ converges to $f(x)$ in $L^2(\mathbb{R})$. Conversely as the scale decreases to zero, S^j smooths more the signal details and we expect that the resulting signal ultimately converges to zero. One can easily show that these constraints are equivalent to the following conditions on the Fourier transform of $\theta(x)$:

$$\lim_{|\omega| \rightarrow 0} \hat{\theta}(\omega) = 1 \quad \text{and} \quad (3.7)$$

$$\lim_{|\omega| \rightarrow +\infty} \hat{\theta}(\omega) = 0 . \quad (3.8)$$

Fig. 3.1 shows an example of smoothing function with its Fourier transform. A smoothing operation does not imply any loss of information about the original signal $f(x)$. If the Fourier transform of the smoothing function does not have any zero, it is theoretically possible to reconstruct $f(x)$ from $S^j f(x)$ with a deconvolution. However, such a deconvolution procedure is unstable. This shows clearly the difference between the operator A^j defined in the first chapter and the operator S^j . Indeed, when computing the approximation of a function $f(x)$ at the resolution 2^j with the operator A^j , we loose some information about $f(x)$. This information corresponds to the orthogonal projection of $f(x)$ on the orthogonal complement of V_j in $L^2(\mathbb{R})$.

To extract the details which appear in $S^{j+1} f(x)$ but have been attenuated in $S^j f(x)$ we introduce the function $\psi(x) \in L^2(\mathbb{R})$ whose Fourier transform is given by

$$|\hat{\psi}(\omega)|^2 = |\hat{\theta}(\frac{\omega}{2})|^2 - |\hat{\theta}(\omega)|^2 . \quad (3.9)$$

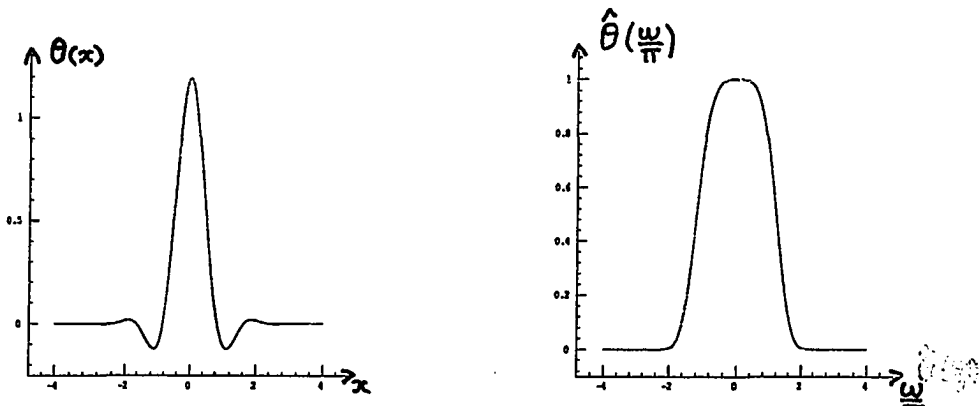


Fig. 3.1. The left and right figures are, respectively, the graph of a smoothing function $\theta(x)$ and its Fourier transform $\hat{\theta}(\frac{\omega}{\pi})$. $\theta(x)$ is a low pass filter.

The function $\psi(x)$ is called a **dyadic wavelet**. This definition was initially suggested by Philippe Tchamitchian. By integrating equation (3.9) on ω between $-\infty$ and $+\infty$ and applying Parseval's theorem, we can show that $\|\psi\| = \|\theta\| = 1$. Since any smoothing function satisfies $\hat{\theta}(\omega) = U(\frac{\omega}{2}) \hat{\theta}(\frac{\omega}{2})$, the Fourier transform of a wavelet can also be written

$$\hat{\psi}(2\omega) = G(\omega) \hat{\theta}(\omega) \quad \text{where} \quad |U(\omega)|^2 + |G(\omega)|^2 = 1. \quad (3.10)$$

With a simple summation on equation (3.9) we can show also that

$$\sum_{j=-J}^J |\hat{\psi}(2^j \omega)|^2 = |\hat{\theta}(2^{-J-1}\omega)|^2 - |\hat{\theta}(2^J \omega)|^2. \quad (3.11)$$

By taking the limit of (3.11) as J tends to $+\infty$ and applying the properties (3.7) and (3.8) of a smoothing function, we have

$$\lim_{J \rightarrow +\infty} \sum_{j=-J}^J |\hat{\psi}(2^j \omega)|^2 = \sum_{j \in \mathbb{Z}} |\hat{\psi}(2^j \omega)|^2 = 1. \quad (3.12)$$

This convergence is clearly uniform for $|\omega| > 1$. Theorem 3.1 shows that this property is a characterization of a dyadic wavelet.

Theorem 3.1

Any function $\psi(x) \in L^2(\mathbb{R})$ such that $\|\psi\| = 1$ is a wavelet function if and only if

$$\forall \omega \in \mathbb{R} \quad \lim_{J \rightarrow +\infty} \sum_{j=-J}^J |\hat{\psi}(2^j \omega)|^2 = 1 \quad , \quad \text{and the convergence is uniform for } |\omega| \geq 1 .$$

The proof of this theorem is given in appendix B. Fig. 3.2 shows the wavelet associated with the smoothing function in Fig. 3.1. These particular functions are further described in paragraph 3.5.1.1. One can easily show that an orthogonal wavelet as defined by theorem 1.3 verifies the conditions of theorem 3.1. Any orthogonal wavelet is thus also a dyadic wavelet.

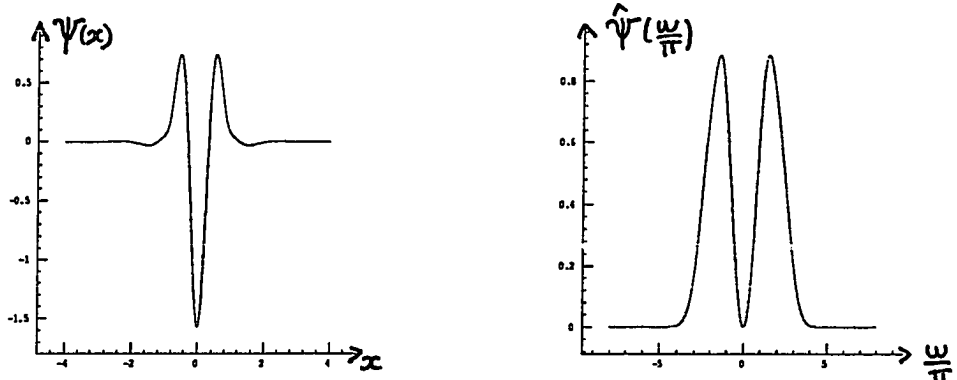


Fig. 3.2. The left and right figures are, respectively, the graph of a wavelet $\psi(x)$ and the absolute value of its Fourier transform $|\hat{\psi}(\frac{\omega}{\pi})|$. $\psi(x)$ is a band pass filter.

Given a wavelet $\psi(x)$, we call the wavelet transform at the scale 2^j of $f(x) \in L^2(\mathbb{R})$

$$W^j f(x) = f * \psi^j(x) . \quad (3.13)$$

The wavelet transform of $f(x)$ at the scale 2^j provides the details of $f(x)$ which have been attenuated between the scales 2^{j+1} and 2^j . The energy of these details are equal to the difference of the energies of $S^j f$ and $S^{j+1} f$:

$$\|W^j f\| = \|S^{j+1} f\| - \|S^j f\| . \quad (3.14)$$

Proof of equation (3.14) : We can derive from equation (3.9) that

$$|\hat{f}(\omega)|^2 |\hat{\psi}(2^{-j}\omega)|^2 = |\hat{f}(\omega)|^2 |\theta(2^{j-1}\omega)|^2 - |f(\omega)|^2 |\theta(2^{-j}\omega)|^2 . \quad (3.15)$$

By integrating equation (3.15) between $-\infty$ and $+\infty$ and applying Parseval's theorem we get equation (3.14).

3.2.2. Infinite dyadic wavelet transform

We call the **Infinite Dyadic Wavelet Transform** of $f(x)$, the sequence of functions

$$\mathbf{W}_I f = \left[W^j f(x) \right]_{j \in \mathbb{Z}} . \quad (3.16)$$

Such a transform decomposes a function into its details which appear at all the scales $(2^j)_{j \in \mathbb{Z}}$. In this paragraph, we study the most important properties of this transform.

• Translation property

Let $f(x) \in L^2(\mathbb{R})$ and $g(x) = f(x-\tau)$ be a translation of $f(x)$ by τ . Since the convolution product is translating,

$$W^j g(x) = W^j f(x-\tau) . \quad (3.17)$$

The wavelet transform of $g(x)$ is equal to the wavelet transform of $f(x)$ translated by τ .

• Completeness of the wavelet representation

A function can be reconstructed from its wavelet representation.

$$f(x) = \sum_{j=-\infty}^{+\infty} W^j f(x) * \tilde{\psi}^j(x) = \mathbf{W}_I^{-1} \left[W^j f(x) \right]_{j \in \mathbb{Z}} . \quad (3.18)$$

The inverse wavelet transform operator \mathbf{W}_I^{-1} is characterized by equation (3.18).

Proof : By multiplying equation (3.12) by $\hat{f}(\omega)$ we get

$$\hat{f}(\omega) = \sum_{j \in \mathbb{Z}} \hat{f}(\omega) |\hat{\psi}(2^j \omega)|^2 .$$

This expression is the Fourier transform of equation (3.18).

• Energy conservation

The total energy of a signal can be decomposed into a sum of the energies of the details

appearing at each scale 2^j . This energy conservation is a discretization of the energy conservation formula of A. Grossmann and J. Morlet [16].

$$\|f(x)\|^2 = \sum_{j=-\infty}^{+\infty} \|W^j f(x)\|^2 . \quad (3.19)$$

Proof: If we multiply equation (3.12) by $|\hat{f}(\omega)|^2$ we get

$$|\hat{f}(\omega)|^2 = \sum_{j \in \mathbb{Z}} |\hat{f}(\omega)|^2 |\hat{\psi}(2^j \omega)|^2 .$$

By integrating this equation between $+\infty$ and $-\infty$ we obtain equation (3.19). This energy conservation equation is similar to the energy conservation equation derived by A. Grossmann and J. Morlet [16] for a continuous wavelet transform.

• Continuity and dyadic wavelet transform space

Let \mathbf{I} be the subspace of $(L^2(\mathbb{R}))^\mathbb{Z}$ of all the wavelet transforms $W_I f = [W^j f(x)]_{j \in \mathbb{Z}}$, for $f(x) \in L^2(\mathbb{R})$. We saw that W_I admits an inverse W_I^{-1} which is characterized by equation (3.18); it is thus an isomorphism from $L^2(\mathbb{R})$ onto \mathbf{I} . The energy conservation equation shows that this isomorphism is isometric. The operators W_I and W_I^{-1} are therefore continuous.

To characterize the vector space \mathbf{I} , we build a projection operator P_I from $(L^2(\mathbb{R}))^\mathbb{Z}$ to \mathbf{I} . This projection operator is defined from the wavelet transform W_I and the inverse wavelet transform W_I^{-1} . We saw that the inverse wavelet transform W_I^{-1} was characterized by equation (3.18) for any element of \mathbf{I} . Let us extend W_I^{-1} to the entire space $(L^2(\mathbb{R}))^\mathbb{Z}$:

$$\forall \left[g_j(x) \right]_{j \in \mathbb{Z}} \in (L^2(\mathbb{R}))^\mathbb{Z} \quad W_I^{-1} \left[g_j(x) \right]_{j \in \mathbb{Z}} = \sum_{j \in \mathbb{Z}} g_j * \hat{\psi}^j(x) . \quad (3.20)$$

One can easily show that $W_I^{-1} \left[g_j \right]_{j \in \mathbb{Z}} \in L^2(\mathbb{R})$. We can now characterize the vector space \mathbf{I} with the projection operator P_I defined by

$$P_I = W_I \circ W_I^{-1} . \quad (3.21)$$

$$(L^2(\mathbb{R}))^\mathbb{Z} \xrightarrow{W_I^{-1}} L^2(\mathbb{R}) \xrightarrow{W_I} \mathbf{I} .$$

This operator clearly satisfies the conditions of a projection operator from $(L^2(\mathbb{R}))^\mathbb{Z}$ on \mathbf{I} :

$$\forall \left[g_j(x) \right]_{j \in \mathbb{Z}} \in (\mathbf{L}^2(\mathbb{R}))^{\mathbb{Z}} , \quad P_I \left[g_j(x) \right]_{j \in \mathbb{Z}} \in \mathbf{I} \quad \text{and} \quad (3.22)$$

$$\left[g_j(x) \right]_{j \in \mathbb{Z}} \in \mathbf{I} \quad \text{if and only if} \quad P_I \left[g_j(x) \right]_{j \in \mathbb{Z}} = \left[g_j(x) \right]_{j \in \mathbb{Z}} . \quad (3.23)$$

By inserting in equation (3.21) the definition of \mathbf{W}_I and \mathbf{W}_I^{-1} given by equations (3.13) and (3.18), we obtain

$$P_I \left[g_j(x) \right]_{j \in \mathbb{Z}} = \left[\sum_{k=-\infty}^{+\infty} K_{j,k} * g_k(x) \right]_{j \in \mathbb{Z}} \quad \text{where} \quad K_{j,k}(x) = \psi^j * \bar{\psi}^k(x) . \quad (3.24)$$

As a consequence of equation (3.23), for any wavelet transform $\mathbf{W}_I f = [W^j]_{j \in \mathbb{Z}}$ we have in particular

$$\forall j \in \mathbb{Z} , \quad W^j f(x) = \sum_{k=-\infty}^{+\infty} K_{j,k} * W^k f(x) . \quad (3.25)$$

This equation expresses the redundancy between the wavelet transforms at different scales. The functions $K_{j,k}(x)$ are called reproducing kernels. The application of reproducing kernels to wavelet transforms was introduced by A. Grossmann and J. Morlet [15]. The correlation of the wavelet transforms $W^k f(x)$ and $W^j f(x)$ is given by the energy of the reproducing kernel $K_{j,k}(x)$.

As explained in chapter 1, in practice a measuring device does not precisely measure a continuous signal but only an approximation at a finite resolution. In the next paragraph, we show how to apply the multiresolution approximation model in order to define a finite dyadic wavelet transform.

3.2.3. Finite Dyadic Wavelet Transform

3.2.3.1. Finite resolution approximation

We saw in chapter 1 that the concept of multiresolution could be defined with respect to a sequence of vector spaces $\left[\mathbf{V}_j \right]_{j \in \mathbb{Z}}$, called a multiresolution approximation of $\mathbf{L}^2(\mathbb{R})$. The approximation of a function $f(x)$ at the resolution 2^j is then defined as the orthogonal projection of $f(x)$ on the vector space \mathbf{V}_j . Theorem 1.1 shows that this multiresolution

approximation is characterized by a unique function $\phi(x)$ called a scaling function. The orthogonal projection operator A^j can thus be expressed in this basis :

$$\forall f(x) \in \bar{L}^2(\mathbb{R}) , A^j f(x) = \sum_{n=-\infty}^{+\infty} 2^{-j} \langle f(u), \phi^j(u - 2^{-j}n) \rangle \phi^j(x - 2^{-j}n) . \quad (3.26)$$

The vector space \mathbf{V}_j of all the functions of $L^2(\mathbb{R})$ approximated at the resolution 2^j is characterized by :

$$\forall f^*(x) \in \mathbf{V}_j , \exists (\alpha_n) \in l^2(\mathbb{Z}) , f^*(x) = \sum_{n=-\infty}^{+\infty} \alpha_n \phi^j(x - 2^{-j}n) . \quad (3.27)$$

In the next lemma we give a condition on the scaling function $\phi(x)$ so that any function approximated at the resolution 2^j can be interpreted as a smoothing at the scale 2^j of some function in $L^2(\mathbb{R})$.

Lemma 3.1

Let $\left[\mathbf{V}_j\right]_{j \in \mathbb{Z}}$ be a multiresolution space sequence and $\phi(x)$ be the associated scaling function. If there exists a function $v(x) \in L^2(\mathbb{R})$ such that

$$\phi(x) = \theta * v(x) \quad \text{with} \quad \hat{v}(\omega) = O\left(\frac{1}{\omega}\right) , \quad \text{then} \quad (3.28)$$

$$\forall f^*(x) \in \mathbf{V}_j , \exists f(x) \in \bar{L}^2(\mathbb{R}) \quad \text{such that} \quad f^* = S^j f . \quad (3.29)$$

The proof of this lemma is given in appendix C. If the scaling function $\phi(x)$ satisfies the condition of the lemma, any approximated function at the resolution 2^j is thus equal to a smoothing at the scale 2^j of some function in $L^2(\mathbb{R})$. The contrary is false. The smoothing at the scale 2^j of any function in $L^2(\mathbb{R})$ is not a priori the approximation at the resolution 2^j of some function in $L^2(\mathbb{R})$. We show in appendix C that a function $f(x) \in \bar{L}^2(\mathbb{R})$ verifies $S^j f(x) \in \mathbf{V}_j$ if and only if

$$\exists (\alpha_n)_{n \in \mathbb{Z}} \in l^2(\mathbb{Z}) , f(x) = \sum_{n=-\infty}^{+\infty} \alpha_n v^j(x - 2^{-j}n) . \quad (3.30)$$

The function $f(x)$ must therefore be in the vector space generated by the family of functions $\left[v^j(x - 2^{-j}n)\right]_{n \in \mathbb{Z}}$; it cannot be an arbitrary function in $L^2(\mathbb{R})$.

In chapter 1, we characterized an approximation $A^j f(x) \in V_j$ with the set of inner products :

$$A^j f_d = \left[\langle f(u), \phi^j(u - 2^{-j}n) \rangle \right]_{n \in \mathbb{Z}} = \left[\langle A^j f(u), \phi^j(u - 2^{-j}n) \rangle \right]_{n \in \mathbb{Z}} .$$

Another convenient characterization of a signal approximated at the resolution 2^j is to sample uniformly this signal at the rate 2^j . The following theorem shows how to reconstruct an approximation $A^j f(x)$ from the set of samples $\left[A^j f(2^{-j}n) \right]_{n \in \mathbb{Z}}$.

Theorem 3.2

If there exists two constants c_1 and c_2 such that $c_1 \leq \sum_{n=-\infty}^{+\infty} \hat{\phi}(\omega + 2n\pi) \leq c_2$, then any function $f(x) \in V_j$ can be decomposed into

$$f(x) = \sum_{n=-\infty}^{+\infty} f(2^{-j}n) 2^{-j} \rho^j(x - 2^{-j}n) . \quad (3.31)$$

The spline function $\rho(x)$ is unique and its Fourier transform is given by

$$\hat{\rho}(\omega) = \frac{\hat{\phi}(\omega)}{\sum_{n=-\infty}^{+\infty} \hat{\phi}(\omega + 2n\pi)} . \quad (3.32)$$

The proof of this theorem is detailed in appendix D. In this chapter, we characterize a signal approximated at the resolution 2^j by providing a uniform sampling of this signal.

Let us suppose that we have been able to approximate a function $f(x)$ at the resolution 2^{j_2} . This approximation $A^{j_2} f(x)$ does not contain any information on the details of the function which are smaller than 2^{-j_2} . It would thus be absurd to try to compute the wavelet transform of this approximated function for any scale bigger than 2^{j_2} . In the next paragraph we study a finite dyadic wavelet transform of such an approximated function.

3.2.3.2. Definition and properties of a finite dyadic wavelet transform

In this paragraph, we suppose that we can only recover an approximation of the original function at the resolution 2^{j_2} . The resolution 2^{j_2} can be viewed as the maximum resolution of our measuring device. We also suppose that the scaling function $\phi(x)$ satisfies the condition of lemma 2. The approximation at the resolution 2^{j_2} of any function $f^*(x) \in \mathbf{V}_{j_2}$ can thus be interpreted as a smoothing at the scale 2^{j_2} of some function $f(x) \in \mathbf{L}^2(\mathbb{R})$: $f^*(x) = S^{j_2}f(x)$. We want to emphasize once more that the contrary is not true. From now on, we denote by $f^*(x) = S^{j_2}f(x) \in \mathbf{V}_{j_2}$ any approximated function at the resolution 2^{j_2} . The incremental smoothing property (6) of the smoothing operation implies that from $S^{j_2}f(x)$ we can compute the wavelet transform of $f(x)$ at any smaller scale 2^j , $j < j_2$. In practical computations we must, however, stop the wavelet decomposition at some finite resolution 2^{j_1} .

We call the finite dyadic wavelet transform between the scale 2^{j_2} and 2^{j_1} the operator \mathbf{W}_F which transforms any function $S^{j_2}f \in \mathbf{V}_{j_2}$ into the set of functions

$$\mathbf{W}_F(S^{j_2}f) = \left\{ \left[W_j f(x) \right]_{j_1 \leq j < j_2}, S^{j_1}f(x) \right\}. \quad (3.33)$$

It provides a smoothing of the signal $f(x)$ at a coarse scale 2^{j_1} plus the successive details which appear between the scales 2^{j_1} and 2^{j_2} . Let $(\mathbf{L}^2(\mathbb{R}))^{j_2-j_1}$ be the set of finite sequences of $\mathbf{L}^2(\mathbb{R})$ functions $\left[g_j(x) \right]_{j_1-1 \leq j < j_2}$. The operator \mathbf{W}_F transforms any approximated signal $f^*(x) = S^{j_2}f \in \mathbf{V}_{j_2}$ into an element of $(\mathbf{L}^2(\mathbb{R}))^{j_2-j_1}$.

• Computation of a finite dyadic wavelet transform

We describe a simple pyramidal algorithm to compute a finite dyadic wavelet transform for any approximated signal $S^{j_2}f \in \mathbf{V}_{j_2}$. We saw in paragraph 3.2.1 that the Fourier transform of a smoothing function and its associated wavelet satisfy

$$\hat{\theta}(\omega) = U\left(\frac{\omega}{2}\right) \hat{\theta}\left(\frac{\omega}{2}\right) \quad \text{and} \quad \hat{\psi}(\omega) = G\left(\frac{\omega}{2}\right) \hat{\theta}\left(\frac{\omega}{2}\right).$$

In equation (3.5), we saw that the Fourier transform of $S^{j+1}f(x)$ and $S^j f(x)$ are related by

$$\hat{S}^j f(\omega) = U(2^{-j-1}\omega) \hat{S}^{j+1} f(\omega). \quad (3.34)$$

Similarly we can show that the Fourier transform of $S^{j+1}f(x)$ and $W^jf(x)$ are related by

$$\hat{W}^jf(\omega) = G(2^{-j-1}\omega) \hat{S}^{j+1}f(\omega) . \quad (3.35)$$

Since $|U(\omega)| \leq 1$ and $|G(\omega)| \leq 1$, we can define their inverse Fourier transform in the sense of Schwartz distributions. Let u^j and g^j be the inverse Fourier transforms of $U(2^{-j}\omega)$ and $G(2^{-j}\omega)$, equations (3.34) and (3.35) yield

$$S^jf(x) = S^{j+1}f * u^{j+1} \quad \text{and} \quad (3.36)$$

$$W^jf(x) = S^{j+1}f * g^{j+1} . \quad (3.37)$$

By iterating on these two equations with j varying between $j_2 - 1$ and j_1 , we can compute the finite dyadic wavelet transform of $S^{j_2}f(x)$.

In all the examples which are shown, we suppose that the input signal was measured at the resolution 1. The maximum scale 2^{j_2} of the finite dyadic wavelet transforms is therefore equal to 1 ($j_2=0$). Fig. 3.3 shows an example of a signal approximated at the resolution 1, and Fig. 3.4 gives a finite dyadic wavelet decomposition between the scales 1 and 2^{-5} ($j_1=-5$). This wavelet decomposition was computed with the wavelet and the smoothing function shown in Fig. 3.1 and 3.2.

• Inverse finite wavelet transform

A finite dyadic wavelet transform is complete. We can reconstruct $f^* = S^{j_2}f \in \mathbf{V}_{j_2}$ from its finite wavelet transform

$$\mathbf{W}_F(S^{j_2}f) = \left\{ \left[W^jf(x) \right]_{j_1 \leq j < j_2}, S^{j_1}f(x) \right\} .$$

The inverse finite wavelet transform can also be implemented with a simple pyramidal algorithm. Let $\bar{U}(\omega)$ and $\bar{G}(\omega)$ be, respectively, the complex conjugates of $U(\omega)$ and $G(\omega)$. Equations (3.34) and (3.35) yield

$$\bar{U}(2^{-j-1}\omega) \hat{S}^jf(\omega) + \bar{G}(2^{-j-1}\omega) \hat{W}^jf(\omega) = (|U(2^{-j-1}\omega)|^2 + |G(2^{-j-1}\omega)|^2) \hat{S}^{j+1}f(\omega) .$$

Since $|U(\omega)|^2 + |G(\omega)|^2 = 1$,

$$\bar{U}(2^{-j-1}\omega) \hat{S}^jf(\omega) + \bar{G}(2^{-j-1}\omega) \hat{W}^jf(\omega) = \hat{S}^{j+1}f(\omega) . \quad (3.38)$$

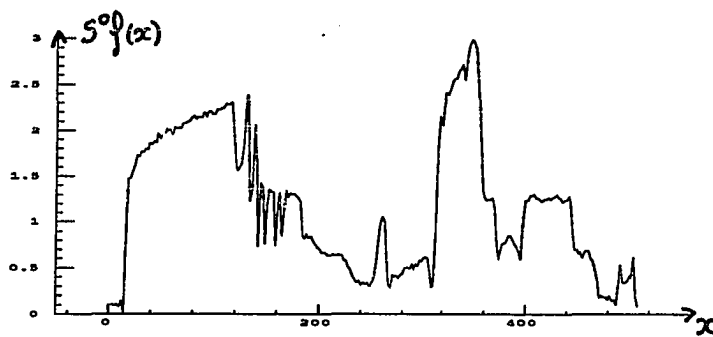


Fig. 3.3. Original signal measured at the resolution $1 : S^0f(x)$.

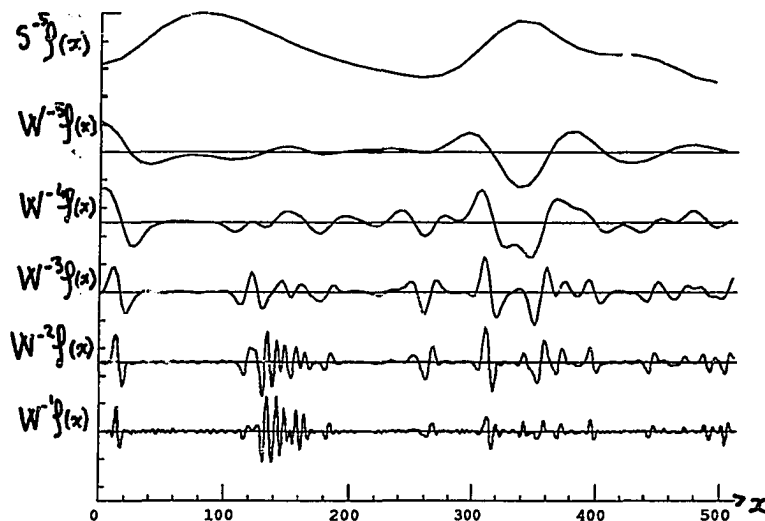


Fig. 3.4. Dyadic wavelet representation of the signal shown in Fig. 3.3. The signal was decomposed between the scales 1 and 2^{-5} . The signal at the top is a smoothing transform of the original signal at the scale $2^{-5} : S^{-5}f(x)$. The other curves correspond to the wavelet transform $W^j f(x)$ for $0 > j \geq -5$.

Let \bar{h}^j and \bar{g}^j be respectively the reflections of u^j and g^j . The inverse Fourier transform of equation (3.38) can be written

$$\bar{h}^{j+1} * S^j f(x) + \bar{g}^{j+1} * W^j f(x) = S^{j+1} f(x) . \quad (3.39)$$

By iterating on this equation for j varying between j_1 and $j_2 - 1$, we can thus reconstruct $S^{j_2} f(x)$ from its finite dyadic wavelet transform. This algorithm is a characterization of the

inverse finite dyadic wavelet transform operator W_F^{-1} .

• Energy conservation

For a finite dyadic wavelet transform also, there is a simple energy conservation property given by

$$\|S^{j_2}f(x)\|^2 = \sum_{j=j_1}^{j_2-1} \|W^j f(x)\|^2 + \|S^{j_1}f(x)\|^2. \quad (3.40)$$

This equation can be derived by iterating on equation (3.14), with j varying between j_1 and $j_2 - 1$.

• Continuity and finite wavelet transform space

Let \mathbf{F} be the subspace of $(L^2(\mathbb{R}))^{j_2-j_1}$ of the finite wavelet transforms of all the functions in \mathbf{V}_{j_2} . The energy conservation equation shows that the operator W_F is an isometric isomorphism from \mathbf{V}_{j_2} onto \mathbf{F} . The operators W_F and W_F^{-1} are thus continuous.

As in the infinite case, we characterize the vector space \mathbf{F} with a projection operator from $(L^2(\mathbb{R}))^{j_2-j_1}$ on \mathbf{F} . This projector operator is also defined from the wavelet transform W_F and the inverse wavelet transform W_F^{-1} . The inverse wavelet transform W_F^{-1} is defined on any finite wavelet transform by iterating on equation (3.39). This operator can also be extended to any sequence of functions in the space $(L^2(\mathbb{R}))^{j_2-j_1}$. The extension of W_F^{-1} transforms any sequence $[f_j]_{j_1-1 \leq j < j_2} \in (L^2(\mathbb{R}))^{j_2-j_1}$ into a function $f(x) \in L^2(\mathbb{R})$ with the following loop :

$$\begin{cases} \alpha_{j_1-1}(x) = f_{j_1-1}(x) \\ \text{for } j \text{ varying between } j_1-1 \text{ and } j_2-1 : \quad \alpha_{j+1}(x) = \alpha_j * \bar{h}^j(x) + f_j * \bar{g}^j(x) \\ f(x) = \alpha_{j_2}(x) \end{cases}$$

As extended, the range of W_F^{-1} on $(L^2(\mathbb{R}))^{j_2-j_1}$ is a subspace of $L^2(\mathbb{R})$ which includes strictly the vector space \mathbf{V}_{j_2} . In order to get back to the vector space \mathbf{V}_{j_2} we must then apply the operator A^{j_2} , which is an orthogonal projection on \mathbf{V}_{j_2} . Let P_F be the operator defined

by

$$P_F = W_F \circ A^{j_2} \circ W_F^{-1}. \quad (3.41)$$

$$(L^2(\mathbb{R}))^{j_2-j_1} \xrightarrow{W_F^{-1}} L^2(\mathbb{R}) \xrightarrow{A^{j_2}} V_{j_2} \xrightarrow{W_F} F.$$

This operator satisfies the conditions of a projection operator from $(L^2(\mathbb{R}))^{j_2-j_1}$ on F :

$$\forall \left[g_j(x) \right]_{j_1-1 \leq j < j_2} \in (\mathbb{C})^{j_2-j_1}, \quad P_F \left[g_j(x) \right]_{j_1 \leq j < j_2} \in F \quad \text{and}$$

$$\left[g_j(x) \right]_{j_1-1 \leq j < j_2} \in F \quad \text{if and only if} \quad P_F \left[g_j(x) \right]_{j_1-1 \leq j < j_2} = \left[g_j(x) \right]_{j_1-1 \leq j < j_2}.$$

This operator expresses the intrinsic redundancy of a finite dyadic wavelet representation. It is an important tool for analyzing any transform based on a finite dyadic wavelet representation.

The dyadic wavelet representation is a continuous representation which needs to be discretized to be used by computer algorithms. We saw in chapter 1 that if the dyadic wavelet is an orthonormal wavelet, we can build an uncorrelated representation by sampling uniformly the dyadic wavelet representation. The inconvenience of such a sampling is that the derived representation does not translate. In the next paragraph, we define a translating discrete representation from an adaptive sampling of the dyadic wavelet decomposition.

3.3. Energy Zero-Crossings Representation

3.3.1. Adaptive Sampling : Zero-Crossings

A simple adaptive sampling of the functions $\left[W^j f(x) \right]_{j \in \mathbb{Z}}$ consists of recording the positions of the zero-crossings. When $f(x)$ is translated, $W^j f(x)$ is also translated so the position of the zero-crossings are translated as well. If $\psi(x)$ is proportional to the second derivative of a smoothing function $\xi(x)$ scaled by a factor α , any zero-crossing of $W^j f(x)$ can be interpreted as a point of abrupt change in the function $f(x)$ smoothed by $\xi(x)$ at the scale 2^j . Indeed if $\psi(x) = \lambda \xi''(\alpha x)$,

$$W^j f(x) = f * \psi^j(x) = \lambda \alpha^2 2^{2j} (f(u) * \xi(\alpha 2^j u))''(x). \quad (3.42)$$

Hence, a zero-crossing of $W^j f(x)$ corresponds to an inflection point of the function $f(x)$ which had been smoothed by $\xi(x)$ at the scale $\alpha 2^j$. Fig. 3.5 illustrates this on a straight edge. Fig. 3.7 shows the wavelet decomposition of a straight edge between the scale 1 and 2^{-3} . We clearly see that the location of the zero-crossings correspond to the location of the abrupt changes in the original signal shown in Fig. 3.6. In order to be proportional to the second derivative of a smoothing function, the Fourier transform $\hat{\psi}(\omega)$ of the wavelet $\psi(x)$ must satisfy

$$\hat{\psi}(\omega) = -\frac{\lambda}{\alpha} \omega^2 \xi\left(\frac{\omega}{\alpha}\right). \quad (3.43)$$

Since $\xi(x)$ is a smoothing function, $\xi(0)=1$. The Fourier transform $\hat{\psi}(\omega)$ must have a zero of order two at $\omega=0$. The parameters α and λ are adjusted in order to have $\xi(0)=1$ and $\|\xi\|=1$. Fig. 3.8 shows the smoothing function $\xi(x)$ which is proportional to the second derivative of the wavelet shown in Fig. 3.2.

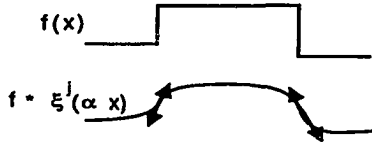


Fig. 3.5 The zero-crossings of a wavelet transform provide the locations of the inflection points (edges) of $(f(u) * \xi(\alpha 2^j u))(x)$.

Several researchers have studied the characterization of a function from properties of zero-crossings [27, 52]. In particular, a large effort has been concentrated on the zero-crossing properties of a function convolved with the Laplacian of a Gaussian [44, 49, 51, 19]. The Laplacian of a Gaussian is not a dyadic wavelet since its Fourier transform does not satisfy the condition of theorem 3.1. These studies, however, give some interesting preliminary results. Let us denote by $\Delta G(x)$ the Laplacian of a normalized Gaussian, and $\Delta G^s(x) = \Delta G(sx)$. R. Hummel [19] has shown that if $f(x) \in L^2(\mathbb{R})$, the zero-crossings of $f * \Delta G^s(x)$, for all $s \in \mathbb{R}$, uniquely characterize the function $f(x)$. This characterization is, however, not stable. A small

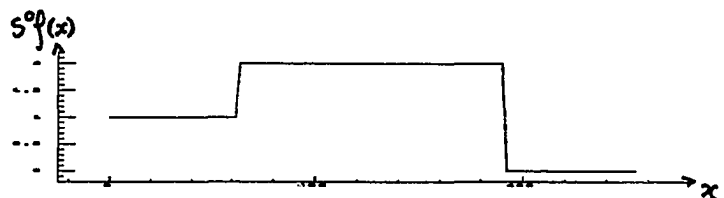


Fig. 3.6. Example of straight edges.

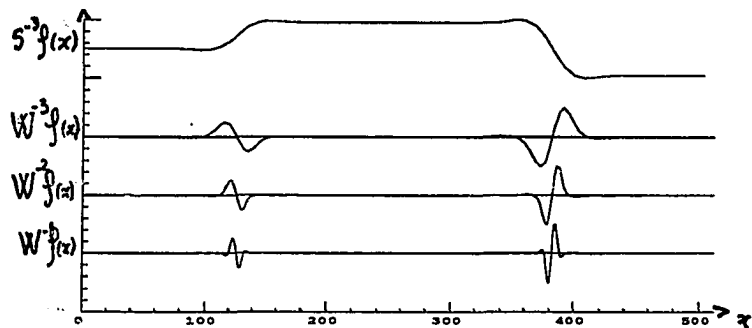


Fig. 3.7. Dyadic wavelet decomposition of straight edges between the scales 1 and 2^{-3} . At each scale, the zero-crossings provide the locations of the edges.

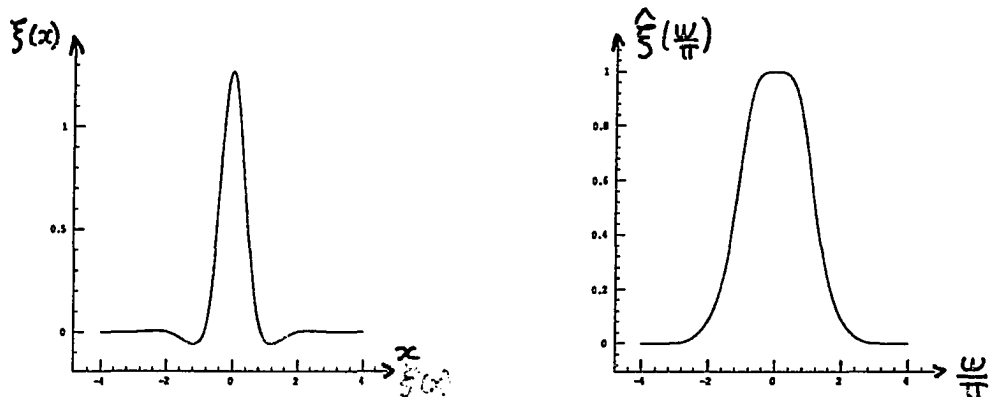


Fig. 3.8. The left and right figures are respectively the graph of the smoothing function $\xi(x)$ and its Fourier transform $\xi(\frac{\omega}{\pi})$. The second derivative of $\xi(x)$ is proportional to the wavelet shown in Fig. 3.2.

perturbation of the zero-crossings may correspond to an arbitrarily large distortion on the function $f(x)$. R. Hummel thus proposed to stabilize the zero-crossing representation by recording the gradient along each zero-crossing. Although the derived representation seems to be stable experimentally [20], it has two disadvantages for pattern recognition applications. The convolution with a Laplacian of Gaussian corresponds to a second derivative operation on the signal. The gradient along each zero-crossing is therefore a third derivative. In practice, the computation of a signal's third derivative is noisy. The second problem is that such a representation admits no simple, natural metric. It is difficult to find a non ad-hoc distance which combines both the values of the gradients and the positions of the zero-crossings. We thus cannot easily compare two signals decomposed with such a transform. In the next paragraph we try to stabilize the zero-crossing representation of a dyadic wavelet transform with a local energy measure. We show that one can easily define a metric within such a representation. As opposed to what has been done previously in the case of a Laplacian of Gaussian, with a dyadic wavelet transform the scale parameter varies only on a discrete dyadic scale $(2^j)_{j \in \mathbb{Z}}$ and not over \mathbb{R} or a uniform sub-lattice of \mathbb{R} . We thus keep much less information about the zero-crossing locations.

3.3.2. Stabilization with local energies

Another way to stabilize a zero-crossing representation is to record the energy of $W^j f(x)$ between two consecutive zero-crossings (see Fig. 3.9). Let (z_{k-1}^j, z_k^j) be two consecutive zero-crossings. The energy e_k^j between z_{k-1}^j and z_k^j is defined by

$$e_k^j = \left[\int_{z_{k-1}^j}^{z_k^j} |W^j f(x)|^2 dx \right]^{\frac{1}{2}} \cdot \text{sign}(W^j f) . \quad (3.44)$$

In the energy e_k^j , we keep the sign of $W^j f(x)$ on the interval $[z_{k-1}^j, z_k^j]$. This energy measures the importance of the structure which appears at the scale 2^j between the two "edges" located in z_{k-1}^j and z_k^j . The sign tells us whether the structure is convex or concave (sign of a second derivative).

We characterize these zero-crossings and local energies with the following operator E . Let $g(x) \in \mathbf{C}$ be a continuous $L^2(\mathbb{R})$ function and let $\{z_n\}_{n \in \mathbb{Z}}$ and $\{e_n\}_{n \in \mathbb{Z}}$ be, respectively, the positions of its zero-crossings and the values of the local energies between each pair of zero-crossings. The zero-crossings and local energies of $g(x)$ are characterized by the piecewise constant function $Eg(x)$ defined by :

$$\forall x \in [z_{n-1}, z_n] , \quad Eg(x) = a_n = \frac{e_n}{\sqrt{z_n - z_{n-1}}} . \quad (3.45)$$

The function $Eg(x)$ has the same zero-crossings as $g(x)$ and has the same local energy between each pair of zero-crossings. We define the operator E on \mathbf{C} and not over the whole space $L^2(\mathbb{R})$ since we cannot define in general the zero-crossings of a function in $L^2(\mathbb{R})$. E is a nonlinear operator from \mathbf{C} to the subspace of $L^2(\mathbb{R})$ of piecewise-constant functions. Since $g(x)$ and $Eg(x)$ have the same local energies, they also have the same global energy :

$$\|Eg\|^2 = \|g\|^2 = \sum_{n \in \mathbb{Z}} |e_n|^2 . \quad (3.46)$$

We denote by E_I the operator which transforms any infinite sequence of continuous functions $\{g_j(x)\} \in (\mathbf{C})^\mathbb{Z}$ into a sequence of piecewise-constant functions defined by $E_I[g_j(x)] = [Eg_j] \in (\mathbf{C})^\mathbb{Z}$.

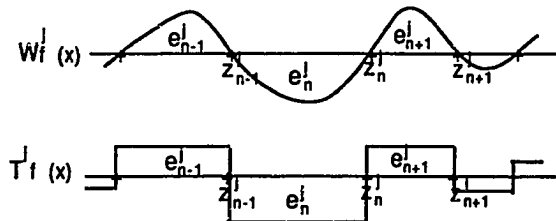


Fig. 3.9. Construction of $T^j f(x)$ from $W^j f(x)$.

At each scale 2^j , the zero-crossings and local energies of $W^j f(x)$ are characterized by the piecewise constant function $T^j f = E(W^j f)$. Fig. 3.9 illustrates this transformation. We call the Infinite Energy Zero-Crossing representation the set of functions

$$\mathbf{T}_I f = \left[T^j f(x) \right]_{j \in \mathbb{Z}} = \left[E(W^j f)(x) \right]_{j \in \mathbb{Z}} . \quad (3.47)$$

The infinite Energy Zero-Crossing representation is a sequence of piecewise constant functions which are characterized by the zero-crossings and energies of the infinite dyadic wavelet transform. The infinite Energy Zero-Crossing transform \mathbf{T}_I can be decomposed into an infinite wavelet transform \mathbf{W}_I followed by the energy zero-crossing detection operator \mathbf{E}_I :

$$\mathbf{T}_I = \mathbf{E}_I \circ \mathbf{W}_I . \quad (3.48)$$

From the computer implementation point of view, at each scale 2^j , $T^j f(x)$ is characterized by the position of its zero-crossings $\left[z_k^j \right]_{k \in \mathbb{Z}}$ and by the value of its amplitudes $\left[a_k^j \right]_{k \in \mathbb{Z}}$ between two zero-crossings. These amplitudes are given by

$$a_k^j = \frac{e_k^j}{\sqrt{z_k^j - z_{k-1}^j}} .$$

The definition of an EZC representation on a finite range of scales 2^j , for $j_1 - 1 \leq j < j_2$, can similarly be derived from the definition of a finite dyadic wavelet representation. Let $S^{j_2} f \in \mathbf{V}_{j_2}$ be an approximated function at the resolution 2^{j_2} . We call the finite Energy Zero-Crossing representation of $S^{j_2} f$ between the scales 2^{j_2} and 2^{j_1} , the sequence of functions

$$\mathbf{T}_F(S^{j_2} f) = \left\{ \left[T^j f(x) \right]_{j_1 \leq j < j_2}, S^{j_1} f(x) \right\} . \quad (3.49)$$

Fig. 3.10 shows the finite EZC representation between the scales 1 and 2^{-5} of the signal shown in Fig. 3. Let $(\mathbf{C})^{j_2-j_1}$ be the set of finite sequences of continuous $L^2(\mathbf{R})$ functions $\left[g_j(x) \right]_{j_1-1 \leq j < j_2}$. Let \mathbf{E}_F denote the operator which transforms any sequence of function $\left[g_j(x) \right]_{j_1-1 \leq j < j_2} \in (\mathbf{C})^{j_2-j_1}$ into the sequence of functions $\left\{ \left[E g_j(x) \right]_{j_1 \leq j < j_2}, g_{j_1-1} \right\}$.

The finite EZC transform operator \mathbf{T}_F can be decomposed into a finite wavelet transform followed by the operator \mathbf{E}_F :

$$\mathbf{T}_F = \mathbf{E}_F \circ \mathbf{W}_F .$$

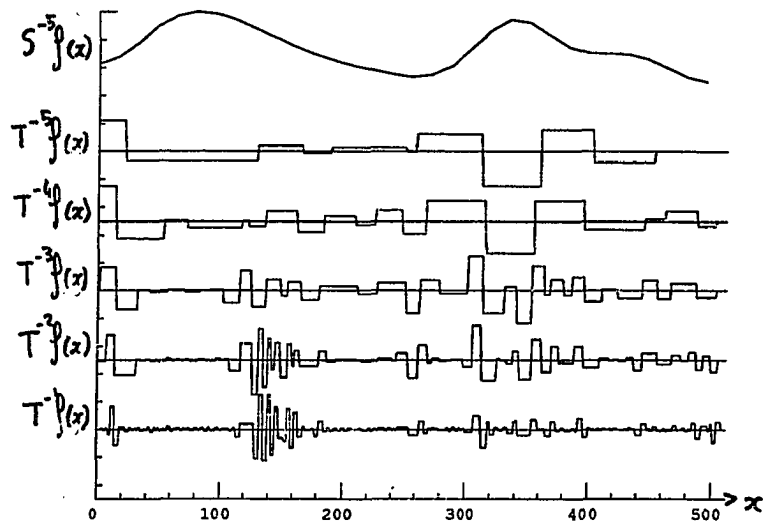


Fig. 3.10. Energy Zero-Crossings representation of the signal shown in Fig. 3.3. It is derived from the zero-crossings and local energies of the wavelet transform shown in Fig. 3.4. The top curve is $S^{-5}f(x)$ and the other piecewise constant curves are the graphs of $T^j f(x)$ for $0 > j \geq -5$.

3.4. Properties of an Energy Zero-Crossings representation

- Translation property

An Energy Zero-Crossings representation is clearly translating when the signal translates, since the zero-crossings of $W^j f(x)$ are translated and the energies between two zero-crossings are not modified.

$$\text{If } g(x) = f(x-t) \text{ then } \forall j \in \mathbb{Z}, \quad T^j g(x) = T^j f(x-t). \quad (3.50)$$

- Energy conservation

We can derive an energy conservation property from equation (3.46) and from the energy conservation equations of a dyadic wavelet transform.

For an infinite energy zero-crossing representation we have :

$$\forall f(x) \in L^2(\mathbb{R}), \quad \|f\|^2 = \sum_{j \in \mathbb{Z}} \|T^j f\|^2. \quad (3.51)$$

In the case of a finite energy zero-crossings representation the energy conservation is expressed

by :

$$\forall S^{j_2}f \in V_{j_2}, \quad \|S^{j_2}f(x)\|^2 = \sum_{j=j_1}^{j_2} \|T^j f\|^2 + \|S^{j_1}f(x)\|^2. \quad (3.52)$$

3.4.1. Distance on the Energy Zero-Crossing representation

A natural distance on the EZC representations can be derived from the energy conservation equations (3.51) and (3.52). For an infinite EZC representation, this distance is defined as follows. Let $f(x) \in L^2(\mathbb{R})$, $g(x) \in L^2(\mathbb{R})$ and $T_I f$, $T_I g$ be respectively their EZC representations, then

$$d(T_I f, T_I g) = \left[\sum_{j \in \mathbb{Z}} \|T^j f - T^j g\|^2 \right]^{\frac{1}{2}}. \quad (3.53)$$

One can verify that d is indeed a distance. The energy conservation equations can be written

$$d(T_I f, 0) = \|f\|. \quad (3.54)$$

For any pair of functions $f(x)$ and $g(x)$ in $L^2(\mathbb{R})$ we also have

$$d(T_I f, T_I g) \leq d(T_I f, 0) + d(T_I g, 0) = \|f\| + \|g\|.$$

The distance d is thus closely related to the norm in $L^2(\mathbb{R})$. In the finite case the distance d is similarly defined. Let $S^{j_2}f(x) \in V_{j_2}$ and $S^{j_2}g \in V_{j_2}$ be two functions approximated at the resolution 2^{j_2} . The distance between the two corresponding finite EZC representations is defined by

$$d(T_F(S^{j_2}f), T_F(S^{j_2}g)) = \left[\sum_{j=j_1}^{j_2-1} \|T^j f - T^j g\|^2 + \|S^{j_1}f - S^{j_1}g\|^2 \right]^{\frac{1}{2}}. \quad (3.55)$$

We can also derive from the energy conservation equation (3.52) that

$$d(T_F(S^{j_2}f), 0) = \|S^{j_2}f\| \quad \text{and} \quad (3.56)$$

$$d(T_F(S^{j_2}f), T_F(S^{j_2}g)) \leq \|S^{j_2}f\| + \|S^{j_2}g\|. \quad (3.57)$$

Since $T^j f(x)$ and $T^j g(x)$ are piecewise-constant functions, the integral

$$\int_{-\infty}^{+\infty} (T^j f(x) - T^j g(x))^2 dx = \|T^j f - T^j g\|^2 \quad (3.58)$$

is simple and quick to compute. It is calculated by multiplying the values of $T^j f(x)$ and $T^j g(x)$ between each pair of zero-crossings. The distance d can thus easily be implemented.

The distance d as previously defined is a global distance which compares two EZC representations over the entire spatial domain. A pattern is often a local feature embedded in the signal. For pattern matching purposes, we thus want to define a local distance which locally compares two EZC representations. In order to derive such a distance from d , we study the decomposition at all scales of a local feature such as a dirac $\delta_{x_0}(x)$ centered in x_0 .

$$W^j \delta(x) = \delta_{x_0} * \psi^j(x) = \psi^j(x - x_0) . \quad (3.59)$$

Let σ be the size of the interval on which the energy of $\psi(x)$ is mostly concentrated :

$$\int_{-\sigma}^{\sigma} \psi^2(x) dx \approx \int_{-\infty}^{+\infty} \psi^2(x) dx . \quad (3.60)$$

Equations (3.59) and (3.60) show that the energy of $W^j \delta_{x_0}(x)$ is mainly concentrated on the interval $[x_0 - 2^{-j}\sigma, x_0 + 2^{-j}\sigma]$. This implies that

$$T^j \delta_{x_0}(x) \approx 0 \quad \text{for } |x - x_0| \geq 2^{-j} \sigma . \quad (3.61)$$

In the case of an infinite EZC representation, it is thus natural to define the following local distance d_{x_0} for comparing two representations in the neighborhood of a point x_0 :

$$d_{x_0}(T_I f, T_I g) = \left[\sum_{j \in \mathbb{Z}} \int_{x_0 - 2^{-j}\sigma}^{x_0 + 2^{-j}\sigma} (T^j f(x) - T^j g(x))^2 dx \right]^{\frac{1}{2}} . \quad (3.62)$$

For a finite EZC representation, the local distance d_{x_0} is given by

$$d_{x_0}(T_F(S^{j_1}f), T_F(S^{j_2}g)) = \left[\sum_{j \in \mathbb{Z}} \int_{x_0 - 2^{-j}\sigma}^{x_0 + 2^{-j}\sigma} (T^j f(x) - T^j g(x))^2 dx + \int_{x_0 - 2^{-j_1}\sigma}^{x_0 + 2^{-j_1}\sigma} (S^{j_1}f(x) - S^{j_1}g(x))^2 dx \right]^{\frac{1}{2}} . \quad (3.63)$$

When matching patterns with a coarse to fine strategy, we decompose the local distance d_{x_0} into a sum of local distances $d_{x_0}^j$ such that

$$d_{x_0}^j(T^j f, T^j g) = \left[\int_{x_0 - 2^{-j}\sigma}^{x_0 + 2^{-j}\sigma} (T^j f(x) - T^j g(x))^2 dx \right]^{\frac{1}{2}} . \quad (3.64)$$

$d_{x_0}(T^j f, T^j g)$ is a measure of the local distortion between $f(x)$ and $g(x)$ near the point x_0 , at the scale 2^j .

3.4.2. Completeness of the Energy Zero-Crossing representation

In this paragraph, we study the completeness of the finite Energy Zero-Crossing representation. The finite Energy Zero-Crossing representation is complete if and only if the operator T_F admits an inverse T_F^{-1} on its range. Since $T_F = E_F \circ W_F$ and since we know that W_F is an isomorphism for V_{j_2} onto F , we must prove that the restriction of E_F to F is invertible on its range. This problem is difficult to solve mathematically because E_F is a nonlinear operator. Hence, we take an experimental approach to the problem and show that one can develop an iterative algorithm which implements the inverse of the restriction of E_F to F .

For any function $S^{j_2}f \in V_{j_2}$, we want to reconstruct the finite wavelet transform $W_F(S^{j_2}f)$ from the EZC representation $T_F(S^{j_2}f)$. We must therefore characterize each function $W^j f(x)$ with the positions of its zero-crossings and the values of its local energies. Let Γ_f be the set of all the sequences $\{g_j(x)\}_{j_1-1 \leq j < j_2} \in (\mathbb{C})^{j_2-j_1}$, such that $E_F\{g_j(x)\}_{j_1 \leq j < j_2} = T_F(S^{j_2}f)$. For any such sequence, $g_{j_1-1}(x) = S^{j_1}f(x)$, and for all integers $j_1 \leq j < j_2$, the zero-crossings and local energies of $g_j(x)$ and $T^j f(x)$ are the same. Γ_f is clearly not a vector space. The wavelet representation $W_F(S^{j_2}f)$ is a member of the intersection of Γ_f and F . If the restriction of E_F to F is injective then this intersection is reduced to $W_F f$:

$$\Gamma_f \cap F = \left\{ W_F(S^{j_2}f) \right\}. \quad (3.65)$$

We have defined in (3.41) a linear projection operator P_F on the vector space F . Let P_{Γ_f} be a projector on Γ_f . Since Γ_f is not a vector space, P_{Γ_f} is a nonlinear operator. By definition P_{Γ_f} satisfies the following two properties :

$$\forall \{g_j\}_{j_1-1 \leq j < j_2} \in (\mathbb{C})^{j_2-j_1}, \quad P_{\Gamma_f}\{g_j\}_{j_1-1 \leq j < j_2} \in \Gamma_f \quad \text{and}, \quad (3.66)$$

$$\{g_j\}_{j_1-1 \leq j < j_2} \in \Gamma_f \quad \text{if and only if} \quad P_{\Gamma_f}\{g_j\}_{j_1-1 \leq j < j_2} = \{g_j\}_{j_1-1 \leq j < j_2}. \quad (3.67)$$

Since the wavelet transform $W_F(S^{j_2}f)$ is a member of the intersection of Γ_f and F , it is a fixed point of both operators P_{Γ_f} and P_F . If the EZC representation is complete then assertion (3.65) shows that $W_F(S^{j_2}f)$ is their unique common fixed point. Let P be a composition of P_{Γ_f} with P_F

$$P = P_F \circ P_{\Gamma_f} \quad (3.68)$$

$W_F(S^{j_2}f)$ is also the a fixed point of P . The reconstruction of $W_F(S^{j_2}f)$ from the EZC representation $T_F(S^{j_2}f)$ is based on this property.

A classical method for computing a fixed point of an operator is to iterate on this operator from a given initial point. Let P^n be the composition n times of the operator P and I be an initial point in $(C)^{j_2-j_1}$. We would like to show that

$$\lim_{n \rightarrow \infty} P^n(I) = W_F(S^{j_2}f) . \quad (3.69)$$

Fig. 3.11 illustrates the principle of this reconstruction algorithm.

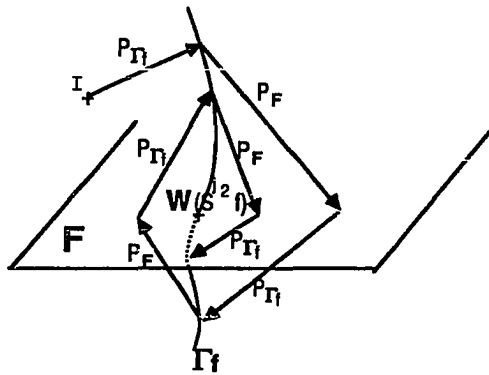


Fig. 3.11 Illustration of the reconstruction algorithm. Γ_f is symbolized by a curve and F by a plane. By iterating on a composition of the operators P_{Γ_f} and P_F , we want to reach $W_F(S^{j_2}f)$ which is at the intersection of Γ_f and F . The initial point I is anywhere in $(C)^{j_2-j_1}$.

Since the operator P is not a contracting operator, the algorithm might not converge from any

initial point. With the implementation of the operator P described in paragraph 3.5.2, we have shown experimentally that for any chosen point I the algorithm does converge. In about than ten iterations, the function $P^n(I)$ is a very good reconstruction of $W_F(S^{j_2}f)$. Fig. 3.12 shows the result of such an iteration by using the EZC representation given in Fig. 3.10. The quality of the reconstruction can be appreciated by comparing this reconstruction with the original wavelet decomposition shown in Fig. 3.4. From this reconstruction of the wavelet transform we have reconstructed the original signal by applying the inverse wavelet transform operator W_F^{-1} . The reconstruction of the approximated function is shown in Fig. 3.13. We have obtained the same quality of reconstruction for all the signals that we have decomposed. The signal shown in Fig. 3.3 is the scan line of an image. For all the image scan lines that we have tested, the reconstruction from the EZC representation had the same quality. We have also tested the reconstruction algorithm on some particularly interesting functions of V_{j_2} . We have shown numerically that if $S^{j_2}f = \rho^{j_2}(x)$ or $S^{j_2}f = \xi^{j_2}(x)$, the reconstruction algorithm also converges towards the original wavelet representation. By applying the inverse wavelet transform operator W_F^{-1} , we have then been able to reconstruct the original functions $\rho^{j_2}(x)$ and $\xi^{j_2}(x)$. Since the representation is translating, this shows that we can reconstruct any function of the two families $\left[\rho^{j_2}(x - 2^{-j_2}n)\right]_{n \in \mathbb{Z}}$ and $\left[\xi^{j_2}(x - 2^{-j_2}n)\right]_{n \in \mathbb{Z}}$. Each of these families is a basis of the vector space V_{j_2} but since the operator T_F is not linear, we cannot generalize this result to any signal $S^{j_2}f \in V_{j_2}$. For all the signals that we have tested, after three iterations we already had a good reconstruction of the finite dyadic wavelet transform. At the highest scales 2^j , the wavelet transforms $W^j f(x)$ take a few more iterations to be properly reconstructed at every point. As the value of the minimum resolution 2^{j_1} is decreased, the quality of the reconstruction is not modified.

A Wavelet transform and thus an Energy Zero-Crossing representation is defined with respect to a wavelet function $\psi(x)$. In the example shown in this paper the wavelet $\psi(x)$ was the function shown in Fig. 3.2. We have also tested the reconstruction with another wavelet which was much less regular. This other wavelet was differentiable but not continuously differentiable. Very similar results were obtained on the EZC representation defined with respect to this other wavelet.

This reconstruction algorithm cannot provide a proof for the completeness of a finite Energy Zero-Crossings representation, since we cannot make an extensive test on all the possible signals $S^{j_2}f \in V_{j_2}$. However, given these reconstructions, we can expect that this representation is indeed complete for any kind of signal in V_{j_2} or at least for a large class of functions within this vector space.

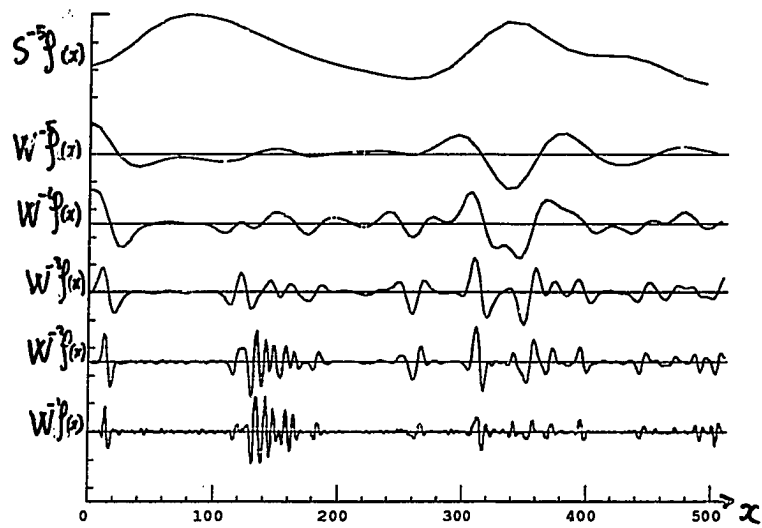


Fig. 3.12 Reconstruction of the dyadic Wavelet transform with the iterative algorithm previously described. The quality of this reconstruction can be appreciated by comparing this graph with the original wavelet transform shown in Fig. 3.4.

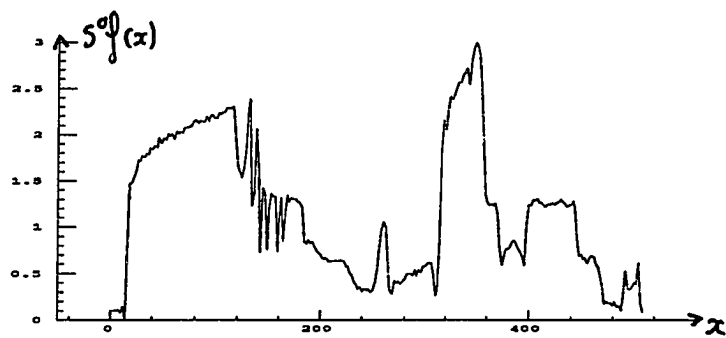


Fig. 3.13 Reconstruction of the original signal by applying the inverse wavelet transform operator on the wavelet reconstruction shown in Fig. 3.12. The quality of this reconstruction can be appreciated by comparing this graph with the original signal shown in Fig. 3.3.

3.4.3. Continuity of the Energy Zero-Crossing representation

In this paragraph, we show that the operators T_F and T_I can have some local discontinuities when some zero-crossings are created or disappear at a scale 2^j . We study this problem for a finite EZC representation but the same result applies for an infinite representation. The operator T_F is said to be continuous if for any signal $S^{j_2}f \in V_{j_2}$, the addition of a signal $\epsilon(x)$ of small energy produces only a small distortion on the EZC representation of $S^{j_2}f(x)$. This continuity cannot be derived from the energy conservation equation because T_F is not a linear operator. Since $T_F = E_F \circ W_F$ and W_F is continuous, the continuity of T_F depends upon the continuity of the restriction of E_F to F . The continuity of the restriction of E_F to F implies that $\|W_F(f) - W_F(f+\epsilon)\|$ is small then $d(T_F(S^{j_2}f), T_F(S^{j_2}(f+\epsilon)))$ remains small. We show that this is not true if the perturbation $\epsilon(x)$ creates or suppresses a pair of zero-crossings in $W^j f(x)$ at a given scale 2^j . This discontinuity phenomenon is illustrated by Fig. 3.14.

Let $(z_{k,1}^j, z_{k,2}^j)$ be a pair of zero-crossings created by the perturbation $\epsilon(x)$ in between two zero-crossings (z_{k-1}^j, z_k^j) of $W^j f(x)$. The energy e_k^j of $W^j f(x)$ in the interval $[z_{k-1}^j, z_k^j]$ is suddenly divided into $e_{k,1}^j$, $e_{k,2}^j$ and $e_{k,3}^j$. If the perturbation $\epsilon(x)$ is small then $e_{k,1}^j + e_{k,3}^j \approx e_k^j$, $e_{k,2}^j \approx 0$ and $z_{k,1}^j = z_{k,2}^j$. Even if the perturbation $\epsilon(x)$ has a very low energy, $T^j(f+\epsilon)$ can be significantly different from $T^j f$ between the zero-crossings z_{k-1}^j and z_k^j (see Fig. 3.14). The following equation gives an estimation of the distortion due to the creation of a new pair of zero-crossings :

$$\int_{z_{k-1}^j}^{z_k^j} (T^j f(x) - T^j(f+\epsilon)(x))^2 dx \leq (e_k^j \sqrt{\frac{z_{k,1}^j - z_{k-1}^j}{z_k^j - z_{k-1}^j}} - e_{k,1}^j)^2 + (e_k^j \sqrt{\frac{z_k^j - z_{k,2}^j}{z_k^j - z_{k-1}^j}} - e_{k,3}^j)^2.$$

In general, a small perturbation rather creates or suppresses some zero-crossings in regions of low local energies. The perturbation estimated by the previous equation is then negligible. It is also important to observe that the distortion of $T_F(S^{j_2}f)$ introduced by new zero-crossings remains localized. The overall representation $T_F(S^{j_2}f)$ is not modified. When testing the EZC representation on the stereo-matching problem, we shall see that these local discontinuities do not disturb much the matching process.

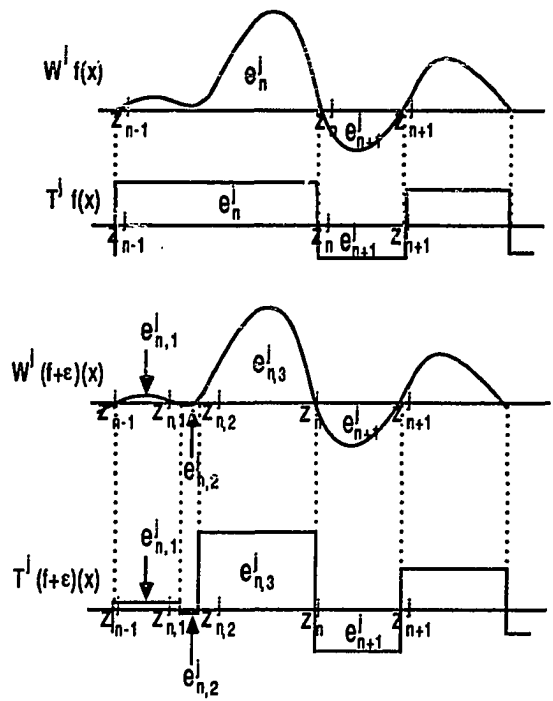


Fig. 3.14 When creating a new zero-crossing, a small perturbation $\varepsilon(x)$ can significantly modify the Energy Zero-Crossing representation. The energy e_n^I is suddenly divided into $e_{1,n}^I$, $e_{2,n}^I$ and $e_{3,n}^I$.

In the previous paragraph, we have shown that the operator T_F is invertible for a large class of signals. Let us suppose that it is invertible on its range and let T_F^{-1} denote its inverse. The inverse operator T_F^{-1} is said to be continuous if any small perturbation of a representation $T_F f$ measured with d corresponds to a small distortion of the original signal $f(x)$. Since the inverse wavelet operator W_F^{-1} is continuous, it is sufficient to prove that the wavelet transform $W_F f$ is only slightly modified. In this case we do not have any problem related to the creation of new pairs of zero-crossings, since the EZZC representation is supposed to be only slightly perturbed. The fact that our reconstruction algorithm does converge shows experimentally that any small perturbation of $T_F f$ corresponds to a small distortion of the associated wavelet representation $W_F f$.

3.5. Numerical algorithms

In this paragraph we describe the numerical implementation of a finite Energy Zero-Crossing transform. We then show how to compute the reconstruction algorithm described in paragraph 3.4.2 .

3.5.1. Implementation of a finite Energy Zero-Crossing representation

In the following, we detail the computation of a finite EZC representation for any signal approximated at a resolution 1 . We suppose that our measuring device provides us with a uniform sampling of an approximated signal at the rate 1. Theorem 3.2 shows how to interpolate between these samples to compute the value of this approximated signal everywhere. In order to calculate an EZC representation we must first compute the corresponding dyadic wavelet representation. Then we can estimate the position of the zero-crossings and the value of the local energies of this wavelet transform. In practice we cannot compute the values of the functions $W^j f(x)$ at every point. We can only calculate a uniform sampling of these functions. In order to estimate the position of the zeros and the value of the energies with the same precision for all the scales 2^j , we must sample $W^j f(x)$ at a rate proportional to 2^j . Indeed, the frequency energy of $W^j f(x)$ is mainly concentrated in frequency band whose size is proportional to 2^j . In order to simplify the implementation we choose a sampling rate which is a power of 2 . Let 2^{j_0+j} be the sampling rate at each scale 2^j . We show that we can develop a discrete equivalent of the pyramidal algorithm described in paragraph 3.2.3.2. The position of the zero-crossings and the value of the local energies are then estimated with a simple linear interpolation between the samples of this discrete wavelet representation.

3.5.1.1. Dyadic wavelets for discrete algorithms

In this paragraph, we define a particular sub-class of wavelets such that the discrete wavelet transform can be computed with a pyramidal algorithm. We saw in paragraph 3.2.1 that any smoothing function $\theta(x)$ has a Fourier transform $\hat{\theta}(\omega)$ which can be written

$$\hat{\theta}(\omega) = \prod_{p=1}^{+\infty} U(2^{-p}\omega) . \quad (3.71)$$

The Fourier transform of an associated wavelet $\psi(x)$ can be expressed as

$$\hat{\psi}(\omega) = G\left(\frac{\omega}{2}\right)\hat{\theta}\left(\frac{\omega}{2}\right), \text{ where } |G(\omega)|^2 + |U(\omega)|^2 = 1. \quad (3.72)$$

As explained in paragraph 3.3.1, we are interested in wavelets $\psi(x)$ which are proportional to the second derivative of a smoothing function $\xi(x)$. We saw in equation (3.43) that the Fourier transform $\hat{\psi}(\omega)$ must then have a zero of order two at $\omega=0$. Equation (3.72) implies that $G(\omega)$ must also have a zero of order two at $\omega=0$. This is verified if and only if the first three derivatives of $U(\omega)$ are equal to zero at $\omega=0$. To be able to compute a discrete wavelet transform with a pyramidal algorithm, we will also suppose that $U(\omega)$ and $G(\omega)$ are $2\pi 2^{j_0-1}$ periodic. The functions $U(\omega)$ and $G(\omega)$ can then be written as Fourier series :

$$U(\omega) = \sum_{n \in \mathbb{Z}} u_n e^{in 2^{j_0-1} \omega} \quad \text{and} \quad G(\omega) = \sum_{n \in \mathbb{Z}} g_n e^{in 2^{j_0-1} \omega}. \quad (3.73)$$

The inverse Fourier transforms of $U(\omega)$ and $G(\omega)$ as defined in paragraph 3.2.3.2 are two distributions given by :

$$u(x) = \sum_{n \in \mathbb{Z}} u_n \delta(x - n 2^{j_0-1}) \quad \text{and} \quad g(x) = \sum_{n \in \mathbb{Z}} g_n \delta(x - n 2^{j_0-1}).$$

We represent these two distributions by the two $L^2(\mathbb{Z})$ sequences $U = [u_n]_{n \in \mathbb{Z}}$, $G = [g_n]_{n \in \mathbb{Z}}$ and call them discrete filters. In the next paragraph we show that we can compute a discrete wavelet decomposition by successively convolving the signal with these two discrete filters.

Let us now describe the particular dyadic wavelet which has been used for computing the examples shown in this paper. In this particular case we chose a sampling coefficient 2^{j_0} equal to 8 ($j_0=3$). The Fourier transform of the smoothing function shown in Fig. 3.1 corresponds to a function $U(\omega)$ which is 8π periodic and such that

$$U(\omega) = e^{-\frac{\omega^2}{19.25}} \quad \text{for } \omega \in [-4\pi, 4\pi]. \quad (3.74)$$

The coefficient 19.25 was adjusted numerically in order to have $|\Theta| = 1$. We do not have any general characterization of the functions $U(\omega)$ which would enable us adjust the norm of $\Theta(x)$. The Fourier transform of the associated wavelet shown in Fig. 3.2 corresponds to $G(\omega) = -\sqrt{1 - U(\omega)^2}$. Fig. 3.15 gives the corresponding values of the two discrete filters $U = [u_n]_{n \in \mathbb{Z}}$ and $G = [g_n]_{n \in \mathbb{Z}}$.

n	u_n	g_n	n	u_n	g_n
0	0.151	-0.898	8	-0.014	0.012
1	0.144	0.100	9	-0.015	0.004
2	0.125	0.092	10	-0.013	-0.001
3	0.097	0.080	11	-0.008	-0.003
4	0.066	0.066	12	-0.003	-0.004
5	0.035	0.050	13	0.000	-0.003
6	0.011	0.035	14	0.002	-0.002
7	-0.006	0.022	15	0.002	-0.001

Fig. 3.15 Coefficients of the discrete filters U, G . These filters are symmetrical with respect to $n = 0$: $u_{-n} = u_n$ and $g_{-n} = g_n$.

3.5.1.2. Interpolation of a finite resolution approximation

In this paragraph, we will describe the interpolation of a discrete approximated signal and explain how to compute a scaling function to define the concept of resolution. Let us suppose that our measuring device provides us with a uniform sampling at the rate 1 of a signal measured at the resolution 1. Let $S^0f(x) \in V_0$ denote this approximated signal; the uniform sampling corresponds to $\left[S^0f(n) \right]_{n \in \mathbb{Z}}$. As we shall see in paragraph 3.5.1.3, in order to apply the discrete pyramidal algorithm which computes the discrete wavelet transform of S^0f , we must first calculate a uniform sampling of $S^0f(x)$ at a rate 2^{j_0+1} . Such a sampling can be calculated with the spline function $\rho(x)$ defined in theorem 3.2. Indeed, we saw in theorem 3.2 that

$$S^0f(x) = \sum_{k=-\infty}^{+\infty} S^0f(k) \rho(x - k) .$$

For any sample $n 2^{-j_0+1}$ we thus have

$$S^0f(n 2^{-j_0+1}) = \sum_{k=-\infty}^{+\infty} S^0f(k) \rho(n 2^{-j_0+1} - k) . \quad (3.75)$$

This equation shows that the interpolated discrete signal $S^0 f(n 2^{-j_0+1})$ can be computed by putting $2^{j_0-1} - 1$ zeros in between each sample of $\{S^0 f(n)\}_{n \in \mathbb{Z}}$ and convolving the resulting signal with the discrete interpolation filter $\rho_d = \{\rho(n 2^{-j_0+1})\}_{n \in \mathbb{Z}}$.

Let us now discuss the choice of a scaling function for implementing the concept of resolution. Theorem 1.2 shows that the Fourier transform $\hat{\phi}(\omega)$ of a scaling function can be computed from a function $H(\omega)$ satisfying properties (a), (b) and (c). In order to be able to define a finite dyadic wavelet transform, the scaling function $\phi(x)$ must also satisfy the conditions of lemma 3.1. The Fourier transform $\hat{\phi}(\omega)$ must have a decay at infinity which is faster than $\frac{\theta(\omega)}{\omega}$:

$$\hat{\phi}(\omega) = O\left(\frac{\theta(\omega)}{\omega}\right) \quad \text{at infinity}.$$

This condition is always satisfied if the Fourier transform of $\phi(x)$ has a compact support. These scaling functions have been studied by Y. Meyer [37]. They correspond to the functions $H(\omega)$ which are equal to 1 on the interval $[-\frac{\pi}{3}, \frac{\pi}{3}]$. The inconvenience of these scaling functions is that they have a slow effective decay at infinity. The interpolation function $\rho(x)$ defined in theorem 3.2 also has a slow decay. This means that the coefficients of the interpolation filter ρ_d decrease slowly. It is then more efficient to compute the convolution product of the interpolation (3.75) with a multiplication in the Fourier domain.

If we want to be able to compute directly the interpolation equation in the spatial domain, we must choose a scaling function which has a faster effective decay at infinity. In this case, the Fourier transform $\hat{\phi}(\omega)$ does not have a compact support. We can choose, for example, the scaling function plotted in the Fig. 1.1 of chapter 1. In each interval $[k, k+1]$ this function $\phi(x)$ corresponds to a polynomial of order three. It is further characterized in appendix A. From theorem 3.2, we can derive that the Fourier transform of the corresponding spline function $\rho(x)$ is given by

$$\hat{\rho}(\omega) = \left[\frac{\sin \frac{\omega}{2}}{\frac{\omega}{2}} \right]^4 (1 - \frac{2}{3} \sin^2 \frac{\omega}{2})^{-1}. \quad (3.76)$$

In this particular case, the function $\rho(x)$ is cubic spline polynomial. The coefficients of the filter ρ_d are given in Fig. 3.16 for $j_0 = 3$.

n	$\rho(\frac{n}{4})$	n	$\rho(\frac{n}{4})$	n	$\rho(\frac{n}{4})$	n	$\rho(\frac{n}{4})$
0	1	4	0	8	0	12	0
1	0.881	5	-0.123	9	0.033	13	-0.008
2	0.600	6	-0.127	10	0.034	14	-0.009
3	0.269	7	-0.068	11	0.018	15	-0.005

Fig. 3.16 Coefficients of the discrete filter $\left[\rho(n2^{-j_0+1}) \right]_{n \in \mathbb{Z}}$ for $j_0 = 3$. This filter is symmetrical about $n = 0$.

3.5.1.3. Implementation of a discrete dyadic wavelet transform

In this paragraph, we describe the pyramidal implementation of a discrete wavelet transform. This algorithm is a generalization of the algorithm that we developed in chapter 1 for orthogonal wavelets. It can also be viewed as a discretization of the pyramidal algorithm described in paragraph 3.2.3.2 for computing a finite dyadic wavelet transform. Let $S^0 f(x) \in \mathbf{V}_0$ be the approximated signal that we want to decompose. Let us denote by $W^j f_d$ the discrete signal equal to a uniform sampling of $W^j f(x)$ at a rate 2^{j_0+j} :

$$W^j f_d = \left[W^j f(k2^{-j_0-j}) \right]_{k \in \mathbb{Z}} = \left[f * \psi^j(k2^{-j_0-j}) \right]_{k \in \mathbb{Z}}. \quad (3.77)$$

Let us also denote by $S^j f_d$ the discrete signal equal to uniform sampling of $S^j f(x)$ at a rate 2^{j_0+j-1} :

$$S^j f_d = \left[S^j f(k2^{-j_0-j+1}) \right]_{k \in \mathbb{Z}} = \left[f * \theta^j(k2^{-j_0-j+1}) \right]_{k \in \mathbb{Z}}. \quad (3.78)$$

Let 2^{-J} be the minimum resolution where we want to stop our wavelet decomposition. We now detail the computation of the discrete wavelet transform $\left\{ \left[W^j f_d \right]_{0 \leq j \leq J}, S^{-J} f_d \right\}$.

As described in paragraph 3.5.1.2, we suppose that we have already computed a uniform sampling at the rate 2^{j_0-1} of the approximated signal $S^0f(x)$ that we want to decompose. This uniform sampling corresponds to the discrete signal S^0f_d . The following lemma shows that for any scale 2^j , one can decompose $S^{j+1}f_d$ into S^jf_d and W^jf_d by convolving this discrete signal with the two filters U and G . This lemma is a discrete equivalent of equations (3.36) and (3.37).

Lemma 3.2

$$\forall j \in \mathbb{Z}, \quad W^jf_d = S^{j+1}f_d * G \quad \text{and} \quad (3.79)$$

$$\text{if } \left[\lambda_n \right]_{n \in \mathbb{Z}} = S^{j+1}f_d * U \quad \text{then} \quad S^jf_d = \left[\lambda_{2n} \right]_{n \in \mathbb{Z}}. \quad (3.80)$$

The proof of this lemma is given in appendix E. Lemma 3.2 shows that W^jf_d can be computed by convolving $S^{j+1}f_d$ with the discrete filter G . To compute S^jf_d , we must convolve $S^{j+1}f_d$ with the discrete filter U and keep every other sample of the convolution product. By iterating on equations (3.79) and (3.80), it is now easy to decompose the discrete signal S^0f_d into the discrete wavelet transform $\left\{ \left[W^jf_d \right]_{0 < j \leq J}, S^{-J}f_d \right\}$. This pyramidal algorithm is illustrated by the block diagram of Fig. 3.17. If S^0f_d has N non-zero samples, one can easily show that each discrete signal W^jf_d has approximately $N2^{j+1}$ non-zero samples and that $S^{-J}f_d$ has $N2^{-J}$ non-zero samples. The computational complexity of the algorithm is $N \log(N)$. The dyadic wavelet decomposition shown in Fig. 3.4 was computed with the coefficients of the filters U and G given in Fig. 3.15.

To compute the EZC representation, we can then estimate the position of the zero-crossings with a linear interpolation between the zero-crossing samples of each W^jf_d . The energies between each pair of zero-crossings can also be estimated with a similar linear interpolation from the square value of the samples.

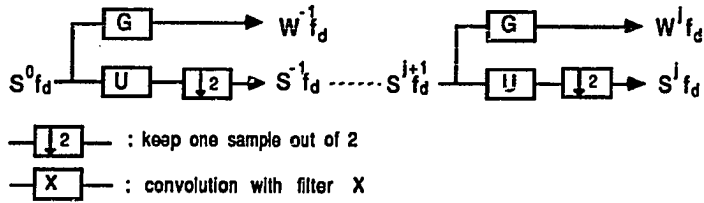


Fig. 3.17 This block diagram illustrates the pyramidal architecture of the algorithm which decomposes the interpolated signal $S^0 f_d$ into a discrete wavelet representation. This algorithm is based on convolutions with the two filters U and G .

3.5.2. Implementation of the Energy Zero-Crossing reconstruction algorithm

In this paragraph, we describe the numerical implementation of the reconstruction algorithm exposed in paragraph 3.4.2. This reconstruction algorithm is based on two projection operators : P_F and $P_{\Gamma F}$. We saw in paragraph 3.2.3.2 that the projection operator P_F could be decomposed into

$$P_F = W_F \circ A^0 \circ W_F^{-1}. \quad (3.81)$$

The discrete implementation of the operator W_F has been described in paragraph 3.5.1.3 . In the next paragraph we explain another discrete pyramidal algorithm for implementing the inverse wavelet operator W_F^{-1} . We then detail the implementation of the orthogonal projection operator A^0 and give a simple algorithm for computing the nonlinear projection on Γf .

3.5.2.1. Implementation of a discrete inverse dyadic wavelet transform

A discrete wavelet operator transforms a uniform sampling $S^0 f_d$ of an approximated signal $S^0 f(x)$ into a discrete dyadic wavelet representation $\left\{ \left[W^j f_d \right]_{0 \leq j \leq J}, S^{-J} f_d \right\}$. We now describe another pyramidal algorithm for implementing a discrete version of the inverse wavelet transform W_F^{-1} . This operator reconstructs $S^0 f_d$ from $\left\{ \left[W^j f_d \right]_{0 \leq j \leq J}, S^{-J} f_d \right\}$. The algorithm is based on a discretization of equation (3.39).

For each scale 2^j , we show how to compute $S^{j+1}f_d$ from the two discrete signals $S^j f_d$ and $W^j f_d$. The first step of this calculation consists of interpolating between each sample of $S^j f_d = [S^j f(n2^{-j_0-j+1})]_{n \in \mathbb{Z}}$ in order to get a sampling of $S^j f(x)$ at a rate 2^{j_0+j} : $\Lambda = [S^j f(n2^{-j_0-j})]_{n \in \mathbb{Z}}$. This interpolation is computed with the spline function $p(x)$ described in paragraph 3.5.1.2.

$$\forall n \in \mathbb{Z}, S^j f((2n+1)2^{-j_0-j}) \approx \sum_{k=-\infty}^{+\infty} S^j f(k2^{-j_0-j+1}) p\left(\frac{2n+1}{2}-k\right). \quad (3.82)$$

Equation (3.79) shows that the intermediate sample $[S^j f((2n+1)2^{-j_0-j})]_{n \in \mathbb{Z}}$ can be computed by putting a zero between each pair of samples of $S^j f_d$ and by convolving the resulting signal with the interpolation filter $\left[p\left(\frac{n}{2}\right)\right]_{n \in \mathbb{Z}}$. Fig. 3.18 gives the coefficients of this filter when $p(x)$ is a cubic spline polynomial. Such an interpolation is not exact but it provides a precise estimate of the intermediate samples. Indeed, the Nyquist rate of $S^j f(x)$ is approximately 2^j . Since we already have a sampling of $S^j f(x)$ at the rate 2^{j_0+j-1} , the function $S^j f(x)$ varies smoothly between two samples $n2^{-j_0-j+1}$ and $(n+1)2^{-j_0-j+1}$. The smoothness of $S^j f(x)$ is well approximated by the spline filter previously mentioned, so equation (3.82) gives us a close estimation of the intermediate samples.

Let $\tilde{U} = [u_{-n}]_{n \in \mathbb{Z}}$ and $\tilde{G} = [g_{-n}]_{n \in \mathbb{Z}}$ be the mirror filters of U and G defined in (3.73). The following Lemma shows that $S^{j+1}f_d$ can be computed by convolving $W^j f_d$ and Λ with the two filters \tilde{G} and \tilde{U} .

Lemma 3.3

$$\text{Let } \Lambda = [S^j f((2n+1)2^{-j_0-j})]_{n \in \mathbb{Z}}, \quad S^{j+1}f_d = \Lambda * \tilde{U} + W^j f_d * \tilde{G}. \quad (3.83)$$

The proof of lemma 3.3 is given in appendix F. By repeating this reconstruction operation for $0 > j \geq -J$, we can reconstruct $S^0 f_d$ from the discrete wavelet representation $\left\{[W^j f_d]_{0 < j \leq -J}, S^{-J} f_d\right\}$. The filters U and G that we used for our implementation are

symmetricals about $n = 0$, so $\tilde{U} = U$ and $\tilde{G} = G$. The block diagram shown in Fig. 3.18 illustrates the pyramidal algorithm which implements a discrete inverse wavelet transform W_F^{-1} .

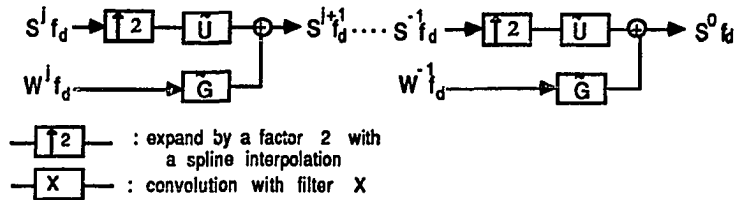


Fig. 3.18 This block diagram illustrates the pyramidal algorithm for reconstructing the interpolated signal $S^0 f_d$ from a discrete wavelet decomposition. This reconstruction is based on convolutions with the two discrete filters \tilde{U} and \tilde{G} .

As described in paragraph 3.2.3.2, in order to define the projection operator P_F , W_F^{-1} must be extended to the whole space $(L^2(\mathbb{R}))^{j_0-j_1}$. The discrete implementation of W_F^{-1} that we just described reconstructs $S^0 f_d$ from $\left\{ \left[W^j f_d \right]_{0 < j \leq J}, S^{-J} f_d \right\}$. To implement the projection operator P_F , we need to extend this algorithm to any sequence of discrete signals $\left[d_j \right]_{0 > j \geq J-1}$, where $d_j = \left[d_{n2^{-j+1}} \right]_{n \in \mathbb{Z}}$ is any sequence in $L^2(\mathbb{Z})$. Let $d = \left[d_{n2^{-j+1}} \right]_{n \in \mathbb{Z}}$ be the discrete signal which is obtained by applying the operator W_F^{-1} on $\left[d_j \right]_{0 > j \geq J-1}$. Theorem 3.2 shows that this discrete signal can be considered a uniform sampling at the rate 2^{j_0-1} of a function $d(x) \in V_{j_0-1}$, where

$$d(x) = \sum_{n=-\infty}^{+\infty} d_{n2^{-j_0+1}} 2^{-j_0+1} \rho^{j_0-1}(x - 2^{-j_0+1}n) . \quad (3.84)$$

To implement the operator P_F , we must compute the orthogonal projection of $d(x)$ on the vector space V_0 . This orthogonal projection will be characterized by a uniform sampling at a rate 1 in order to later apply the pyramidal wavelet algorithm described in paragraphs 3.5.1.2 and 3.5.1.3.

3.5.2.2. Implementation of the projection operator A^0

The operator A^0 is an orthogonal projection from $L^2(\mathbb{R})$ on the vector space V_0 . In this paragraph, we show how to compute the orthogonal projection on V_0 of any function $d(x) \in V_{j_0-1}$. The orthogonal projection $A^0 d(x)$ will be characterized by a uniform sampling at a rate 1. Equation (3.26) implies that

$$A^0 d(x) = \sum_{p=-\infty}^{+\infty} \langle d(x), \phi(x-p) \rangle \phi(x-p) . \quad (3.85)$$

The expression of $d(x)$ given in equation (3.84) yields

$$\langle d(x), \phi(x-p) \rangle = \sum_{n=-\infty}^{+\infty} d_{n2^{-j_0+1}} 2^{-j_0+1} \langle \rho^{j_0-1}(u-2^{-j_0+1}n), \phi(u-p) \rangle .$$

Each of the inner product $\langle \rho^{j_0-1}(u-2^{-j_0+1}n), \phi(u-p) \rangle$ can be expressed as a convolution product so that

$$\langle d(x), \phi(x-p) \rangle = \sum_{n=-\infty}^{+\infty} d_{n2^{-j_0+1}} 2^{-j_0+1} \rho^{j_0-1} * \phi(p - 2^{-j_0+1}n) . \quad (3.86)$$

The sequence of inner products $\left[\langle d(x), \phi(x-p) \rangle \right]_{p \in \mathbb{Z}}$ can thus be computed by convolving the sequence $\left[d_{n2^{-j_0+1}} \right]_{n \in \mathbb{Z}}$ with the discrete filter $\left[2^{-j_0+1} \rho^{j_0-1} * \phi(n2^{-j_0+1}) \right]_{n \in \mathbb{Z}}$ and keeping one sample out of 2^{j_0-1} of the convolution product. The uniform sampling of $A^0 d(x)$ at a rate 1 is given by the sequence $\left[A^0 d(k) \right]_{k \in \mathbb{Z}}$. Equation (3.85) yields

$$A^0 d(k) = \sum_{p=-\infty}^{+\infty} \langle d(x), \phi(x-p) \rangle \phi(k-p) . \quad (3.87)$$

This uniform sampling is therefore equal to the convolution of $\left[\langle d(x), \phi(x-p) \rangle \right]_{p \in \mathbb{Z}}$ with the filter $\left[\phi(n) \right]_{n \in \mathbb{Z}}$. In conclusion, equations (3.86) and (3.87) show that $\left[A^0 d(k) \right]_{k \in \mathbb{Z}}$ can be computed from the discrete signal $\left[d_{n2^{-j_0+1}} \right]_{n \in \mathbb{Z}}$ by

- convolving $\left[d_{n2^{-j_0+1}} \right]_{n \in \mathbb{Z}}$ with the discrete filter $\left[2^{-j_0+1} \rho^{j_0-1} * \phi(n2^{-j_0+1}) \right]_{n \in \mathbb{Z}}$,
- taking one sample out of 2^{j_0-1} of the convolved signal, and
- convolving the sub-sampled signal with the filter $\left[\phi(n) \right]_{n \in \mathbb{Z}}$.

The coefficients of the discrete filters $\left[c_n = 2^{-j_0+1} \rho^{j_0-1} * \phi(n 2^{-j_0+1}) \right]_{n \in \mathbb{Z}}$ and $\left[\phi(n) \right]_{n \in \mathbb{Z}}$ are given by Fig. 3.19 in the case of a cubic spline polynomial, for $j_0 = 3$.

n	c_n	n	c_n	n	c_n	n	c_n
0	0.272	4	-0.185	8	0.012	12	-0.006
1	0.237	5	-0.047	9	0.020	13	-0.009
2	0.153	6	-0.039	10	0.015	14	-0.006
3	0.056	7	-0.013	11	0.003	15	-0.001

n	$\phi(n)$	n	$\phi(n)$
0	1.089	4	0.013
1	-0.075	5	-0.006
2	0.047	6	0.003
3	-0.025	7	-0.002

Fig. 3.19 Coefficients of the filter $\left[\phi(n) \right]_{n \in \mathbb{Z}}$ and of the filter $\left[c_n = 2^{-j_0+1} (\rho^{j_0-1} * \phi)(n 2^{-j_0+1}) \right]_{n \in \mathbb{Z}}$ for $j_0 = 3$, in the case of a cubic spline polynomial.
These filters are symmetrical about $n = 0$.

Equation (3.81) shows that the projection operator P_F can now be implemented by computing an inverse discrete wavelet transform W_F^{-1} , then an orthogonal projection A^0 on the vector space V_0 and finally a discrete wavelet transform. In order to finish the implementation of the reconstruction algorithm described in paragraph 3.4.2, we must now numerically define the projection operator P_{Ff} .

3.5.2.3. Implementation of a projection operator on Γ_f

By definition, a projection on Γ_f should satisfy properties (3.66) and (3.67). It must transform any sequence of curves $[g_j(x)]_{j_1-1 \leq j < j_2} \in (\mathbf{C})^Z$ into a new sequence of curves $[h_j(x)]_{j_1-1 \leq j < j_2} \in \Gamma_f$. The function $h_{j-1}(x)$ should be equal to $S^{j-1}f(x)$, and for $j_1 \leq j < j_2$ each function $h_j(x)$ should have the same energies and zero-crossings as $T^j f(x)$. We describe a simple algorithm for implementing this deformation.

Let $j_1 \leq j < j_2$ and $[z_h^j]_{n \in Z}$, $[e_h^j]_{n \in Z}$ be respectively the positions of the zero-crossings and the energies of each function $T^j f(x)$. We deform a function $g_j(x)$ into a function $h_j(x)$ whose zero-crossings and local energies are equal to $[z_h^j]_{n \in Z}$ and $[e_h^j]_{n \in Z}$. This deformation is illustrated by Fig. 3.20. We first define a function $\alpha(x)$ such that for each pair of zeros (z_h^{j-1}, z_h^j)

$$\forall x \in [z_h^{j-1}, z_h^{j-1}] \quad , \quad \alpha(x) = g_j(x) + a x + b \quad \text{with} \quad \begin{cases} a z_h^{j-1} + b = -g_j(z_h^{j-1}) \\ a z_h^j + b = -g_j(z_h^j) \end{cases} \quad (3.88)$$

The function $\alpha(x)$ has a zero-crossing at each point $[z_h^j]_{n \in Z}$ but might have some other ones (see Fig. 3.20). We need to remove these spurious zero-crossings and keep the sign of $\alpha(x)$ constant and equal to the sign of e_h^j on each interval $[z_h^{j-1}, z_h^{j-1}]$. This operation is done in the following loop, in which we add a triangle function to $\alpha(x)$ to suppress the regions of $[z_h^{j-1}, z_h^{j-1}]$ where $\alpha(x)$ has a sign different than the sign of e_h^j (see Fig. 3.20).

While $\alpha(x)$ has a zero-crossing in the interval $[z_h^{j-1}, z_h^{j-1}]$:

$$\text{let } x_n \in [z_h^{j-1}, z_h^{j-1}] \text{ such that } \alpha(x_n) \operatorname{sign}(e_h^j) = \min_{x \in [z_h^{j-1}, z_h^{j-1}]} \{ \alpha(x) \operatorname{sign}(e_h^j) \} \quad ,$$

$$\text{for } x \in [z_h^{j-1}, x_n] \quad , \quad \alpha(x) = \alpha(x) - 2 \alpha(x_n) \frac{x - z_h^{j-1}}{x_n - z_h^{j-1}} \quad ,$$

$$\text{for } x \in [x_n, z_h^j] \quad , \quad \alpha(x) = \alpha(x) - 2 \alpha(x_n) \frac{x - z_h^j}{x_n - z_h^j} \quad ,$$

end of loop.

Let us call $\beta(x)$ the function $\alpha(x)$ which is obtained at the end of this loop. On each interval

$[z_{k-1}^j, z_k^{j-1}]$, the sign of $\beta(x)$ is equal to the sign of e_k^j and $\beta(z_{k-1}^j) = \beta(z_k^j) = 0$. We must now dilate $\beta(x)$ on each of these intervals in order to have a local energy equal to e_k^j . The function $h_j(x)$ is thus defined by

$$\forall n \in \mathbb{Z}, \quad \forall x \in [z_{k-1}^j, z_k^{j-1}], \quad h_j(x) = \left[\frac{e_k^j \beta(x)}{\int_{z_{k-1}^j}^{z_k^j} \beta(x)^2 dx} \right]^{\frac{1}{2}}. \quad (3.89)$$

The overall deformation process is illustrated in Fig. 3.20. One can verify that such a deformation defines a projection operator $P_{\Gamma\Gamma}$ which satisfies equations (3.66) and (3.67).

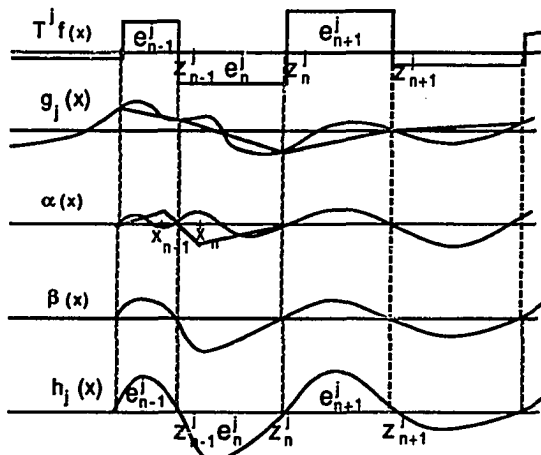


Fig. 3.20 Illustration of the deformation algorithm for implementing the projection operator $P_{\Gamma\Gamma}$. The function $g_j(x)$ is deformed in order to match its zero-crossings and local energy values with the zero-crossings and local energy values of $T^j f(x)$.

3.6. Application of the Energy Zero-Crossing representation to stereo matching

An important problem in computer vision is to recover a three-dimensional description of the surfaces which appear in a scene. From two images of a single scene, one can indeed compute the distance between each point of the scene and the pair of stereo cameras. Let P be a point of the world which is projected on both images. Let P_l and P_r be respectively the projections of P on the left and the right images (see Fig. 3.21). One can compute the distance from P to the pair of stereo cameras from the difference of positioning τ between P_l and P_r (see Fig. 3.21). This difference of positioning is called a disparity. The goal of a stereo-matching algorithm is to find for each point P_l of the left image the matching point P_r of the right image such that P_l and P_r are the projections of the same point P of the scene. The principle of such an algorithm is to look for a point P_r in the right image such that locally around P_r the image is the most similar to the neighborhood around P_l in the left image. Although this matching problem is a priori a two-dimensional search, it can be reduced to a one-dimensional search by using the epipolar geometry of the cameras (see Fig. 3.21). An epipolar plane is a plane which contains the point P and the optical centers of the left and right cameras. The intersections of such a plane with the left and the right images define a pair of epipolar lines. The stereo match of any point which is on a left epipolar line can be found on the corresponding right epipolar line. The problem is thus reduced to a one-dimensional matching problem along each pair of epipolar lines. Much research has been devoted to finding efficient algorithms for matching these epipolar lines [15, 34]. We show that such an algorithm can be implemented with a coarse to fine strategy on the EZC representation.

3.6.1. Matching Algorithm

Let us suppose that our left and right images have N^2 pixels each. The left and right epipolar scan lines have N samples each : $[l_n]_{1 \leq n < N}$ and $[r_n]_{1 \leq n < N}$. Each of these sequences of samples characterize the approximation of a signal at the resolution 1. Let $S^0l(x)$ and $S^0r(x)$ be, respectively, the corresponding left and right approximated signals. For every point x_0 , the goal of the matching process is to find the disparity $\tau(x_0)$ such that $S^0l(x_0)$ and $S^0r(x_0 - \tau(x_0))$ are locally the most similar. For this purpose, we compute the finite EZC representation of $S^0l(x)$ and $S^0r(x)$ and locally compare these two representations with a

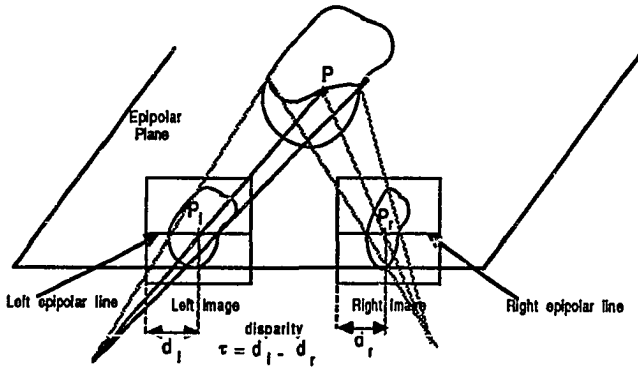


Fig. 3.21 Example of horizontal epipolar geometry of a pair of stereo images. A point P of the scene appears respectively in P_l and P_r in the left and right images.

coarse to fine strategy. A coarse to fine strategy consists of matching first the coarser details of the two signals $S^0l(x)$ and $S^0r(x)$ and then using the finer details to get more precise matches. Let $\left\{ \left[T^j l(x) \right]_{-J \leq j \leq -1}, S^{-J} l(x) \right\}$ and $\left\{ \left[T^j r(x) \right]_{-J \leq j \leq -1}, S^{-J} r(x) \right\}$ be, respectively, the finite EZC representation of the left and the right approximated signals between the scales 1 and 2^{-J} . We have described in paragraph 3.5.1 how to compute these representations given the sequences of samples $\left[l_n \right]_{1 \leq n < N}$ and $\left[r_n \right]_{1 \leq n < N}$. Matching two signals $T^j l(x)$ and $T^j r(x)$ consists of trying to match their zero-crossings. We use the local distance defined by equation (3.64) for matching the zero-crossings around which $T^j l(x)$ and $T^j r(x)$ are the most similar. Let $\left[z_k^j \right]_{j \in Z}$, $\left[e_k^j \right]_{j \in Z}$ and $\left[\bar{z}_k^j \right]_{j \in Z}$, $\left[\bar{e}_k^j \right]_{j \in Z}$ be, respectively, the zero-crossings and energies of $T^j l(x)$ and $T^j r(x)$. Given a zero-crossing z_k^j of $T^j l(x)$ we want to find the zero-crossing \bar{z}_k^j of $T^j r(x)$ such that if $\tau = z_k^j - \bar{z}_k^j$ then

$$d_{z_k^j}(T_F l(x), T_F r(x-\tau)) = \left(\int_{z_k^j-2-j\sigma}^{z_k^j+2-j\sigma} (T^j l(x) - T^j r(x-\tau))^2 dx \right)^{1/2} = d_{\min} \quad (3.90)$$

is minimum. This means that the neighborhood of $T^j r(x)$ around \bar{z}_k^j is the most similar to the neighborhood of $T^j l(x)$ around z_k^j (see Fig. 3.24). This minimum value d_{\min} gives also a confidence measure on the match. The smaller d_{\min} is, the higher our confidence in the match.

Each match between a zero-crossing of $T^j l(x)$ and a zero-crossing of $T^j r(x)$ gives a local estimate of the disparity τ . At the next scale 2^{j+1} we use this local estimate of the disparity in order to constrain the search when trying to find the correspondence between the zero-crossings of $T^{j+1} l(x)$ and the zero-crossings of $T^{j+1} r(x)$. When beginning at the coarser scale 2^{-J} , we do not have any prior estimation of the disparity to constrain the search. This lack of prior information is not a problem since there are only few zero-crossings to match in $T^{-J} l(x)$ and $T^{-J} r(x)$ when J is big enough (see Fig. 3.24).

3.6.2. Discussion of the algorithm and results

The coarse to fine strategy considerably reduces the complexity of the search for a match since we use the matching information at the previous scale to constrain the search at the next scale. This strategy presupposes that we have a good confidence in the matches at the coarser scales, since any error at a coarse scale might propagate at finer scales. At the coarse level we have a higher confidence in the matches because the signals $T^j l(x)$ and $T^j r(x)$ have less distortions (see Fig. 3.23). Indeed, the distortions between the left and right epipolar signals are primarily introduced in the high frequencies of these signals. The distortions are due to the differences in viewing perspectives, to the camera systems noise and to the errors in positioning the epipolar lines in the two images. The matches at the coarser scales are thus more reliable.

In order to avoid side effects, at each scale we did not try to match the zero-crossings at the borders. As we can see from the successive matchings shown in Fig. 3.24, we get a very dense matching on the signal. There are, however, some domains of the signal where we do not match the zero-crossings because there is too much distortion between $T^j l(x)$ and $T^j r(x)$. In these domains, the minimal distance d_{\min} of any pair of matching zero-crossings is large. We have included in our algorithm a confidence threshold c_0 in order to eliminate such matches. If $\frac{1}{d_{\min}} < c_0$, we eliminate the match. As shown in Fig. 3.24, in some domains we are able to find some matches at a coarse scale but not at finer scales, because there is too much high frequency noise. By comparing Fig. 3.22 and Fig. 3.23, we can see that when the left and right signals are locally similar, at each scale $T^j l$ and $T^j r$ are also similar. It is very rare that the discontinuity of the operator T_F , mentioned in paragraph 3.4.3, introduces a noticeable perturbation. As explained in paragraph 3.4.1, the distance d_{z_k} , which must be minimized, is

simple to compute. If we want to speed up the algorithm, we can eliminate any potential match between z_h^i and z_p^i , without computing the distance d_{ij} , when the corresponding energies e_h^i and e_p^i do not have the same sign or have very different values.

As a conclusion we would like to emphasize that such a stereo-matching algorithm is very simple to develop because the EZC representation in itself is well adapted to this pattern recognition problem. We did not try to add any verification procedure on the matches obtained with this algorithm, because our goal was just to demonstrate the efficiency of the representation.

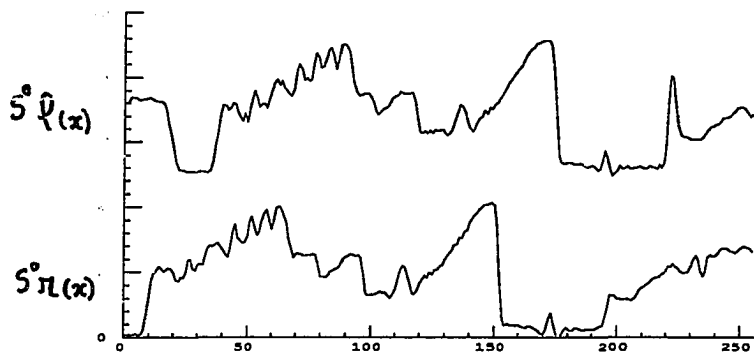


Fig. 3.22 Pair of stereo epipolar scan lines from a real pair of stereo images. The distortion between these two signals is due to the difference of viewing perspective, to the camera noise and to the errors in the computation of the epipolar geometry.

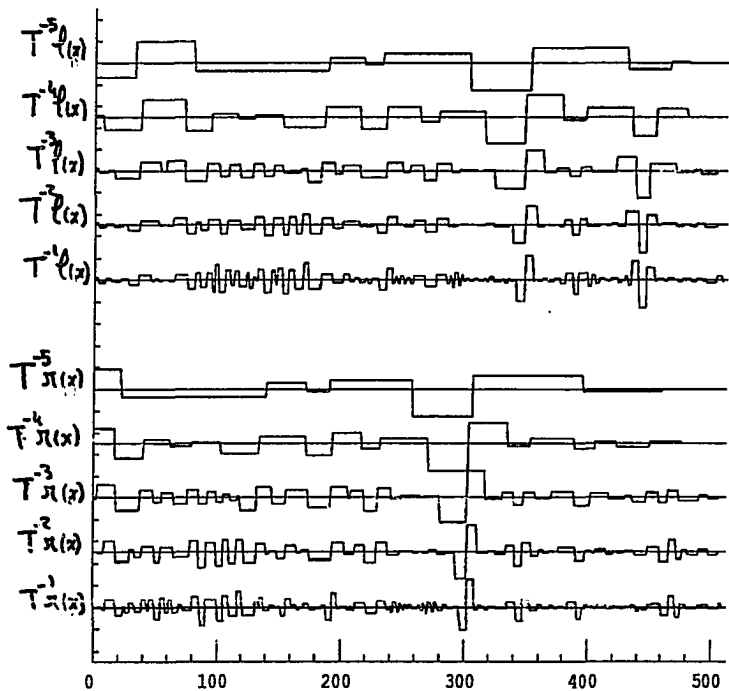


Fig. 3.23 Energy Zero-Crossing representations of the two epipolar lines. The top EZC representation corresponds to the left signal and the bottom one to the right signal. We want to match these representations with a coarse to fine strategy.

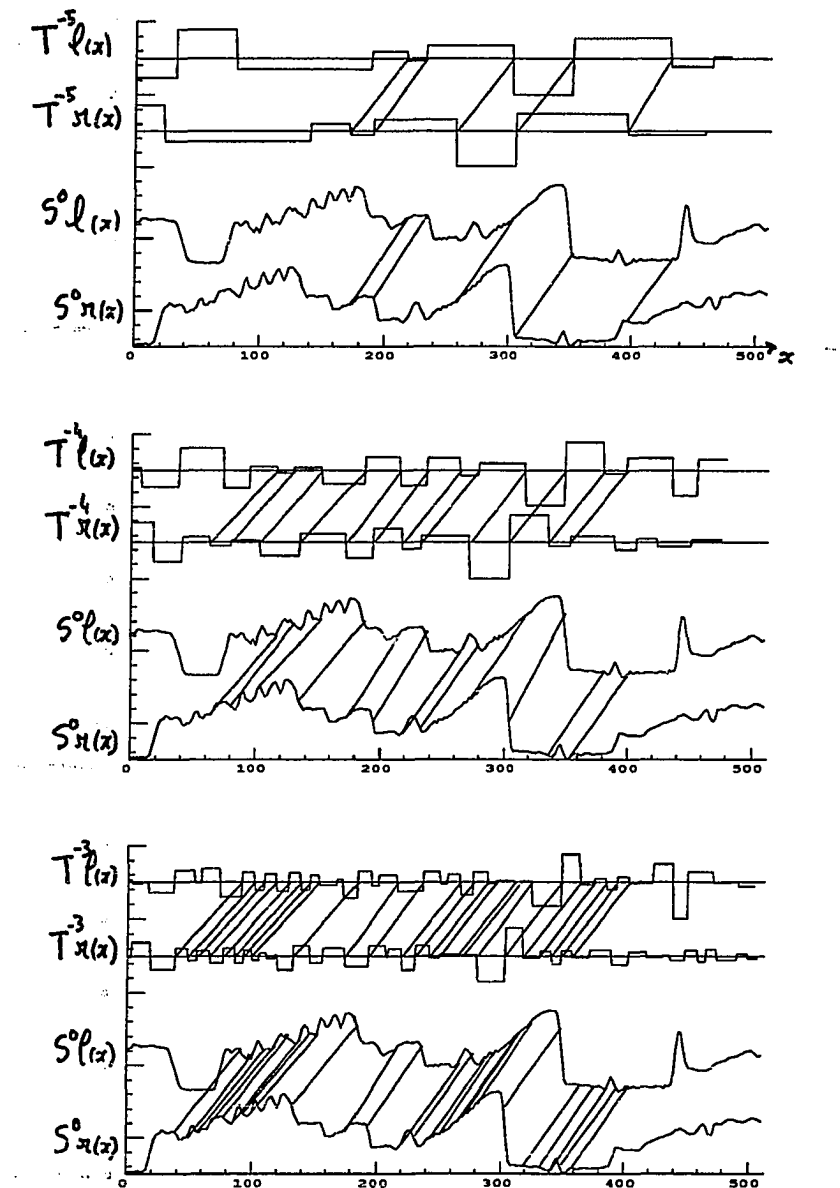


Fig. 3.24 Coarse to fine matching between the zero crossings at the resolutions 2^{-5} , 2^{-4} and 2^{-3} of the EZC representations of a pair of stereo epipolar lines. The top graphs show the zero-crossing matches of the pair of functions $T^j l(x)$ and $T^j r(x)$. The bottom graphs give the corresponding matches of the epipolar lines $l(x)$ and $r(x)$.

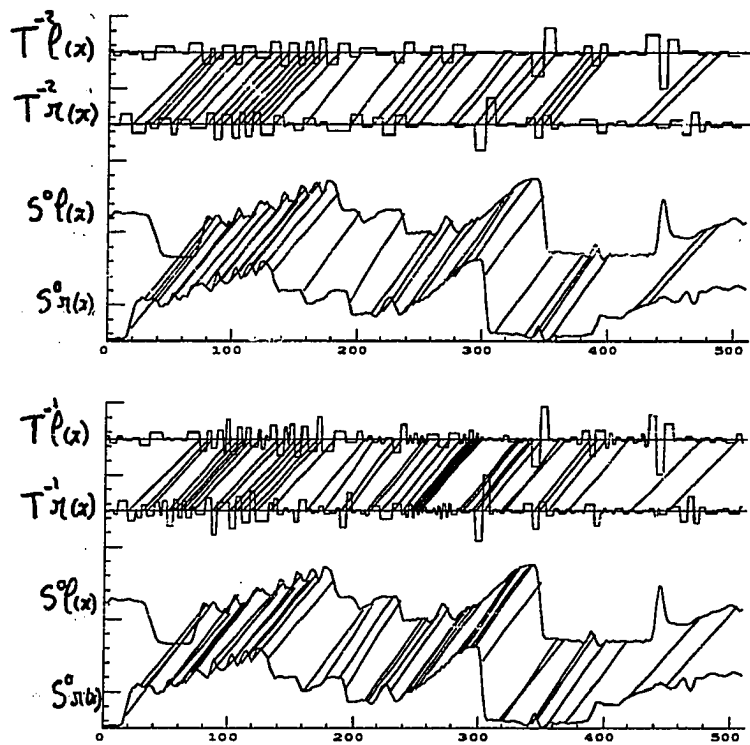


Fig. 3.24 Coarse to fine matching between the zero crossings at the resolutions 2^{-2} and 2^{-1} of the EZC representations of a pair of stereo epipolar lines. The top graphs show the zero-crossing matches of the pair of functions $T^j l(x)$ and $T^j r(x)$. The bottom graphs give the corresponding matches of the epipolar lines $l(x)$ and $r(x)$.

3.7. Dyadic Wavelet transform of images

The dyadic wavelet transform can be generalized to two dimensions by introducing several wavelet functions having different orientation selectivities. In two dimensions, the operator S^j which smoothes any function $f(x,y) \in L^2(\mathbb{R}^2)$ at the scale 2^j is defined by

$$S^j f(x,y) = f * \Theta(x,y) .$$

We can easily extend the analysis we did on one-dimensional smoothing functions and show that in two dimensions the smoothing function $\Theta(x,y)$ must satisfy

$$\|\Theta\| = 1 , \quad (3.91)$$

$$\exists U(\omega_x, \omega_y) \text{ with } \Theta(2\omega_x, 2\omega_y) = U(\omega_x, \omega_y) \Theta(\omega_x, \omega_y) \text{ and } |U(\omega_x, \omega_y)| \leq 1 . \quad (3.92)$$

$$\lim_{\substack{|\omega_x| \rightarrow +\infty \\ |\omega_y| \rightarrow +\infty}} \hat{\Theta}(\omega_x, \omega_y) = 0 , \quad (3.93)$$

$$\lim_{\substack{|\omega_x| \rightarrow 0 \\ |\omega_y| \rightarrow 0}} \hat{\Theta}(\omega_x, \omega_y) = 1 . \quad (3.94)$$

Let $f(x,y) \in L^2(\mathbb{R}^2)$. The details of $f(x,y)$ which appear in $S^{j+1}f(x,y)$ but have been attenuated in $S^j f(x,y)$ are separated into several spatial orientations. For this purpose we decompose $|\hat{\Theta}(\frac{\omega_x}{2}, \frac{\omega_y}{2})|^2 - |\hat{\Theta}(\omega_x, \omega_y)|^2$ into

$$|\hat{\Theta}(\frac{\omega_x}{2}, \frac{\omega_y}{2})|^2 - |\hat{\Theta}(\omega_x, \omega_y)|^2 = \sum_{i=1}^{i_0} |\hat{\Psi}_i(\omega_x, \omega_y)|^2 . \quad (3.95)$$

Each function $\hat{\Psi}_i(\omega_x, \omega_y)$ is the Fourier transform of a function $\Psi_i(x,y)$. The family of functions $\left[\Psi_i(x,y) \right]_{1 \leq i < i_0}$ is called a **dyadic wavelet family**. The following theorem is a simple extension of theorem 3.1.

Theorem 3.3

A family of $L^2(\mathbb{R}^2)$ functions $\{\Psi_i(x,y)\}_{1 \leq i \leq i_0}$ is a dyadic wavelet family if and only if

$$\sum_{i=1}^{i_0} \|\Psi_i\|^2 = 3 \quad \text{and} \quad \forall \omega \in \mathbb{R} \quad \lim_{j \rightarrow +\infty} \sum_{j=i}^J \sum_{i=1}^{i_0} |\hat{\Psi}_i(2^j \omega_x, 2^j \omega_y)|^2 = 1 \quad ,$$

with a uniform convergence for $|\omega_x| \geq 1$ and $|\omega_y| \geq 1$.

Since the smoothing function $\Theta(x,y)$ satisfies equation (3.92), for any $1 \leq i \leq i_0$ we can find a function $G_i(\omega_x, \omega_y)$ such that $\Psi_i(2\omega_x, 2\omega_y) = G_i(\omega_x, \omega_y) \Theta(\omega_x, \omega_y)$ and

$$\sum_{i=1}^{i_0} |G_i(\omega_x, \omega_y)|^2 + |U(\omega_x, \omega_y)|^2 = 1 \quad . \quad (3.97)$$

Each function $\Psi_i(x,y)$ is a band pass filter having a specific spatial orientation selectivity. For example, Fig. 3.25 shows a possible distribution of the frequency support of the functions $\hat{\Psi}_i(\omega_x, \omega_y)$. In Fig. 3.25 all the wavelet $\hat{\Psi}_i(\omega_x, \omega_y)$ can be derived from one another with a simple rotation of their frequency support. This is however not a necessary condition for defining a dyadic wavelet transform.

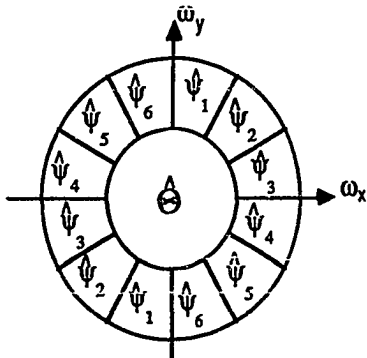


Fig. 3.25 Example of repartition of the support of $\hat{\Theta}(\omega_x, \omega_y)$ and of the wavelets $\hat{\Psi}_i(\omega_x, \omega_y)$ in the frequency plane.

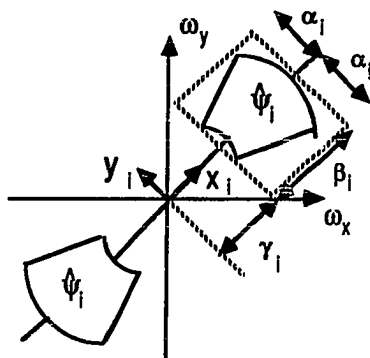


Fig. 3.26 Each filter $\Psi_i(x,y)$ is a band pass filter along the direction \vec{x}_i and a low pass filter along the perpendicular direction \vec{y}_i .

As can be seen in Fig. 3.26, each filter $\Psi_i(x,y)$ is a band-pass filter along a direction \vec{x}_i and a low-pass filter along the perpendicular direction \vec{y}_i .

Let $f(x,y) \in L^2(\mathbb{R}^2)$. The dyadic wavelet transform of $f(x,y)$ at the resolution 2^j and along an orientation i is defined by

$$W_i f(x,y) = f * \Psi_i(x,y) . \quad (3.98)$$

$W_i f(x,y)$ provides the details of the signals which appear at the resolution 2^j in the direction \vec{x}_i . $W_i f(x,y)$ is a low-band signal along the \vec{y}_i direction with an energy mainly concentrated in the frequency interval $[-2^j \alpha_i, 2^j \alpha_i]$ (see Fig. 3.26) and a band limited signal in the \vec{x}_i direction with an energy concentrated in the interval $[-2^j(\beta_i + \gamma_i), -2^j \gamma_i] \cup [2^j \gamma_i, 2^j(\beta_i + \gamma_i)]$.

We call the **two-dimensional infinite dyadic wavelet transform** the sequences of signals

$$\mathbf{W}_I f = \left\{ \left[W_i f(x,y) \right]_{j \in \mathbb{Z}}, \left[W_2 f(x,y) \right]_{j \in \mathbb{Z}}, \dots, \left[W_{l_0} f(x,y) \right]_{j \in \mathbb{Z}} \right\} . \quad (3.99)$$

In two dimensions, an infinite dyadic wavelet transform has the same properties as in one dimension, but it includes a new parameter which is the local orientation of the signal.

• Translation property

Let $g(x,y) = f(x-\tau_x, y-\tau_y)$ be a translation of the signal $f(x,y)$. Then

$$Wif(x,y) = Wif(x-\tau_x, y-\tau_y) . \quad (3.100)$$

• Completeness

$$f(x,y) = \sum_{i=1}^{i_0} \sum_{j \in \mathbb{Z}} Wif(x,y) * \tilde{\psi}_i^j(x,y) . \quad (3.101)$$

• Energy conservation

$$\|f(x,y)\|^2 = \sum_{i=1}^{i_0} \sum_{j \in \mathbb{Z}} \|Wif(x,y)\|^2 . \quad (3.102)$$

We can now define the Energy Zero-Crossing representation of images from this two-dimensional dyadic wavelet representation.

3.8. Energy Zero-Crossing representation of images

As in one dimension, we build a discrete representation from the zero-crossings and the local energies of the dyadic wavelet transform. For now, let us fix the resolution at 2^j and the orientation at i . We saw that $Wif(x,y)$ is a low-band signal along the \vec{y}_i^j direction with an energy mainly concentrated in the frequency interval $[-2^j\alpha_i, 2^j\alpha_i]$ (see Fig. 3.26) and a band limited signal in the \vec{x}_i^j direction with an energy concentrated in the interval $[-2^j(\beta_i + \gamma_i), -2^j\gamma_i] \cup [2^j\gamma_i, 2^j(\beta_i + \gamma_i)]$. Hence, $Wif(x,y)$ is an undulating surface along the \vec{x}_i^j direction and a smooth surface along the \vec{y}_i^j direction (see Fig. 3.27). Fig. 3.31(c) is an example of such surface. Let (x_i, y_i) be the coordinate axes parallel to the vectors \vec{x}_i^j and \vec{y}_i^j (see Fig. 3.27). In order to simplify the notations, from now on, all the functions are written within this system of coordinates. The zero-crossings of the surface $Wif(x_i, y_i)$ correspond to intersection of this surface with the (x_i, y_i) horizontal plane. The intersection curves are smooth functions $x_i = C_n(y_i)$ (see Fig. 3.27), whose Fourier transforms have a frequency support included in the interval $[-2^j\alpha_i, 2^j\alpha_i]$. Fig. 3.31(b) gives an example of zero-crossing curves. In order to build a discrete representation, we sample these zero-crossing curves along the y_i axis, at a rate $\frac{2^j}{d}$ larger than the Nyquist rate : $d < \frac{\pi}{\alpha_i}$. Let us call a row any line of the

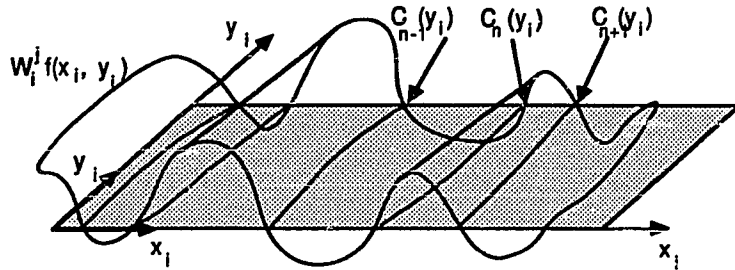


Fig. 3.27. The surface $W/f(x_i, y_i)$ is undulating in the \vec{x}_i direction and is varying smoothly in the \vec{y}_i direction.

(x_i, y_i) plane which is parallel to the x_i axis, and a row-sampling at a rate $\frac{2^j}{d}$ an infinite set of rows $\left[R_m \right]_{m \in \mathbb{Z}}$ with a constant interval $2^{-j}d$ between each row (see Fig. 3.28). The Cartesian equation of the row R_m is $y_i = m2^{-j}d$. We can derive from the Nyquist theorem that the zero crossing curves C_n are characterized by the positions of their intersections with each row R_m of a row-sampling with $d < \frac{\pi}{\alpha_i}$ (see Fig. 3.28). Let z_n^m be the abscissa of the intersection between the zero-crossing curve C_n and R_m (see Fig. 3.28). Let S_n^m be the surface of the (x_i, y_i) plane which is between the curves $C_{n-1}(y_i)$ and $C_n(y_i)$ for $y_i \in [(m-\frac{1}{2})d2^{-j}, (m+\frac{1}{2})d2^{-j}]$ (see Fig. 3.28). We denote by e_n^m the local energy of the arch of surface of $W/f(x_i, y_i)$, which is over the surface S_n^m :

$$e_n^m = \left[\int \int |W/f(x_i, y_i)|^2 dx_i dy_i \right]^{\frac{1}{2}} \cdot \text{sign}(W/f) . \quad (3.103)$$

The energy e_n^m has the same sign as $W/f(x_i, y_i)$ for $(x_i, y_i) \in S_n^m$.

In two dimensions, for each orientation i and resolution 2^j , the Energy Zero-Crossing representation is characterized by the positions of the zero-crossings $\left[z_n^m \right]_{(n,m) \in \mathbb{Z}^2}$ and the values of the local energies $\left[e_n^m \right]_{(n,m) \in \mathbb{Z}^2}$. These sequences of zero-crossings and local energies can be characterized by a piecewise constant surface defined below. Let \tilde{S}_n^m be the rectangle defined by $x_i \in [z_{n-1}^m, z_n^m]$ and $y_i \in [(m-\frac{1}{2})d2^{-j}, (m+\frac{1}{2})d2^{-j}]$ (see Fig. 3.28).

$$\forall (n, m) \in \mathbb{Z}^2, \quad \forall (x_i, y_i) \in \tilde{S}_n^m, \quad T_l f(x_i, y_i) = \frac{e_n^m}{\sqrt{d} 2^{-j_d} (z_n^m - z_{n-1}^m)} \quad . \quad (3.104)$$

$T_l f(x_i, y_i)$ has the same zero-crossing as $W_l f(x_i, y_i)$ along each row R_m of the row-sampling and has the same local energy values (see Fig. 3.29). Fig. 3.31(d) gives an example of a surface $T_l f(x_i, y_i)$ derived from $W_l f(x_i, y_i)$.

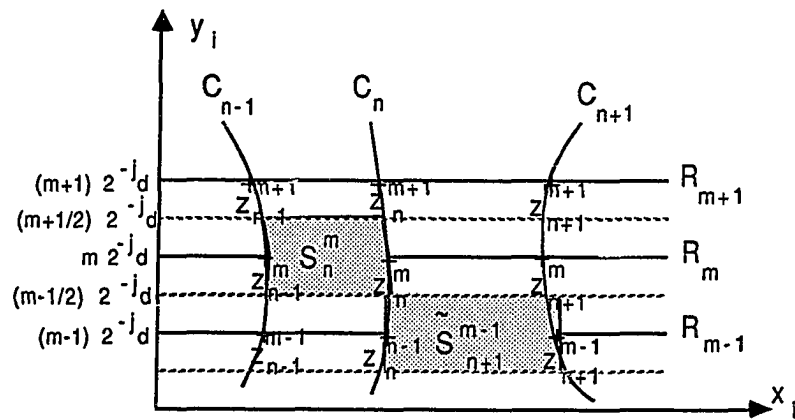


Fig. 3.28. Zero-crossing curves intersecting a row-sampling in the (x_i, y_i) plane.

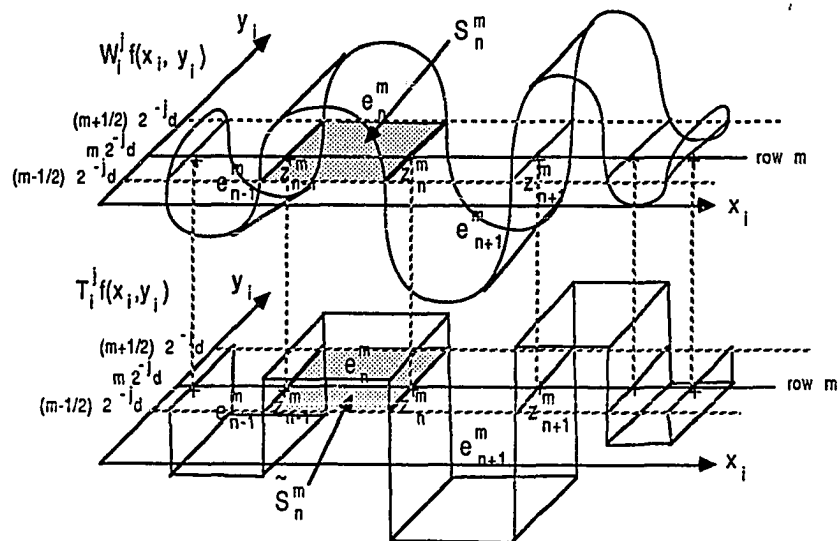


Fig. 3.29 Illustration of the definition of $T_l f(x_i, y_i)$ from $W_l f(x_i, y_i)$.

We call two-dimensional Energy Zero-Crossing representation the set of piecewise constant functions

$$T_{lf} = \left\{ \left[T_{1f}(x, y) \right]_{j \in \mathbb{Z}}, \left[T_{2f}(x, y) \right]_{j \in \mathbb{Z}}, \dots, \left[T_{if}(x, y) \right]_{j \in \mathbb{Z}} \right\} \quad . \quad (3.105)$$

Since $T_{if}(x_i, y_i)$ is constant when x_i is fixed and $y_i \in [(m - \frac{1}{2})2^{-j}d, (m + \frac{1}{2})2^{-j}d]$, the piecewise constant surface $T_{if}(x_i, y_i)$ can also be characterized by the set of piecewise constant curves $T_{if^m}(x_i) = T_{if}(x_i, m2^{-j}d)$. Hence, we can perform any two-dimensional computation on $T_{if}(x_i, y_i)$ as a sum on all the rows R_m of one dimensional computations on the functions $T_{if^m}(x_i)$. The functions $T_{if^m}(x_i)$ are identical to the piecewise constant functions of a one-dimensional EZC representation. A two-dimensional Energy Zero-Crossing representation can essentially be viewed as a set of one-dimensional EZC representations with two parameters corresponding to the local orientation of the signal i and the row m which is considered.

• Energy conservation

It is clear that the total energy of $T_{if}(x_i, y_i)$ is the same as $W_{if}(x_i, y_i)$, since they have the same local energies :

$$\|T_{if}\|^2 = \|W_{if}\|^2 = \sum_{m \in \mathbb{Z}} \sum_{n \in \mathbb{Z}} |e_n^m|^2 \quad . \quad (3.106)$$

An energy conservation equation can thus be derived from the energy conservation equation (3.102) on a two-dimensional dyadic wavelet transform :

$$\|f(x, y)\|^2 = \sum_{i=1}^{i_0} \sum_{j \in \mathbb{Z}} \|T_{if}(x, y)\|^2 \quad . \quad (3.107)$$

• Translation property

If the signal $f(x, y)$ is translated along the \vec{x}_i direction, $T_{if}(x_i, y_i)$ is exactly translated. Indeed, the zero-crossings and local energies are translating. If $f(x, y)$ is translated along the \vec{y}_i direction, $T_{if}(x_i, y_i)$ is translated with a small error depending upon the size of the sampling interval between each row. Indeed, we have a sampling distortion effect due to the row-sampling. However, this sampling distortion is much smaller than the sampling distortion discussed in chapter 1 because along the y_i direction, $W_{if}(x_i, y_i)$ is low-band signal. If the

sampling rate of the row is at least twice the Nyquist frequency ($d < \frac{\pi}{2\alpha_i}$) , this error is negligible in practical computations. In two dimensions, the Energy Zero-Crossing representation is therefore translating along any direction with a good approximation.

• Distance

In two dimensions, the distance on a EZC representation is a simple extension of the one-dimensional distance. For any $f(x,y) \in L^2(\mathbb{R}^2)$ and $g(x,y) \in L^2(\mathbb{R}^2)$,

$$d(T_I f, T_I g) = \sum_{i=1}^{i_0} \sum_{j \in \mathbb{Z}} \|T_I f(x_i, y_i) - T_I g(x_i, y_i)\|^2. \quad (3.108)$$

As explained previously, this two-dimensional computation can be reduced to a one-dimensional computation by observing that

$$\|T_I f(x_i, y_i) - T_I g(x_i, y_i)\|^2 = 2^{-j} d \sum_m \|T_I^m f(x_i) - T_I^m g(x_i)\|^2. \quad (3.109)$$

As we have seen for a one-dimensional EZC representation, the value of $\|T_I^m f(x_i) - T_I^m g(x_i)\|^2$ is easy to compute since $T_I^m f(x_i)$ and $T_I^m g(x_i)$ are one-dimensional piecewise constant functions.

For local matching, we can also define a local distance about a point (a,b) by generalizing the local one-dimensional distance. Let (a_i, b_i) be the coordinates of the point (a,b) in the system axis (x_i, y_i) and σ_i be the size of the interval on which the energy of $\Psi_i(x_i, y_i)$ is mainly concentrated .

$$\int_{-a_i}^{a_i} \int_{-b_i}^{b_i} |\Psi_i(x_i, y_i)|^2 dx_i dy_i \approx \int_{-\infty}^{\infty} \int_{-\infty}^{\infty} |\Psi_i(x_i, y_i)|^2 dx_i dy_i. \quad (3.110)$$

The local distance around (a,b) is defined by :

$$d_{(a,b)}(T_I f, T_I g) = \sum_{i=1}^{i_0} \sum_{j \in \mathbb{Z}} \int_{a_i - \sigma_i 2^{-j}}^{a_i + \sigma_i 2^{-j}} \int_{b_i - \sigma_i 2^{-j}}^{b_i + \sigma_i 2^{-j}} (T_I f(x_i, y_i) - T_I g(x_i, y_i))^2 dx_i dy_i. \quad (3.111)$$

This local distance computation also can be reduced to a one-dimensional computation by observing that

$$2^{-j} d \sum_{\frac{b_i 2^j - \sigma_i}{d} \leq m \leq \frac{b_i 2^j + \sigma_i}{d}} \int_{a_i - \sigma_i 2^{-j}}^{a_i + \sigma_i 2^{-j}} (T_i f(x_i, y_i) - T_i g(x_i, y_i))^2 dx_i dy_i =$$

$$\int_{a_i - \sigma_i 2^{-j}}^{a_i + \sigma_i 2^{-j}} (T_i^m f(x_i) - T_i^m g(x_i))^2 dx_i .$$

We do not discuss the completeness and the stability of the two-dimensional EZC representation in this dissertation, since we have not yet implemented the reconstruction algorithm.

3.8.1. Example of two-dimensional Energy Zero-Crossing representation

In this paragraph, we describe a simple two-dimensional dyadic wavelet representation having four orientation tunings : horizontal , vertical and the two diagonals. From this dyadic wavelet representation we can then derive the corresponding Energy Zero-Crossing representation. This representation is a separable extension of the one-dimensional dyadic wavelet representation. Let $\theta(x)$ be a one-dimensional smoothing function and let $U(\omega)$ be such that

$$\hat{\theta}(2\omega) = U(\omega) \hat{\theta}(\omega) .$$

Let $\psi(x)$ be a dyadic wavelet associated with $\theta(x)$ and $G(\omega)$ be such that

$$\hat{\psi}(2\omega) = G(\omega) \hat{\theta}(\omega) \quad \text{and} \quad |G(\omega)|^2 + |U(\omega)|^2 = 1 .$$

The function $\Theta(x,y) = \theta(x) \theta(y)$ is a two-dimensional separable smoothing function. From such a smoothing function we can build a family of four dyadic wavelets $\left[\Psi_i(x,y) \right]_{1 \leq i \leq 4}$.

Equation (3.97) shows that the Fourier transform of the dyadic wavelets $\Psi_i(x,y)$ must satisfy

$$\hat{\Psi}_i(\omega_x, \omega_y) = G_i(\omega_x, \omega_y) \Theta(\omega_x, \omega_y) \quad \text{for } 1 \leq i \leq 4 \quad \text{with}$$

$$\sum_{i=1}^{i_0} |G_i(\omega_x, \omega_y)|^2 + |U(\omega_x, \omega_y)|^2 = 1 . \quad (3.113)$$

Let us describe a possible choice of functions $G_i(\omega_x, \omega_y)$. Let $\gamma(\omega_x, \omega_y)$ be the 2π periodic function in ω_x and ω_y such that

$$\begin{cases} \gamma(\omega_x, \omega_y) = 0 & \text{if } (\omega_x, \omega_y) \in [0, \pi] \times [0, \pi] \cup [-\pi, 0] \times [-\pi, 0] \\ \gamma(\omega_x, \omega_y) = 1 & \text{if } (\omega_x, \omega_y) \in [-\pi, 0] \times [0, \pi] \cup [0, \pi] \times [-\pi, 0] \end{cases} .$$

The functions $G_i(\omega_x, \omega_y)$ are defined by :

$$G_1(\omega_x, \omega_y) = U(\omega_x) G(\omega_y) \quad (3.114)$$

$$G_2(\omega_x, \omega_y) = G(\omega_x) U(\omega_y) \quad (3.115)$$

$$G_3(\omega_x, \omega_y) = G(\omega_x) G(\omega_y) \gamma(\omega_x, \omega_y) \quad (3.116)$$

$$G_4(\omega_x, \omega_y) = G(\omega_x) G(\omega_y) \gamma(-\omega_x, \omega_y) . \quad (3.117)$$

One can easily show that these functions satisfy equation (3.113). The corresponding wavelet $\Psi_1(x, y)$ is a low-pass filter in the horizontal direction and a band-pass filter in the vertical direction. $\Psi_2(x, y)$ is a low-pass filter in the vertical direction and a band-pass filter in the horizontal direction. $\Psi_3(x, y)$ is a low-pass filter along the first diagonal and a band-pass filter along the second diagonal. $\Psi_4(x, y)$ is a low-pass filter along the second diagonal and a band-pass filter along the first diagonal. Fig. 3.30 is an approximate diagram of the frequency support of the Fourier transform of each wavelet.

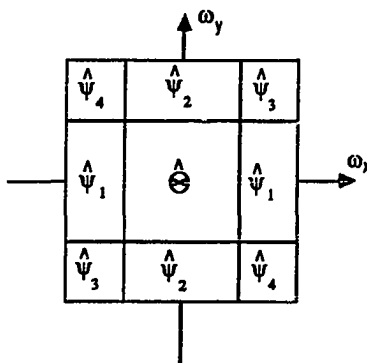
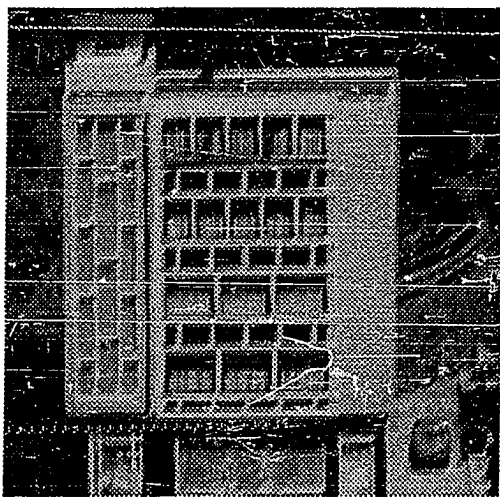


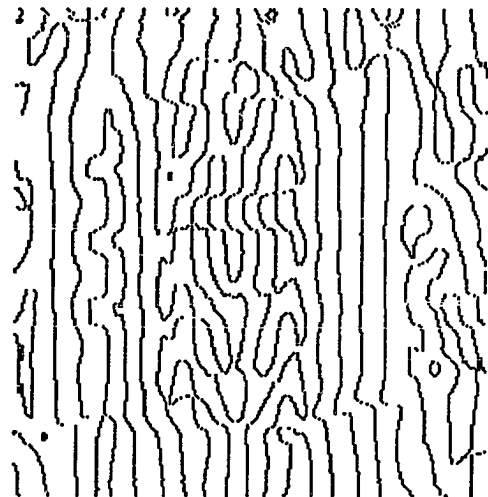
Fig. 3.30 Repartition in the frequency plane of the support of the functions $\hat{\Psi}_i(\omega_x, \omega_y)$, for $1 \leq i \leq 4$.

To build the EZC representation in two dimensions, we first need to define a row-sampling of the (x, y) plane for each resolution 2^j and orientation i . Then along each row of such a row-sampling we must compute a uniform sampling of the curves $W/f(x, y)$ in order to

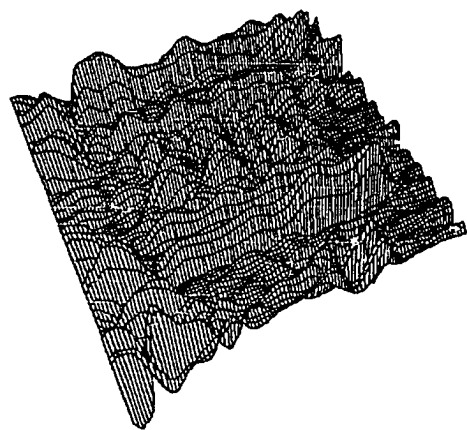
estimate the positions of the zero-crossings and the values of the local energies. The image $f(x,y)$ shown in Fig. 3.31(a) is a 256 by 256 pixel image. Fig. 3.31(b) gives the zero-crossing curves of $W_1^{-4}(x,y)$. We have included all the zero-crossings, including the ones which have a very low energy, so that there are many spurious zero-crossings which do not correspond to significant vertical edges. Fig. 3.31(c) shows the surface $W_1^{-4}(x,y)$, and Fig. 3.31(d), the corresponding function $T_1^{-4}(x,y)$. $T_1^{-4}(x,y)$ was computed with a row-sampling at a rate twice the Nyquist rate (32 rows). It is characterized by the positions of the zero-crossings along each of these rows and the corresponding local energies.



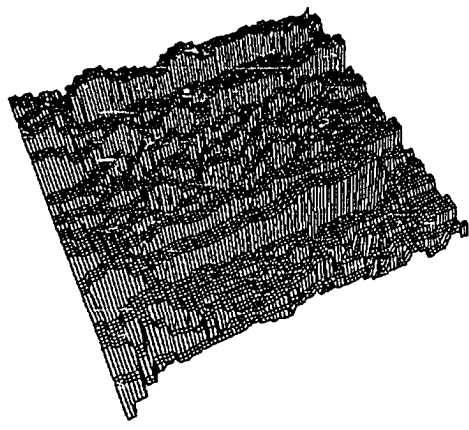
(a)



(b)



(c)



(d)

Fig. 3.31. (a) Original image $f(x,y)$. (b) Zero-crossing curves $C_n(y)$ of $W_1^{-4}f(x,y)$ (resolution 2^{-4} and vertical direction). (c) Graph of the surface $W_1^{-4}f(x,y)$. (d) Graph of the surface $T_1^{-4}f(x,y)$.

3.8.2. Application of the Energy Zero-Crossings representation to image segmentation and pattern matching

In this paragraph, we briefly discuss the applications of this representation to pattern matching and image segmentation. The EZC representation has the important properties required for developing pattern matching algorithms. It is complete, translating, based upon a multiscale decomposition and provides the positions of the discontinuities. The stereo-matching algorithm shows that coarse to fine strategies can easily be implemented with such a representation. A classical approach to fast pattern recognition consists of characterizing a pattern with only a few remarkable features. These features might not provide a complete representation but should be enough for discriminating any given pattern among all others. The problem is to automatically extract these features and then be able to compare them from pattern to pattern. With an EZC representation, these features can be defined for each resolution and orientation as the set of zero-crossings and energies $(z_{n-1}^m, z_n^m), e_n^m$ such that $|e_n^m|$ has a large value. These features correspond to the most important structures of the signal appearing at each resolution 2^j , within the direction \vec{x}_i . We can then compare these features for different patterns by using the distance defined by equation (3.111).

The numerous techniques available in image segmentation can be divided into two dual approaches. The first one consists of finding the edges of the image and then defining a region as a part of the image enclosed inside a connected edge border. On the contrary, the other approach is not based upon discontinuities detection but upon local similarities. Two local areas of an image are part of the same region (or texture) if they have the same textural properties. Regions are grown by grouping the local domains which are similar with respect to the texture similarity criteria. Several researchers [46] have tried to measure texture similarities from the energy output of oriented band pass filters. The EZC representation is based upon such local energy values, within the borders provided by zero-crossings. We thus have a representation which can integrate the two approaches by providing at the same time the locations of the discontinuities and the energies which can be used for similarity measurements.

CONCLUSION AND CONTRIBUTIONS

In this dissertation we have studied a general purpose multiresolution image representation for computer vision applications. In chapter 1 we have described a mathematical model which enables us to understand the concept of resolution. We have seen that it is possible to compute the difference of information between signals approximated at different resolutions. We have then derived an orthogonal multiresolution representation called an orthogonal wavelet representation. This representation corresponds to an expansion of the original continuous signal in a wavelet orthonormal basis. It can also be interpreted as a decomposition of the signal in a set of independent frequency channels having spatial orientation tunings. The wavelet representation is efficiently computed with a pyramidal algorithm based on convolutions with conjugate mirror filters. The original signal can be also reconstructed with a similar algorithm. The numerical stability is well illustrated by the quality of the reconstruction. The orientation selectivity of this representation is useful for many applications. We have discussed in particular the application of the wavelet representation to data compression, texture discrimination and Brownian fractal analysis.

We have described in chapter 2 the mathematical foundations of the multiresolution model. The multiresolution approach to wavelets enables us to characterize the functions of $L^2(\mathbb{R})$ which generate an orthonormal wavelet basis. In particular I. Daubechies has shown that one could define some wavelet of compact support with such an approach. This model has been generalized by Y. Meyer fonctions splines in $L^2(\mathbb{R}^n)$ and then by S. Jaffard and Y. Meyer jaffard ouverts to $L^2(\Omega)$ where Ω is an open subset of \mathbb{R}^n .

However, the orthogonal wavelet representation is not well adapted for pattern matching applications since it does not translate when the signal translates. In chapter 3, we have developed a nonlinear multiscale transform which does translate when the signal translates. It is based on another class of wavelet functions called dyadic wavelets. In the first part of this chapter we have studied the mathematical properties of the dyadic wavelet representation. We have shown that we could define a new signal representation from the zero-crossings and local

energy values of the dyadic wavelet representation. The Energy Zero-Crossing representation admits a simple metric for pattern recognition applications. It has a multiscale organization and provides the locations of the signal "edges" at each scale. We have described an iterative algorithm for reconstructing a signal from its EZC representation. The convergence of the algorithm gives an experimental proof of the completeness of this representation. The mathematical proof of the completeness remains an open problem. We have described the numerical implementation of all our algorithms. In particular, we have detailed the implementation of a discrete dyadic wavelet transform with a pyramidal algorithm of complexity $n \log(n)$. A similar algorithm has been described for implementing an inverse dyadic wavelet transform. We have developed a coarse to fine stereo-matching algorithm to illustrate the application of this decomposition to pattern recognition. The simplicity and the efficiency of this matching algorithm shows that the EZC representation is indeed well adapted for pattern recognition problems. This representation has been extended to two-dimensional signals, but we did not implement the reconstruction algorithm in two dimensions.

We believe that the Energy Zero-Crossing decomposition can provide a general purpose low-level image representation for computer vision applications. An important test would be to show that this representation yields a simple approach to the image segmentation problem. For this purpose we need to develop a texture model based on the EZC representation, which is one of the future orientations of our research. Another interesting development of this work concerns the application of the one-dimensional Energy Zero-Crossing representation to pattern recognition in speech and seismic waves signals.

Appendix A

In this appendix we describe a class of multiresolution approximations of $L^2(\mathbb{R})$ studied by P.Lemarie [25] and G.Battle [2]. These multiresolution approximations are built from polynomial splines of order $2p+1$. The vector space \mathbf{V}_0 is the vector space of all the functions of $L^2(\mathbb{R})$ which are p times continuously differentiable and equal to a polynomial of order $2p+1$ on each interval $[k, k+1]$, for any $k \in \mathbb{Z}$. The other vector spaces \mathbf{V}_j are derived from \mathbf{V}_0 with property (1.3). P. Lemarie has shown that the scaling function associated with such a multiresolution approximation is given by

$$\hat{\phi}(\omega) = \frac{1}{\omega^n \sqrt{\Sigma_{2n}(\omega)}} \quad \text{where } n = 2 + 2p . \quad (1.59)$$

The function $\Sigma_n(\omega)$ is given by

$$\Sigma_n(\omega) = \sum_{-\infty}^{+\infty} \frac{1}{(\omega + 2k\pi)^n} . \quad (1.60)$$

We can compute a closed form of $\Sigma_n(\omega)$ by calculating the derivatives of order $n-2$ of the equation

$$\Sigma_2(\omega) = \frac{1}{4\sin^2(\omega/2)} .$$

The function $H(\omega)$ of theorem 1.2 is given by

$$H(\omega) = \sqrt{\frac{\Sigma_{2n}(\omega)}{2^{2n} \Sigma_{2n}(2\omega)}} . \quad (1.61)$$

The Fourier transform of the corresponding orthonormal wavelet can be derived from equation (1.22) of theorem 1.3 :

$$\hat{\psi}(\omega) = e^{-i\frac{\omega}{2}} \bar{H}\left(\frac{\omega}{2} + \pi\right) \hat{\phi}\left(\frac{\omega}{2}\right) = \frac{e^{-i\frac{\omega}{2}}}{\omega^n} - \frac{\sqrt{\Sigma_{2n}\left(\frac{\omega}{2} + \pi\right)}}{\sqrt{\Sigma_{2n}(\omega) \Sigma_{2n}\left(\frac{\omega}{2}\right)}} . \quad (1.62)$$

P. Lemarie has shown that $\phi(x) = O(e^{-\alpha_n|x|})$, where α_n is a positive coefficient that depends on n .

The scaling function shown in Fig. 1.1 was obtained with $p = 1$, and thus $n = 4$. Let

$$D_1(\omega) = 5 + 30 \left(\cos \frac{\omega}{2}\right)^2 + 30 \left(\sin \frac{\omega}{2}\right)^2 \left(\cos \frac{\omega}{2}\right)^2 \quad \text{and}$$

$$D_2(\omega) = 2 \left(\sin \frac{\omega}{2}\right)^4 \left(\cos \frac{\omega}{2}\right)^2 + 70 \left(\cos \frac{\omega}{2}\right)^4 + \frac{2}{3} \left(\sin \frac{\omega}{2}\right)^6 .$$

The function $\Sigma_8(\omega)$ is given by

$$\Sigma_8(\omega) = \frac{105 \left(\sin \frac{\omega}{2}\right)^8}{D_1(\omega) + D_2(\omega)} .$$

In this particular case, the vector spaces V_j are composed of cubic spline polynomials.

Appendix B

This appendix gives a proof of theorem 3.1. We have already shown that if $\psi(x)$ is a wavelet, it must satisfy the conditions of Lemma 1. Conversely, let $\psi(x)$ be a function satisfying the condition of the lemma. Let $\hat{\theta}(\omega)$ be a function defined by $\hat{\theta}(\omega) \geq 0$ and

$$|\hat{\theta}(\omega)|^2 = \sum_{j=1}^{+\infty} |\hat{\psi}(2^j \omega)|^2 . \quad (3.118)$$

The functions $\hat{\theta}(\omega)$ and $\hat{\psi}(\omega)$ satisfy

$$|\psi(\omega)|^2 = |\hat{\theta}(\frac{\omega}{2})|^2 - |\hat{\theta}(\omega)|^2 .$$

In order to prove that $\psi(x)$ is a wavelet, we show that $\hat{\theta}(\omega)$ is the Fourier transform of a scaling function. Let us prove first that $\hat{\theta}(\omega)$ is square integrable :

$$\int_{-\infty}^{+\infty} |\hat{\theta}(\omega)|^2 d\omega = \int_{-\infty}^{+\infty} \sum_{j=1}^{+\infty} |\hat{\psi}(2^j \omega)|^2 d\omega = 2\pi \sum_{j=1}^{+\infty} 2^{-j} \|\psi\|^2 = 2\pi . \quad (3.119)$$

The function $\hat{\theta}(\omega)$ is thus a square integrable function. It defines the Fourier transform of a function $\theta(x)$ and with Parseval's theorem we can derive that $\|\theta\| = 1$. By scaling equation (3.118) by 2^J , we get

$$\forall \omega \in \mathbb{R} , \quad |\hat{\theta}(2^J \omega)|^2 = \sum_{j=J}^{+\infty} |\hat{\psi}(2^j \omega)|^2 .$$

Since $\sum_{j=J}^{+\infty} |\hat{\psi}(2^j \omega)|^2$ converges uniformly when J tends to $+\infty$, we have

$$\lim_{|\omega| \rightarrow 0} |\hat{\theta}(\omega)| = 1 \quad \text{and}$$

$$\lim_{|\omega| \rightarrow \infty} |\hat{\theta}(\omega)| = 0 .$$

Since $\hat{\theta}(\omega) \geq 0$, it satisfies the limit conditions (3.8) and (3.9) of a smoothing function. Finally, $\hat{\theta}(\omega)$ clearly satisfies the causality condition of a smoothing function since

$$|\hat{\theta}(2\omega)|^2 = \sum_{j=2}^{+\infty} |\hat{\psi}(2^j \omega)|^2 \leq |\hat{\theta}(\omega)|^2 .$$

The inverse Fourier transform of $\hat{\theta}(\omega)$ is thus a smoothing function. This concludes the proof of theorem 3.1.

Appendix C

This appendix gives a proof to lemma 3.1 and shows that the converse is not true. In order to simplify the proof we choose $j = 0$. It can then be easily extended for any $j \in \mathbb{Z}$. By taking the Fourier transform of equation (3.27), we can show that the Fourier transform of any function $f^*(x) \in \mathbf{V}_0$ is given by

$$f^*(\omega) = \xi(\omega) \sum_{n=-\infty}^{+\infty} \alpha_n e^{-in\omega}. \quad (3.120)$$

Equation (3.28) shows that $f^*(\omega)$ can be written

$$\hat{f}^*(\omega) = \hat{\psi}(\omega) \hat{f}(\omega) , \text{ where } \hat{f}(\omega) = \hat{\nu}(2^{-j}\omega) \sum_{n=-\infty}^{+\infty} \alpha_n e^{-in\omega}. \quad (3.121)$$

In order to prove equation (3.29), we must show that $\hat{f}(\omega) \in \mathbf{L}^2(\mathbb{R})$. Let us compute the integral of $|\hat{f}(\omega)|^2$:

$$\int_{-\infty}^{+\infty} |\hat{f}(\omega)|^2 d\omega = \sum_{k=-\infty}^{+\infty} \int_{k2\pi}^{(k+1)2\pi} |\hat{f}(\omega)|^2 d\omega = \sum_{k=-\infty}^{+\infty} \int_{k2\pi}^{(k+1)2\pi} \left| \sum_{n=-\infty}^{+\infty} \alpha_n e^{-in\omega} \right|^2 |\nu(\omega)|^2 d\omega.$$

Since $\sum_{n=-\infty}^{+\infty} \alpha_n e^{-in\omega}$ is 2π periodic, and since we know that $\exists C > 0$ such that $|\nu(\omega)|^2 < \frac{C}{1+\omega^2}$, we have

$$\int_{-\infty}^{+\infty} |\hat{f}(\omega)|^2 d\omega = \int_0^{2\pi} \left| \sum_{n=-\infty}^{+\infty} \alpha_n e^{-in\omega} \right|^2 \sum_{k=-\infty}^{+\infty} |\nu(\omega + k2\pi)|^2 \leq \sum_{n=-\infty}^{+\infty} |\alpha_n|^2 \sum_{k=-\infty}^{+\infty} \frac{C}{(1+2k\pi)^2}.$$

This equation shows that $\hat{f}(\omega)$ is square-integrable. It thus defines the Fourier transform of a function $f(x) \in \mathbf{L}^2(\mathbb{R})$. Since $f^*(x) = S^j f(x)$, this concludes the proof of lemma 3.1.

Conversely, not every function $f(x) \in \mathbf{L}^2(\mathbb{R})$ verifies $S^j f(x) \in \mathbf{V}_j$. In order to satisfy such a property, the Fourier transform of $f(x)$ must satisfy equation (3.121). The inverse Fourier transform of this equation can be written

$$f(x) = \sum_{n=-\infty}^{+\infty} \alpha_n v(x-n). \quad (3.122)$$

The function $f(x)$ must therefore be in the vector space generated by the family of functions $\{v(x-n)\}_{n \in \mathbb{Z}}$.

Appendix D

This appendix gives the proof of theorem 3.2. This theorem is proved for $j = 0$. We can generalize the result for any $j \in \mathbf{Z}$ by scaling the functions $\phi(x)$ and $\rho(x)$ by a factor 2^j . Let us express equation (3.31) for $f(x) = \phi(x)$:

$$\phi(x) = \sum_{n=-\infty}^{+\infty} \phi(n) \rho(x - n) . \quad (3.123)$$

If we take the Fourier transform of this equation, by applying the Poisson formula we get

$$\hat{\phi}(\omega) = \sum_{n=-\infty}^{+\infty} \hat{\phi}(\omega + 2n\pi) \hat{\rho}(\omega) . \quad (3.124)$$

The Fourier transform of $\rho(x)$ must therefore verify

$$\hat{\rho}(\omega) = \frac{\hat{\phi}(\omega)}{\sum_{n=-\infty}^{+\infty} \hat{\phi}(\omega + 2n\pi)} . \quad (3.125)$$

This equation defines a function in $L^2(\mathbf{R})$ since $c_2 \geq \sum_{n=-\infty}^{+\infty} \hat{\phi}(\omega + 2n\pi) \geq c_1$.

Let us now suppose that $\rho(x)$ is a function whose Fourier transform is defined by equation (3.125). We want to prove that property (3.31) is indeed satisfied. Since $\sum_{n=-\infty}^{+\infty} \hat{\rho}(\omega + 2n\pi) = 1$, by applying the Poisson formula we derive that

$$\forall n \in \mathbf{Z} \quad \rho(n) = \begin{cases} 1 & \text{if } n = 0 \\ 0 & \text{if } n \neq 0 \end{cases} . \quad (3.126)$$

By reversing the derivation steps of equations (3.124) and (3.125) we can also show that $\phi(x)$ and $\rho(x)$ satisfy equation (3.123). Hence, for any $k \in \mathbf{Z}$, the function $\phi(x - k)$ can be decomposed on the family of functions $\{\rho(x - n)\}_{n \in \mathbf{Z}}$. Since $\{\phi(x - k)\}_{k \in \mathbf{Z}}$ is a basis of V_0 , any function $f(x) \in V_0$ can thus be decomposed the family of the functions $\{\rho(x - n)\}_{n \in \mathbf{Z}}$:

$$\exists (\alpha_n)_{n \in \mathbf{Z}} , \quad f(x) = \sum_{n=-\infty}^{+\infty} \alpha_n \rho(x - n) .$$

Since $\rho(x)$ satisfies property (3.126), for all $n \in \mathbf{Z}$, $\alpha_n = f(n)$.

Appendix E

This appendix gives a proof of lemma 3.2.

Proof of equation (3.79) : Let $\hat{W}^j f_d(\omega)$ be the Fourier series of the discrete signal $W^j f_d$ defined by equation (89) :

$$\hat{W}^j f_d(\omega) = \sum_{n \in \mathbb{Z}} W^j f(n 2^{-j_0-j}) e^{-in 2^{-j_0-j}\omega}. \quad (3.127)$$

Since $W^j f(n 2^{-j_0-j}) = f * \psi^j(n 2^{-j_0-j})$, by applying the Poisson formula we can easily derive that

$$\begin{aligned} \hat{W}^j f_d(\omega) &= \hat{f}(\omega) \hat{\psi}(2^{-j}\omega) * 2^{j_0+j} \sum_{n \in \mathbb{Z}} \delta(\omega + n 2\pi 2^{j_0+j}) \quad \text{so} \\ \hat{W}^j f_d(\omega) &= 2^{j_0+j} \sum_{n \in \mathbb{Z}} \hat{f}(\omega + n 2\pi 2^{j_0+j}) \hat{\psi}(2^{-j}\omega + n 2\pi 2^{j_0}). \end{aligned} \quad (3.128)$$

Equation (3.10) yields

$$\hat{\psi}(2^{-j}\omega + n 2\pi 2^{j_0}) = G(2^{-j-1}\omega + n\pi 2^{j_0}) \hat{\theta}(2^{-j-1}\omega + n\pi 2^{j_0}).$$

Since $G(\omega)$ is $2^{j_0}\pi$ periodic,

$$\hat{W}^j f_d(\omega) = 2^{j_0+j} G(2^{-j-1}\omega) \sum_{n \in \mathbb{Z}} \hat{f}(\omega + n 2\pi 2^{j_0+j}) \hat{\theta}(2^{-j-1}\omega + n\pi 2^{j_0}). \quad (3.129)$$

Let us now define the Fourier series $\hat{S}^j f_d(\omega)$ of the discrete signal $S^j f_d$.

$$\hat{S}^j f_d(\omega) = \sum_{n \in \mathbb{Z}} S^j f(n 2^{-j_0-j+1}) e^{-i 2^{-j_0-j+1} n \omega}.$$

Since $S^j f(n 2^{-j_0-j+1}) = f * \theta^j(n 2^{-j_0-j+1})$, we can similarly show that $\hat{S}^j f_d(\omega 2^{-j_0-j+1})$ can be written

$$\hat{S}^j f_d(\omega) = 2^{j_0+j-1} \sum_{n \in \mathbb{Z}} \hat{f}(\omega + n\pi 2^{j_0+j}) \hat{\theta}(2^{-j}\omega + n\pi 2^{j_0}). \quad (3.130)$$

By comparing equation (3.129) with equation (3.130) we can now derive that

$$\hat{W}^j f_d(\omega) = G(2^{-j-1}\omega) \hat{S}^{j+1} f_d(\omega). \quad (3.131)$$

This equation is the Fourier transform of the discrete convolution given in the assertion (3.79) of lemma 3.2 which concludes the proof of equation (3.79).

Proof of equation (3.80) : We saw in equation (3.130) that the Fourier series $\hat{S}^j f_d(\omega 2^{-j_0-j+1})$ can be written

$$\hat{S}^j f_d(\omega) = 2^{j_0+j-1} \sum_{n \in \mathbb{Z}} \hat{f}(\omega + n\pi 2^{j_0+j}) \hat{\theta}(2^{-j}\omega + n\pi 2^{j_0}) .$$

We can derive from equation (3.4) that

$$\hat{\theta}(2^{-j}\omega + n\pi 2^{j_0}) = U(2^{-j-1}\omega + n\pi 2^{j_0-1}) \hat{\theta}(2^{-j-1}\omega + n\pi 2^{j_0-1}) \text{ so}$$

$$\hat{S}^j f_d(\omega) = 2^{j_0+j-1} \sum_{n \in \mathbb{Z}} \hat{f}(\omega + n\pi 2^{j_0+j}) U(2^{-j-1}\omega + n\pi 2^{j_0-1}) \hat{\theta}(2^{-j-1}\omega + n\pi 2^{j_0-1}) .$$

This summation can be divided in two for n even and n odd :

$$\begin{aligned} \hat{S}^j f_d(\omega) &= 2^{j_0+j-1} \sum_{\substack{n \in \mathbb{Z} \\ n \text{ even}}} \hat{f}(\omega + n\pi 2^{j_0+j+1}) U(2^{-j-1}\omega + n\pi 2^{j_0}) \hat{\theta}(2^{-j-1}\omega + n\pi 2^{j_0}) + \\ &2^{j_0+j-1} \sum_{\substack{n \in \mathbb{Z} \\ n \text{ odd}}} \hat{f}(\omega + n\pi 2^{j_0+j+1} + \pi 2^{j_0+j}) U(2^{-j-1}\omega + n\pi 2^{j_0} + \pi 2^{j_0-1}) \hat{\theta}(2^{-j-1}\omega + n\pi 2^{j_0} + \pi 2^{j_0-1}) . \end{aligned}$$

Since U is a $2^{j_0}\pi$ periodic function, this expression can be written

$$\begin{aligned} \hat{S}^j f_d(\omega) &= U(2^{-j-1}\omega) 2^{j_0+j-1} \sum_{n \in \mathbb{Z}} \hat{f}(\omega + n\pi 2^{j_0+j+1}) \hat{\theta}(2^{-j-1}\omega + n\pi 2^{j_0}) + \\ &U(2^{-j-1}\omega + \pi 2^{j_0-1}) 2^{j_0+j-1} \sum_{n \in \mathbb{Z}} \hat{f}(\omega + n\pi 2^{j_0+j+1} + \pi 2^{j_0+j}) \hat{\theta}(2^{-j-1}\omega + n\pi 2^{j_0} + \pi 2^{j_0-1}) . \end{aligned}$$

By comparing this equation with the expression of $\hat{S}^j f_d(\omega)$ given in equation (3.130), we can derive that

$$\hat{S}^j f_d(\omega) = U(2^{-j-1}\omega) \hat{S}^{j+1} f_d(\omega) + U(2^{-j-1}\omega + \pi 2^{j_0-1}) \hat{S}^{j+1} f_d(\omega + \pi 2^{j_0+j}) .$$

This expression is the Fourier transform of equation (3.80). It shows that $S^j f_d$ can be computed by convolving $S^{j+1} f_d$ with the discrete filter U and taking one sample out of two of the resulting discrete signal.

Appendix F

This appendix gives a proof of lemma 3.3.

Proof of equation (3.83) : We saw in equation (3.131) of appendix E that

$$\hat{W}^j f_d(\omega) = G(2^{-j-1}\omega) \hat{S}^{j+1} f_d(\omega) .$$

Let $\hat{\Lambda}(\omega)$ be the Fourier series of the discrete signal Λ defined in equation (3.83) :

$$\hat{\Lambda}(\omega) = \sum_{n \in \mathbf{Z}} S^j f(n 2^{-j-1}) e^{-in 2^{-j-1}\omega} .$$

With a proof similar to the proof of equation (3.131) given in appendix E, we can show that

$$\hat{\Lambda}(\omega) = U(2^{-j-1}\omega) \hat{S}^{j+1} f_d(\omega) .$$

Let $\bar{U}(2^{-j-1}\omega)$ and $\bar{G}(2^{-j-1}\omega)$ be, respectively, the complex conjugates of $U(2^{-j-1}\omega)$ and $G(2^{-j-1}\omega)$.

$$\bar{U}(2^{-j-1}\omega) \hat{\Lambda}(\omega) + \bar{G}(2^{-j-1}\omega) \hat{W}^j f_d(\omega) = (|U(2^{-j-1}\omega)|^2 + |G(2^{-j-1}\omega)|^2) \hat{S}^{j+1} f_d(\omega) .$$

Since $G(\omega)$ and $U(\omega)$ satisfy $|U(\omega)|^2 + |G(\omega)|^2 = 1$,

$$\bar{U}(2^{-j-1}\omega) \hat{\Lambda}(\omega) + \bar{G}(2^{-j-1}\omega) \hat{W}^j f_d(\omega) = \hat{S}^{j+1} f_d(\omega) .$$

This equation is the Fourier transform of equation (3.83), which concludes the proof of lemma 3.3.

References

1. Adelson, E. and Simoncelli, E., "Orthogonal pyramid transform for image coding," *Proc. SPIE, Visual Commun. and Image Proc.*, 1987.
2. Battle, G., *A block spin construction of ondelettes, Part 1 : Lemarie functions.* to be published
3. Beck, J., Sutter, A., and Ivry, R., "Spatial frequency channels and perceptual grouping in texture segregation," *CVGIP*, vol. 37, 1987.
4. Burt, P.J., "The pyramid as a structure for efficient computation," in *Multiresolution image processing and analysis*, ed. A. Rosenfeld, W.H.Freeman and Company, 1982.
5. Burt, P. J. and Adelson, E. H., "The Laplacian pyramid as a compact image code," *IEEE Trans. on Communications*, vol 31, pp 532-540, April 1983.
6. Crowley, J., "A representation for visual information," *Tech. Rep. CMU-RI-TR-82-7*, Robotic Inst. Carnegie-Mellon Univ., 1987.
7. Daubechie, I., "Orthonormal bases of compactly supported wavelets," *subm. to IEEE Trans. on Information Theory*, Bell lab., 1987.
8. Daubechie, I., "The wavelet transform, time-frequency localization and signal analysis," *To appear in Communications in pure and applied mathematics*, 1988.
9. DeVore, R., "The approximation of continuous functions by positive linear operators," *Lecture Notes in Math.* , vol. 293, Springer-Verlag.
10. Esteban, D. and Galand, C., "Applications of quadrature mirror filters to split band voice coding schemes," *Proc. ICASSP*, May 1977.
11. Federbush, P., "Quantum field theory in ninety minutes," *Bull. Am. Math. Soc.*, 1987.
12. Flandrin, P., "On the spectrum of fractional Brownian motions," *Tech. Rep. ICPI TS-8708*, UA 346, CNRS, Lyon, France.
13. Gagalowicz,, "Vers un modele de textures," These de docteur d'etat, INRIA, May 1983.
14. Graham, N., "Psychophysics of spatial frequency channels," *Perceptual organization*, Hilldale,N.J., 1981.

15. Grimson, W., "Computational experiments with a feature based stereo algorithm," *IEEE Trans. Pattern Analys. Machine Intell.*, vol. 7, pp. 17-34, Jan. 1985.
16. Grossmann, A. and Morlet, J., "Decomposition of Hardy functions into square integrable wavelets of constant shape," *SIAM J. Math.*, vol. 15, pp. 723-736, 1984.
17. Hall, E., Rouge, J., and Wong, R., "Hierarchical search for image matching," *Proc. Conf. on Decision and Control*, pp. 791-796, 1976.
18. Heeger, D. and Pentland, A., "Measurement of fractal dimension using Gabor filters," Tech. Rep. TR 391, SRI AI center.
19. Hummel, R., "Representations based on zero-crossings in scale-space," Tech. Rep. 225, Courant Inst., Dept. Computer Sc., June, 1986.
20. Hummel, R. and Moniot, R., "A network approach to reconstruction from zero-crossings," *Proc. of IEEE Workshop on computer vision*, Dec. 1987.
21. Jaffard, S. and Meyer, Y., "Bases d'ondelettes dans des ouverts de R^n ," *Journ. de Mathematiques pures et appliquees*, 1987.
22. Julesz, B., "Textons, the elements of texture perception and their interactions," *Nature*, vol. 290, March 1981.
23. Koenderink, J., "The structure of images," *Biological Cybernetics*, Springer Verlag, 1984.
24. Kronland-Martinet, R., Morlet, J., and Grossmann, A., "Analysis of sound patterns through wavelet transform," *International Journal on Pattern Analysis and Artificial Intelligence*, Jan. 1987.
25. Lemarie, P.G., "Ondelettes a localisation exponentielles," *Journ. de Math. Pures et Appl.*.. to be published
26. Lemarie, P. G. and Y., Meyer, "Ondelettes et bases Hilbertiennes," *Revista Matematica Ibero Americana*, vol. 2, 1986.
27. Logan, B., "Information in the zero-crossings of band pass signals," *Bell Systems Tech. Journ.* , vol. 56, p. 510, 1977.
28. Maitre, H. and Faust, B., "The nonstationary modelization of images: statistical properties to be verified," *Conf. on Pattern Recognition*, May 1978.

29. Mallat, S., "Multiresolution approximation and wavelets," *Subm. to Transactions of the American Mathematical Society.*, U. of Penn, Aug. 1987.
30. Mallat, S., "A theory for multiresolution signal decomposition : the wavelet representation," *to appear in IEEE Trans. on Pattern Analysis and Machine Intelligence.*, U. of Penn., 1989.
31. Mallat, S., "Dyadic wavelets energy zero-crossings," *invited paper in IEEE Trans. on Information Theory*, U. of Penn., 1989.
32. Mandelbrot, B., in *The fractal geometry of nature*, W.H. Freeman and co., New-York, 1983.
33. Marr, D., in *Vision*, W.H.Freeman and Company, 1982.
34. Marr, D. and Poggio, T., "A theory of human stereo vision," *Proc. Royal Soc. London*, vol. B 204, pp. 301-328, 1979.
35. Max, J., "Quantizing for minimum distortion," *Trans. IRE Informat. Theo.*, vol. 6, pp. 7-14.
36. Meyer, Y., "Ondelettes et fonctions splines," *Seminaire Equations aux Derivees Partielles*, Ecole Polytechnique, Paris, France, Dec. 1986.
37. Meyer, Y., "Principe d'incertitude, bases hilbertiennes et algebres d'operateurs," *Bourbaki seminar*, 1985-86, no 662.
38. Miiilar, and Paui, C., "Recursive quadrature mirror filters; criteria specification and design method," *IEEE trans. on ASSP*, vol. 33, pp. 413-420, Apr. 85.
39. Papoulis, A., in *Probability, random variables, and stochastic processes*, Mc Graw-Hill Book, 1984.
40. Pentland, A., "Fractal based description of natural scenes," *IEEE trans on PAMI*, 6(6); 661-674, 1986.
41. Pirani, G. and V., Zingarelli, "Analytical formula for design of quadrature mirror filters," *IEEE trans. on ASSP*, vol. 32, pp. 645-648, Jun. 84.
42. Rosenfeld, A. and Thurston, M., "Edge and curve detection for visual scene analysis," *IEEE trans Comput*, 1971 vol C-20.

43. Rosenfeld, A. and Vanderburg, G. J., "Coarse-fine template matching," *IEEE Trans. Systems, Man, Cybernetics*, voi. SMC-7, pp. 104-107, 1977.
44. Sanz, J. and Huang, T., "Theorem and experiments on image reconstruction from zero-crossings," *Research report RJ5460* , IBM.
45. Tchamitchian, P., "Biorthogonalite et theory des operateurs," *Revista Matematica Ibero Americana*, vol. 2, 1986.
46. Turner, M., "Texture discrimination by Gabor functions," *Biological Cybernetics*, vol. 55, pp. 71-82, 1986.
47. Tyler, C.W., "Stereoscopic vision: cortical limitations and a disparity scaling effect," *Science*, vol. 181, pp. 276-278, 1978.
48. Watson, A., "Efficiency of a model human image code," *Journ. Opt. Soc. of Amer.*, vol. 4, pp. 2401-2417, Dec. 1987.
49. Witkin, A., "Scale space filtering," *Proc. Int. Joint Conf. Artificial Intell.* , 1983.
50. Woods, J. W. and O'Neill, S. D., "Subband coding of images," *IEEE trans. on ASSP*, vol. 34, Oct. 1986.
51. Yuille, A. and Poggio, T., "Scaling theorems for zero crossings," *IEEE trans on PAMI*, vol. 8, Jan 1986.
52. Zeevi, Y. and Rotem, D., "Image reconstruction from zero-crossings," *IEEE ASSP*, vol. 34, pp. 1269-1277, 1986.

Index

Brownian fractal 4, 48
Haar basis 63
Hardy space 52, 64
Sobolev space 52, 65, 66
coarse to fine 2, 113
coding 39
completeness 28, 35, 75, 123, 93
conjugate filters 25
continuity 77, 83, 99
detail signal 1, 20, 32
distance 91, 1277
energy conservation 75, 83, 90, 123, 126
energy local 87, 124
energy zero-crossings 89, 122
epipolar 113
finite dyadic transform 80
frame 3
frequency channel 23, 34
image segmentation 48, 132
infinite dyadic transform 75
interpolation 79, 102
multiresolution approximation 1, 11, 51
noise 4, 39, 113
pattern matching 1, 132
pyramidal algorithm 24, 28, 36, 104, 106
quantization 39
reconstruction algorithm 28, 93, 106
resolution 1, 11
scale 72
scaling function 13, 52
separable 30, 69
smoothing function 72
spline 135
stereo matching 113
texture 46
translation 4, 50, 75, 90, 123, 126
wavelet dyadic 73, 121
wavelet orthogonal 21, 32
wavelet representation 25, 32
zero-crossings 85, 125